DISSERTATION

DEVELOPMENT OF MICROSYSTEMS FOR POINT-OF-USE MICROORGANISM DETECTION

Submitted by

Lei Wang

Graduate Degree Program in Bioengineering

In partial fulfillment of the requirements

For the Degree of Doctor of Philosophy

Colorado State University

Fort Collins, Colorado

Summer 2018

Doctoral Committee:

Advisor: David S. Dandy

Stuart A. Tobet
Chuck S. Henry
Brian J. Geiss
Travis S. Bailey
Anthony J. Marchese

ABSTRACT

DEVELOPMENT OF MICROSYSTEMS FOR POINT-OF-USE MICROORGANISM DETECTION

This dissertation focuses on systematic studies using microfluidic platforms for sensing of microorganisms, including whole microorganism separation, and nucleic acid and antibody detection. These devices have been constructed, validated, and applied to clinically related samples under the guidance of point-of-care criteria. Specifically, an inertial microfluidic device designed for the enrichment of micron and submicron-sized particles and bioparticles with high throughput has been thoroughly investigated (Chapters 2 and 3). To directly detect and identify nucleic acids and anti-pathogen antibodies in an ultra-sensitive manner, capacitive-based affinity biosensors have been extensively studied (Chapters 4 and 5). Continued development of these point-of-need platforms has the potential to greatly increase the capacity of public health agencies in both developed and developing countries in order to readily and rapidly monitor and diagnose emerging infectious diseases of global significance.

The ability to study individual bacteria or subcellular organelles using inertial microfluidics is still nascent. This is due, in no small part, to the significant challenges associated with concentrating and separating specific sizes of micrometer and sub-micrometer bioparticles in a microfluidic format. In Chapter 2, using a rigid polymeric microfluidic network with optimized microchannel geometry dimensions, it is demonstrated that 2 µm, and even sub-micrometer, particles can be continuously and accurately focused to stable equilibrium positions within the channels. Suspensions have been processed at flow rates up to 1400 µL

min^{-1} in an ultrashort 4 mm working channel length. A wide range of suspension concentrations—from 0.01 to 1 v/v%—have been systematically investigated, with yields greater than 97%, demonstrating the potential of this technology for large-scale implementation. Additionally, the ability of this chip to separate micrometer- and sub-micrometer-sized particles and to focus bioparticles (cyanobacteria) has been demonstrated. This study pushes the microfluidic inertial focusing particle range down to sub-micrometer length scales, enabling novel routes for investigation of individual microorganisms and subcellular organelles.

Next in Chapter 3, the inertial microfluidics built in Chapter 2 for micron-sized particles has been applied for concentration of Cyanobacterium *Synechocystis sp. PCC 6803* with a typical size of 2 µm. The materials used in the new device were chosen with an eye toward low-cost, large-scale commercial manufacture. The operating parameters for inertial focusing of the cyanobacteria suspension have been optimized to achieve high-throughput and high-efficiency concentration. The maximum recovery efficiency achieved in a single microchannel device is 98.4 ± 0.2% (mean ± standard deviation). For those conditions, initial results yield a concentration factor of 3.28 for a single pass, which is 98.5% of the maximum possible value for the current design. In addition, the calculated power consumption is less than or equal to that of traditional enrichment methods for a wide range of concentration factors. It is anticipated that this highly parallelizable, robust approach of enrichment will be economically feasible for concentrating microorganisms.

In Chapter 4, a label-free affinity-based capacitive biosensor using interdigitated electrodes has been investigated for ultrasensitive nucleic acid detection. Using an optimized process of DNA probe preparation to minimize the effect of contaminants present in commercial thiolated DNA probe, the electrode surface was functionalized with 24-nucleotide DNA probes based on a complementary West Nile virus sequence (Kunjin strain). The biosensor has the ability to detect complementary DNA fragments with a detection limit down to 20 DNA target molecules (1.5 aM range), making it suitable for a practical point-of-care (POC) platform for low target count clinical applications without the need for amplification. The reproducibility of the biosensor detection was improved with efficient covalent immobilization of purified single-stranded DNA probe oligomers on cleaned gold microelectrodes. In addition to the low detection limit, the biosensor showed a dynamic range of detection from 1 μL^{-1} to 10^5 μL^{-1} target molecules (20 to 2 million targets), making it suitable for sample analysis in a typical clinical application environment. The binding results for capacitive detection were validated using fluorescent probe and target oligomers. Overall, our findings suggest that these ultrasensitive sensor platforms have the potential to be used as a reliable, sensitive, and in-expensive diagnostic tool for detection of pathogen-specific nucleic acid and immune response at the point-of-care.

Detection of viral infection is commonly performed using serological techniques such as the enzyme-linked immuno-sorbent assay (ELISA) to detect virus-specific antibody responses. Such assays may also be used to determine the phase of infection based on antibody isotype prevalence. However, ELISAs demonstrate limited sensitivity and are difficult to perform at the point of care. In Chapter 4, a novel technique for label-free, rapid detection of ultra-low concentrations of virus specific antibodies is presented. A simple and robust capacitive biosensor based on Zika or Chikungunya antigen-coated microwires has been developed. With little discernable nonspecific binding, the sensor can detect as few as 10 antigen-specific antibody molecules in a small volume, and do so within minutes. The system can also be used to rapidly and specifically determine the isotype of the antigen-specific antibodies. Finally, the results of clinical related sample demonstrated that anti-Zika virus antibody can be sensitively and specifically detected in dilute serum of immune mouse and can be accurately isotyped using the sensor.

Lastly in Chapter 6, the most interesting future directions, in my viewpoint, stem out of the works presented in the dissertation were discussed.

ACKNOWLEDGEMENTS

I would like to thank my advisor Dr. David Dandy for his supports, insights, mentorship and guidance throughout my pursuit of a doctoral degree at CSU. I also would like to acknowledge my committee members, Dr. Stuart Tobet, Dr. Chuck Henry, Dr. Brian Geiss and Dr. Travis Bailey, for their time and inputs throughout my Ph.D. years. I would like to express my utmost gratitude to my colleagues who worked with me for years and contributed to my work presented in this dissertation: Jessica Filer, Dr. MilenaVeselinovic and Lang Yang. I would like to thank Sarah Neys Mattern for her patience and consultations during my Ph.D. years in School of Biomeidcal Engineering. Thank you to all current and past members of the Henry lab and EFRI project – especially to Dr. Kenneth Reardon, Dr. Christie Peebles, Dr. John Wydallis, Dr. Yuanyuan Yang, Dr. Robert Channon, Dr. Yi Ern Cheah, Dr. Stevan Albers, Carlos Enrique Quiroz Arita, Chen Shen, Dr. Rachel Feeny, Dr. David Cate, Dr. Jaclyn Adkins, Dr. Allison Werner, Jacob Sebesta, Yusra Obeidat and Maxwell Fox for your supports and comradery.

Lastly, I am grateful for my family and friends, both near and far, for their support and encouragement. Especially to my parents, uncle, Davita Freeman and Kathy Freeman. I would like to thank my supportive husband, Wenlong Xu. Working with you in the graduate school to get our doctoral degrees together will be the best years in my life. Finally, I would like to thank my newborn son, Ethan, who makes my life more complete and more meaningful.

TABLE OF CONTENTS

CHAPTER 1: INTRODUCTION

1.1 Motivation

Microorganisms include viruses, bacteria, fungi, protozoa, helminthes etc., which can be transferred from one host to another through air, body fluids, food, and water [1]. Any microorganism capable of causing disease, and that cause public transmission and economic losses is known as a pathogenic microorganism [2]. Based on a World Health Organization (WHO) report, pathogenic microorganism-induced infectious diseases are the second leading cause of death throughout the world [3]. For example, lower respiratory tract infections, diarrheal diseases, tuberculosis and HIV/AIDS resulted in 7.1 million deaths worldwide in 2015 [3]. In particular, the unprecedented growth in international travel and trade is making the spread of infectious disease more evident as pandemic risks and outbreaks in the era of globalization [4]. Thus, effective and rapid microbial detection is an essential prerequisite for diagnosis of microorganisms and treatment of disease. In the developed world, the standard and conventional detection methods are typically conducted in high-resource setting laboratories by trained technicians, and are often laborious, time-consuming and costly. Despite the significant advances in improved diagnostic technologies in developed countries, safety issues related to food industries, pathogen outbreaks and sexually transmitted diseases remain to be addressed. For instance, food-borne pathogens were the cause of more than 50 million illnesses reported in the USA alone in 2011 [5]. The situation is even more severe in developing countries, where centralized laboratories for diagnostics and treatments are usually lacking. Indeed, half of the mortality in these countries is due to infectious diseases [6]. Bringing diagnostics to the point of need could potentially allow preliminary self-screening, sorting and employment to supplement the basic medical equipment available in third-world nations [4]. In summary, the timely, effective and low-cost detection of microorganisms, especially point-of-care sensing of pathogenic microbes, remains a pressing issue in a wide array of fields ranging from infectious disease diagnostics [7], food safety [8], drug discovery [9] and clinical research [10].

1.2 Conventional and Standard Methods of Microorganism Detection

The established and standard methods of microorganism detection include microscopy, the culture and colony counting method, polymerase chain reaction (PCR) amplification, and immunoassay [11]. These methods depend on the identification of unique microbiological and biochemical components, and are often combined to yield a more robust result.

Microscopy is a widely used and versatile technique to visualize pathogens which cannot be seen with naked eyes [12], but it is limited in terms of its sensitivity and relatively subjective interpretation of results.

The culturing technique is the oldest microbiological method of detection and remains a standard diagnosis for bacterial identification. This process consists of selective plating, pre-enrichment, selective enrichment, and identification [13], which usually takes 2-3 days for initial results and up to 7-10 days for confirmation [14]. Its main drawbacks are extremely long diagnostic time, labor intensive procedures, high risk of contamination and the requirement of skilled personal to interpret the results [14].

Polymerase chain reaction (PCR) is a nucleic acid amplification technology, which is able to amplify a specific segment of a nucleic acid by cycling through three temperature steps and create millions of copies within hours [15]. Firstly, the target double-stranded DNA is denatured at high temperature into two single-stranded DNAs. Then, the specific primers will anneal to the DNA strands, which is followed by the polymerization process in the presence of deoxyribonucleotides and a thermostable DNA polymerase. The presence of PCR amplification products are visualized on an electrophoresis gel [14]. PCR is the most widely adopted method of detection because it detects the nucleic acid by amplifying the DNA/RNA molecules rather than by amplifying the signal of the products, thus it is less prone to produce false-positive results [14]. Although PCR offers the advantages of specificity, sensitivity and the capacity to detect relatively small numbers of target nucleic acid in samples, it still requires DNA extraction from microbial cells, trained personal to operate and interpret the results, and relative long assay time on the order of hours [16], which limits its point-of-care applications.

The antigen-antibody binding based immunoassay is one of the mainstays of pathogen detection, which however requires purified antibody and has the risk of false positive results due to cross-reactivity [17]. The types of antibodies used for immunodetection include monoclonal, polyclonal and recombinant antibodies [14]. Monoclonal antibodies are able to increase the detection specificity compared to their polyclonal counterparts, while polyclonal antibodies can be produced more quickly and more cost effectively. Recombinant antibodies bridge this gap since they can be raised with high specificity in short time from bacteria [14]. Examples of immunoassays include the enzyme immunoassay (EIA), Enzyme-linked immunosorbent assay (ELISA), Enzyme-linked fluorescent assay (ELFA), immunomagnetic separation and western blot [14].

Overall, the established standard methods for microorganism detection are often labor-intensive, time-consuming and require centralized facilities and experienced personnel [18]. Ideal pathogen detection methods for point-of-care applications should not only have sensitivity and specificity comparable to established standard methods but also be cost-effective, fast and easy to operate and interpret [19]. In addition, the platform should also be stable and robust under a wide range of environmental conditions, low-cost and portable, preferably handheld and disposable [15]. The ability to perform multiplex tests is another important prerequisite, especially for pathogens causing infections with similar symptoms [15].

1.3 Microfluidic Units and biosensors for Microbial Detection

Technologies such as microfluidics and biosensors are promising approaches to meet the aforementioned requirements as point-of-care diagnostic platforms [4]. Microfluidics is the science of manipulating and controlling fluids and particles at micron and submicron scales and the technology associated with the development of methods and devices to undertake such tasks [4]. Microfluidics is able to significantly reduce the sample volume needed, and is good at processing small volumes of complex fluids in a timely and effectively manner without the need for trained technicians and centralized facilities. Microfluidics facilitates the development of disposable chips that can be easily integrated with other devices. In addition, the standard fabrication technology of lithography is fast and straightforward. Other fabrication techniques such as hot embossing and injection molding of thermoplastics (e.g., polymethylmethacrylate, polystyrene and polycarbonate) have been also used [4]. Microfluidic systems fabricated on paper offer a cheap and biodegradable alternative for simple point-of-care diagnostic applications [4]. In the past several decades, the field of microfluidics has grown tremendously, sustained by its promises to revolutionize conventional laboratory handling, processing and analytical techniques [4]. This unique set of capabilities is exactly what is needed for point-of-care diagnostic systems [15].

Similar to microfluidics, biosensors also draw a lot of interest for point-of-care detection due to their comparable specificity and sensitivity with established standard methods yet much faster detection times. Biosensors have been defined as analytical devices incorporating biological materials integrated within a physicochemical transducer or transducing microsystem, which could be optical, electrochemical, thermometric, piezoelectric, magnetic or micromechanical [18]. Biosensors usually consist of two main components: a bioreceptor or a biorecognition element to recognize the target analyte, and a transducer to convert a recognition event into a measurable electrical or optical signal [14].

In general, the microsystems used to detect microorganisms can be further divided into three broad categories, namely through conducting whole-cell microorganisms separations, the sensing of genetic materials/nucleic acids, e.g., DNA or RNA, and detection of metabolite products via protein-based assays, e.g., viral structural protein [4]. These three broad categories will be briefly reviewed in the following sections.

1.3.1 Whole Cell Based Microbial Separation or Concentration

In real-world clinical samples, the concentration of whole microorganism cells is often very low and their sizes quite small—from several microns to tens of nanometers—which makes pathogen detection extremely challenging [20]. For example, even when patients have developed clear clinical symptoms of sepsis, there may be only 1 to 30 colony forming units/mL, and most bacteria range from 0.2 – 2.0 µm in diameter [21]. In addition, there are invariably a large number of interfering or confounding species present in the samples, such as the billions of blood cells mixed with these bacteria. Therefore, isolating or concentrating target microorganisms prior to detection is one critical step in order to realize an effective diagnostic. Many microfluidic devices have been developed to enrich microorganisms from air [22], water [23], and clinical samples [24]. The methods for microbial enrichment can be generally classified as physical or biochemical. With higher potential for point-of-care applications, the physical approaches are the focus of this dissertation. Several promising physical methods are introduced as follows.

There are three strategies usually exploited in the physical separation methods, namely properties of pathogen, the special designs of microchannels and external fields [1], which can be further classified broadly into passive and active techniques. Passive techniques take advantage of the microchannel structures, the flow field and the interactions between the pathogen particles [25]. Example techniques includes filtration, pinched flow fractionation, deterministic lateral displacement and inertial focusing microfluidics.

Filtration is a straightforward separation method that utilizes membrane [26], weir [27], pillar [28] and cross flow [29] to sort particles/bioparticles based on their sizes when flow passes through. Filtration-based microfluidics are widely used to separate biological samples, such as blood samples [30] and urine samples [26]. However, the major problem of these methods is the clogging of particles on the filter faces or between pillars and weirs. Cross-flow filtration is similar in terms of operation but different in the flow direction, which is perpendicular to the micropost array and is able to alleviate the particle accumulation in some extent. But the separation efficiency of the cross-flow filtration is usually limited, because the particles/cells are mostly distributed across the microchannels and only the part of particles that reaches the filtering region can be sorted [29].

Pinched flow fractionation (PFF) is another technique among the passive sorting methods, which is able to separate particles based on their sizes using the intrinsic property of laminar flow in a continuous manner [31]. In pinched flow fractionation, two microchannels are aligned to a wider channel with a pinched segment. One of the microchannels is continuously introduced with particle suspension while the other microchannel has particle-free flow at higher flow rates. The wall of the pinch segment induces forces toward the center of the channel in proportion to the particle sizes. These forces shift the flow profile and lead to separations of the particles perpendicular to the flow direction based on their sizes [32]. Therefore, smaller particles are close to the wall of the broadened segment while large particles are near the centerline of this segment. Then the separated particles can be collected independently by a set of collecting branches [32]. In the symmetrical design of outlet branches, particles with diameters less than the width of the pinched section cannot be separated [33]. The asymmetrically arranged multiple branches enable the separations of particles one order of magnitude smaller compared to the symmetrical design. This asymmetrical design was shown to be able to separate a mixture of particles with different diameters ranging from 1.0 to 5.0 μm [34]. But, 1 μm appears to be the smallest particle size that can be sorted by pinched flow fractionation as reported in published studies, which is around the size of bacteria but still much bigger than any viruses. Therefore, PFF can be applied to accurately separate one bacterium from other bacteria based on their differences in sizes, which is difficult to achieve using other methods such as filtration mentioned above.

Compared to pinched flow fractionation, the deterministic lateral displacement (DLD) method provides a much better separation resolution, which can be as small as 800 nm [35]. The DLD utilizes posts in specific arrangements in microchannels to guide the pathways of the particles. Each sequential row of posts shifts laterally at a specified angle, which results in known paths of flow. Then a particle moves to the streamline that aligns with its diameter, and particles with different sizes can be separated from each other along the array of posts [36]. This technology has been used to separate millimeter [37], micrometer [38] and even sub-micrometer [39] sized particles, and has been applied for whole blood components [38], blood plasma with no dilution [38], and bacterial artificial chromosome separation [39]. As reported, the smallest size of microspheres separated is 0.8 μm [39]. The size-based separation of bacteria can therefore be realized using this technique. With advances in nanofabrication, the gap size between posts could be further reduced and these improved devices could, in principle, be used to fractionate even smaller biological samples, such as virus particles. However, the very low throughput (0.01 µL/min [40]), requirements for high precision fabrication, and pillar clogging are the major limitations of this approach for broader applications.

As one of the passive sorting methods, inertial focusing microfluidics is not only able to separate particles/bioparticles based on their size differences, but also to focus the particles into single or multiple particle trains during the same process, which makes inertial focusing highly promising for novel applications such as miniaturized flow cytometry and digital microfluidics-based single-cell analysis. The inertial focusing phenomenon arises from lateral forces exerted on particles in a dilute suspension as they are transported in a non-uniform velocity profile under finite Reynolds number, laminar conditions. The equilibrium migration location of particles depends on a number of factors, including the ratio of the particle size to the channel dimensions, and the Reynolds number Re, which is a dimensionless parameter describing the ratio of inertial forces to viscous forces [41]. In laminar channel or tube flow, each particle experiences a force associated with the parabolic velocity profile. This force, the shear gradient lift force (F_{SL}), pushes particles away from channel centerline. At the same time, channel wall induces a wall-effect lift force (F_{WL}), which moves the particles away from the channel or tube wall [42]. The net lift force (F_L) in a rectangular channel can be expressed as [43]

$$F_L = \frac{\rho U_m^2 a^4}{D_h^2} f_c \tag{1}$$

where ρ is the fluid density, U_m is the maximum channel velocity, a is the particle diameter, f_c is the lift coefficient, and $D_h = 2hw/(h+w)$ is the hydraulic diameter, where h

and w are the height and width of the channel cross-section, respectively. Application of inertial focusing devices mainly focus on precise manipulation of erythrocyte-sized cell suspensions for a number of applications in clinical diagnostics [43]–[46]. Inertial focusing based microfluidics possesses very high throughput (1500 µL/min [47]), very high separation efficiency and simple fabrication techniques. However, separation of smaller micron-sized particles/bioparticles using inertial microfluidics presents a number of technical challenges [41], [48]. As shown in Equation 1, the net lift force will decrease significantly with relatively small changes in particle size due to the fourth-order dependence. Therefore, additional developmental efforts are still needed for small micro and sub-micro particle separation using inertial focusing.

As opposed to passive approaches, active methods apply various external fields on the particles/bioparticles; these include dielectrophoretic, magnetic, optical and acoustic fields [25]. In the following section, we briefly introduce electrophoresis, which applies a dielectrophoretic field on particles, as a typical example of the active methods.

Electrophoresis is widely used as an active approach for particle discrimination and fractionation. When a particle is placed in a nonuniform electrical field, it becomes polarized and experiences a lateral force [49]. Electrophoresis enables electrically-controllable trapping, focusing, translation, fractionation and characterization of particulate mineral, chemical, and biological analytes within a fluid suspending medium [49]. Electrophoresis based separation is on the basis of their dielectric properties. It is feasible to separate mixtures of very small particles, such as mixed nanoparticle solutions into subpopulations. For example, a solution of 93 nm diameter latex beads with a distribution of surface charge can be separated by dielectrophoresis [50]. Because the dielectric properties of a particle depend on both its structure and composition, dielectrophoretic forces access a much richer set of particle properties [49].

However, the application of this approach is limited to separation of particles with significantly different electrophoretic responses [25]. High voltage required for device operation and very low throughput (0.009 μL/min [40]) are additional disadvantages.

In general, the passive sorting methods are better than active approaches due to the absence of need for applied external forces, while the active techniques usually have better separation efficiency. Thus, passive sorting methods can be used where energy input is of critical concern, while active separation techniques are preferred where better concentration efficiency is desired.

1.3.2 Antibody/antigen and alternatives Based Microbial Detection

Antibody-based microfluidic detection is one of the main analytical techniques for microorganism detection. This powerful analytical tool employs immunological principles that rely on the intrinsic affinities between antigen and antibody to obtain the specific affinity. The majority of the systems for microorganism detection immobilize the antibody on a platform surface to detect the presence of antigens in samples [51], [52]. Antibody based microorganism detection in microfluidic systems has been demonstrated using different biosensing tools, including colorimetric detection [53], fluorescence [54], chemiluminescence [52], surface plasmon resonance [55] and impedance [56]. Following a different strategy, a diagnostic method was recently reported for detecting circulating antibodies using a specific antigen [57], which avoids the device selectivity being limited to the specificity of the antibodies used. Applying the antibody/antigen detection approach, infection by microorganisms such as influenza [58], *E. coli* [59], hepatitis B [52], HIV [60] and Zika virus [57] have been detected.

Although antibody/antigen based detection systems are widely used, they suffer from some disadvantages, for instance, the use of animals for production of antibodies, poor stability and high cost. There are several reported alternatives to antibody/antigen, for example, recombinant antibody-fragments (rAbs) [61], molecularly imprinted polymers [62], aptamers [63] and antimicrobial peptides [54]. We will succinctly cover these alternatives in the following section.

Recombinant antibody-fragments (rABs), such as single chain variable fragments, are antibody fragments generated using recombinant antibody coding genes both as a source and as a display technology [64]. Unlike monoclonal antibodies, rABs do not require hybridomas and animals in the production process and only require synthetic genes [64]. As a result, rABs have comparable specificity to mAbs but much lower cost in production. For more details, interested readers can refer to an excellent review on antibody fragments as probes in biosensors [65].

Molecularly imprinted polymers (MIPs) are highly selective polymeric materials produced by the molecular imprinted polymerization, which leaves cavities in polymer matrix with affinity to a chosen “template” molecule [66]. MIPs can be produced at a low cost with high stability and high reproducibility. A detailed review on MIPs based biosensors can be found elsewhere [67]. As an alternative to antibodies, MIP-based pathogen detection preserves the original states and orientations of proteins to provide a high specificity and sensitivity [19]. For example, Heat shock protein 60 (Hsp60), which is a specific receptor for *Listeria monocytogene*s infection, has been used as capture probe for *L. monocytogenes* in a microfluidic format. By using Hsp60, the binding efficiency and sensitivity were much greater than those observed using a monoclonal antibody [68].

Aptamers are short nucleic acid or peptide molecules produced by *in vitro* processes and are capable of binding specific target molecules with enhanced affinity and specificity [69]. However, attempts to use aptamers in practice have been shown to be less efficient than initial expectations, partly due to the lengthy selection time [66]. A detailed review to address the problems, solutions and prospects of aptamer based diagnostics and therapies is available elsewhere [69].

Antimicrobial peptides (AMPs), also called host defense peptides (HDPs), are part of the innate immune response found among all forms of life [70]. When compared to antibodies, AMPs are advantageous with better stability, long-term functionality, and broad-spectrum detection. Antimicrobial peptides have been demonstrated to kill Gram negative and Gram positive bacteria, enveloped viruses, fungi and even transformed or cancerous cells [70]. If the goal is to detect a broad range of pathogens, AMPs are very useful due to semi-selectivity toward the targets. However, for the detection of a specific pathogen, antibody based detection is better than AMPs.

1.3.3 DNA/RNA Nucleic Acid Based Microbial Detection

The fundamental methods developed for nucleic acid based detection are nucleic acid hybridization, polymerase chain reaction (PCR), and fluorescence based techniques [71], [72]. Among these detection technologies, hybridization based methods have been shown to be superior because they are highly sequence-specific, direct, rapid and economical for detection of infectious diseases.

In the hybridization strategy, a specific sequence of DNA is utilized as the probe to capture complimentary target DNA or RNA. Unlike antibodies, nucleic acid used as the probe of a sensor can be easily and readily synthesized. The accumulated knowledge of peptide nucleic acid (PNA) has opened a new research area of DNA biosensors. PNA is a DNA analogue with a peptide backbone instead of a sugar phosphate backbone [19]. Compared to DNA or RNA, PNAs hold the advantages of better chemical and thermal stability, resistance to enzymatic degradation, faster hybridization kinetics, and the ability to hybridize at lower salt concentrations. One drawback of the PNA probes are their relatively high cost compared to DNA probes.

In the hybridization approach, the biological event of DNA/RNA hybridization is converted into measurable and recordable signals in direct proportion to the concentration of analytes [73]. Microsystem DNA/RNA-based detection systems have been coupled to different measurement techniques to detect hybridization events, including amperometric (current measurement at constant potential) [74], potentiometric (potential measurement at constant current) [75], impedance (measurement of changes in resistance) [76], piezoelectric (measurement of changes in mass) [77], thermal (measurement of changes in temperature) [78] or optical (detect changes in transmission of light) [71].

Due to minimal direct detection levels varying between 10^5-10^6 target molecules without any signal amplification technologies, target probing using hybridization-based assays are limited in terms of sensitivity, thus requires additional signal enhancement techniques. Many techniques have been applied to improve the sensitivity, including optical, fluorescent, and electrochemical methods[79]. The first two approaches enhance both the specific and nonspecific signals, thereby leading to increases in potential false positives and deterioration in selectivity. In contrast, the electrochemical method directly detects targets and no further chemical modification is needed on the probes. This method is preferred also because the electrochemical signal can be generated and measured only at events involving specific binding, which circumvents the specificity issue, especially in complex matrices such as blood or serum [80].

1.4 Objectives of this dissertation

The general goal of this dissertation is to develop point-of-care platforms that capture the key elements of gold standard methods for whole microorganism separation, nucleic acid and antibody detection in low-resource settings. To build such platforms, several issues will need to be addressed, which are discussed below.

To achieve the goal of the whole microorganism concentration for point-of-care applications, passive microfluidic separation approaches are better than the active microfluidics because the passive methods do not require additional reagents, external fields or electronics, making them suitable for low-source settings. Among all the microfluidic bioparticle passive sorting techniques introduced above, inertial focusing microfluidics is superior to the other approaches due to its capability for very high throughput, high separation efficiency and simple fabrication requirements. Over the past ten years, there have been a number of studies demonstrating the effectiveness of inertial focusing in a microfluidic format to isolate and concentrate mammalian cell-sized particles and bioparticles, but much less work has been done on micron and submicorn-sized particles. Thus, the first aim of this dissertation (Chapters 2 and 3) is to develop a powerful platform to sort these smaller particles using inertial focusing microfluidics, and validate this platform with a microorganism based on its separation performances and throughput per footprint.

One fundamental limitation to direct and practical point-of-care pathogen detection (nucleic acid or antibody) is posed by the trace quantities of microbes typically present in samples, even though such low concentrations may have the potential to be lethal. Since most of the detection levels of developed DNA or antibody sensors vary between 10^5-10^6 target molecules, direct target capture assays are limited in terms of sensitivity [79]. Therefore, the aim of this part of dissertation (Chapters 4 and 5) is to develop ultrasensitive platforms for trace pathogen nucleic acid and anti-pathogen antibody detection without the need for sample enrichment or signal amplification. The development of such diagnostic platforms in general will greatly benefit public health agencies worldwide to monitor emerging infectious diseases of global importance in future.

1.5 Organization of the Dissertation

In this section, brief outlines of each chapter are given.

Chapter 2. "High-Throughput Inertial Focusing of Micrometer- and Sub-Micrometer-Sized Particles Separation". In this chapter, a serpentine channel inertial focusing microfluidic system has been designed, fabricated and validated. This part of study demonstrated that inertial migration and Dean flow can be effectively and efficiently applied as a powerful tool for inertial focusing of micron-sized particles and bioparticles with high throughput. The unique chips designed for 2 µm and 0.92 µm particles have been constructed using a rigid and easy-to-process polymer. A wide range of flow rates has been tested for this design to achieve as high-throughput as possible. The minimum length of the serpentine channel has been explored to reduce the footprint and it was found to be significantly shorter in length than those in other published studies. For the applications to biological samples, the focusing performance of the chip has been investigated for deformable bioparticles, specifically cyanobacteria.

Chapter 3. "A microfluidic concentrator for cyanobacteria harvesting". As an example of microorganism separation, the inertial focusing microfluidics studied in Chapter 2 has been adapted specially to concentrate Cyanobacterium *Synechocystis* sp. PCC 6803 with a typical size of 2 µm. The operating parameters for inertial focusing of the cyanobacteria suspension have been optimized to achieve high-throughput and high-efficiency concentration. Once focused, the stream of cyanobacteria can be readily separated from the culture medium to obtain a concentrated product. The recovery efficiency and concentration factor are used to evaluate the performance of this inertial focusing platform for micro-algal applications.

Chapter 4. "A sensitive DNA capacitive biosensor using interdigitated electrodes". This chapter presents a label-free affinity-based capacitive biosensor to detect trace viral DNA using interdigitated electrodes. The gold interdigitated electrode surface was functionalized with DNA probes based on the West Nile virus sequence (Kunjin strain). The protocol of DNA probe preparation has been optimized in order to minimize the effect of contaminants in commercial thiolated DNA probes. The DNA binding results presented in this chapter were validated using fluorescent oligomers. The reproducibility of the biosensor detection was improved with modification of single-stranded DNA probe oligomers and gold microelectrodes. The detection limit and the dynamic range of the detection have been examined to verify that it is suitable as a practical point-of-care (POC) platform for ultrasensitive clinical applications without the need for amplification.

Chapter 5. "An Ultra-Sensitive Capacitive Microwire Sensor for Pathogen-Specific Serum Antibody Responses". This chapter is dedicated to the construction and testing of an ultrasensitive biosensor for label-free, rapid detection of ultra-low concentrations of virus-specific antibodies. A simple and robust capacitive biosensor based on Zika or Chikungunya antigen-coated microwires has been developed, optimized and validated with monoclonal antibodies and polyclonal antibodies in mouse serum. The specificity and detection limit have been evaluated. In addition, the anti-ZIKV antibodies during an immunization time-course response and the isotypes of antigen-specific antibodies have been investigated.

REFERENCES

[1] D. Zhang, H. Bi, B. Liu, and L. Qiao, "Detection of Pathogenic Microorganisms by Microfluidics Based Analytical Methods," *Anal. Chem.*, p. acs.analchem.8b00399, 2018.

[2] H. D. Isenberg and B. G. Painter, "Indigenous and pathogenic microorganisms of humans.," *Indig. Pathog. Microorg. humans.*, pp. 25–39, 1980.

[3] "The top 10 causes of death." [Online]. Available: http://www.who.int/en/news-room/fact-sheets/detail/the-top-10-causes-of-death. [Accessed: 04-Jun-2018].

[4] L. Y. Yeo, H. C. Chang, P. P. Y. Chan, and J. R. Friend, "Microfluidic devices for bioapplications," *Small*, vol. 7, no. 1, pp. 12–48, 2011.

[5] C. A. Batt, "Food pathogen detection," *Science (80-.).*, vol. 316, no. 5831, pp. 1579–1580, 2007.

[6] D. M. Morens, G. K. Folkers, and A. S. Fauci, "The challenge of emerging and re-emerging infectious diseases," vol. 430, no. July, 2004.

[7] T. R. Kozel and A. R. Burnham-Marusich, "Point-of-Care Testing for Infectious Diseases: Past, Present, and Future.," *J. Clin. Microbiol.*, vol. 55, no. 8, pp. 2313–2320, Aug. 2017.

[8] M. Y.-C. Wu, M.-Y. Hsu, S.-J. Chen, D.-K. Hwang, T.-H. Yen, and C.-M. Cheng, "Point-of-Care Detection Devices for Food Safety Monitoring: Proactive Disease Prevention.," *Trends Biotechnol.*, vol. 35, no. 4, pp. 288–300, Apr. 2017.

[9] M. Drancourt, A. Michel-Lepage, S. Boyer, and D. Raoult, "The Point-of-Care Laboratory in Clinical Microbiology.," *Clin. Microbiol. Rev.*, vol. 29, no. 3, pp. 429–47, Jul. 2016.

[10] K. R. King, L. P. Grazette, D. N. Paltoo, J. T. McDevitt, S. K. Sia, P. M. Barrett, F. S. Apple, P. A. Gurbel, R. Weissleder, H. Leeds, E. J. Iturriaga, A. K. Rao, B. Adhikari, P. Desvigne-Nickens, Z. S. Galis, and P. Libby, "Point-of-Care Technologies for Precision Cardiovascular Care and Clinical Research: National Heart, Lung, and Blood Institute Working Group," *JACC Basic to Transl. Sci.*, vol. 1, no. 1–2, pp. 73–86, Jan. 2016.

[11] R. Singh, M. Das Mukherjee, G. Sumana, R. K. Gupta, S. Sood, and B. D. Malhotra, "Biosensors for pathogen detection: A smart approach towards clinical diagnosis," *Sensors Actuators, B Chem.*, vol. 197, pp. 385–404, 2014.

[12] "What is Microscopy? | The University of Edinburgh." [Online]. Available: https://www.ed.ac.uk/clinical-sciences/edinburgh-imaging/for-patients-study-participants/tell-me-more-about-my-scan/what-is-microscopy. [Accessed: 04-Jun-2018].

[13] D. J. Fagerberg and J. A. Vens, “Enrichment and Plating Methodology for Salmonella Detection in Food. A Review 1,” *J. Milk Food Techno*, vol. 39, no. 628, 1976.

[14] V. Velusamy, K. Arshak, O. Korostynska, K. Oliwa, and C. Adley, “An overview of foodborne pathogen detection: In the perspective of biosensors,” *Biotechnol. Adv.*, vol. 28, no. 2, pp. 232–254, 2010.

[15] P. Yager, T. Edwards, E. Fu, K. Helton, K. Nelson, M. R. Tam, and B. H. Weigl, “Microfluidic diagnostic technologies for global public health,” *Nature*, vol. 442, no. 7101, pp. 412–418, 2006.

[16] M. A. Syed, “Advances in nanodiagnostic techniques for microbial agents,” *Biosens. Bioelectron.*, vol. 51, pp. 391–400, 2014.

[17] J. Tate and G. Ward, “Interferences in immunoassay.,” *Clin. Biochem. Rev.*, vol. 25, no. 2, pp. 105–20, May 2004.

[18] O. Lazcka, F. J. Del Campo, and F. X. Muñoz, “Pathogen detection: A perspective of traditional methods and biosensors,” *Biosens. Bioelectron.*, vol. 22, no. 7, pp. 1205–1217, 2007.

[19] A. M. Foudeh, T. Fatanat Didar, T. Veres, and M. Tabrizian, “Microfluidic designs and techniques using lab-on-a-chip devices for pathogen detection for point-of-care diagnostics,” *Lab Chip*, vol. 12, no. 18, p. 3249, 2012.

[20] S. Sengupta, J. E. Gordon, and H. C. Chang, “Microfluidic diagnostic systems for the rapid detection and quantification of pathogens,” *Microfluid. Biol. Appl.*, pp. 271–322, 2009.

[21] P. Yagupsky and F. S. Nolte, “Quantitative aspects of septicemia,” *Clin. Microbiol. Rev.*, vol. 3, no. 3, pp. 269–279, 1990.

[22] W. Jing, W. Zhao, S. Liu, L. Li, C.-T. Tsai, X. Fan, W. Wu, J. Li, X. Yang, and G. Sui, “Microfluidic Device for Efficient Airborne Bacteria Capture and Enrichment,” *Anal. Chem.*, vol. 85, no. 10, pp. 5255–5262, May 2013.

[23] U. Dharmasiri, M. A. Witek, A. A. Adams, J. K. Osiri, M. L. Hupert, T. S. Bianchi, D. L. Roelke, and S. A. Soper, “Enrichment and Detection of *Escherichia coli* O157:H7 from Water Samples Using an Antibody Modified Microfluidic Chip,” *Anal. Chem.*, vol. 82, no. 7, pp. 2844–2849, Apr. 2010.

[24] A. Urbansky, P. Ohlsson, A. Lenshof, F. Garofalo, S. Scheding, and T. Laurell, “Rapid and effective enrichment of mononuclear cells from blood using acoustophoresis,” *Sci. Rep.*, vol. 7, no. 1, p. 17161, Dec. 2017.

[25] P. Sajeesh and A. K. Sen, “Particle separation and sorting in microfluidic devices: A review,” *Microfluid. Nanofluidics*, vol. 17, no. 1, pp. 1–52, 2014.

[26] F. Li, R. M. Guijt, and M. C. Breadmore, “Nanoporous membranes for microfluidic concentration prior to electrophoretic separation of proteins in urine,” *Anal. Chem.*, vol. 88, no. 16, pp. 8257–8263, 2016.

[27] L. Zhu, Q. Zhang, H. Feng, S. Ang, F. S. Chau, and W.-T. Liu, “Filter-based microfluidic device as a platform for immunofluorescent assay of microbial cells,” *Lab Chip*, vol. 4, no. 4, p. 337, Aug. 2004.

[28] Y. Yoon, S. Kim, J. Lee, J. Choi, R.-K. Kim, S.-J. Lee, O. Sul, and S.-B. Lee, “Clogging-free microfluidics for continuous size-based separation of microparticles,” *Sci. Rep.*, vol. 6, no. 1, p. 26531, Sep. 2016.

[29] Y. Y. Chiu, C. K. Huang, and Y. W. Lu, “Enhancement of microfluidic particle separation using cross-flow filters with hydrodynamic focusing,” *Biomicrofluidics*, vol. 10, no. 1, pp. 1–13, 2016.

[30] A. Homsy, P. D. van der Wal, W. Doll, R. Schaller, S. Korsatko, M. Ratzer, M. Ellmerer, T. R. Pieber, A. Nicol, and N. F. de Rooij, “Development and validation of a low cost blood filtration element separating plasma from undiluted whole blood,” *Biomicrofluidics*, vol. 6, no. 1, pp. 1–9, 2012.

[31] J. Oakey, J. Allely, and D. W. M. Marr, “Laminar-flow-based separations at the microscale,” *Biotechnol. Prog.*, vol. 18, no. 6, pp. 1439–1442, 2002.

[32] M. Yamada, M. Nakashima, and M. Seki, “Pinched flow fractionation: Continuous size separation of particles utilizing a laminar flow profile in a pinched microchannel,” *Anal. Chem.*, vol. 76, no. 18, pp. 5465–5471, 2004.

[33] A. Jain and J. D. Posner, “Particle dispersion and separation resolution of pinched flow fractionation,” *Anal. Chem.*, vol. 80, no. 5, pp. 1641–1648, 2008.

[34] J. Takagi, M. Yamada, M. Yasuda, and M. Seki, “Continuous particle separation in a microchannel having asymmetrically arranged multiple branches,” *Lab Chip*, vol. 5, no. 7, p. 778, 2005.

[35] L. R. Huang, E. C. Cox, R. H. Austin, and J. C. Sturm, “Continuous Particle Separation Through Deterministic Lateral Displacement,” *Science (80-.).*, vol. 304, no. 5673, pp. 987–990, May 2004.

[36] J. McGrath, M. Jimenez, and H. Bridle, “Deterministic lateral displacement for particle separation: a review,” *Lab Chip*, vol. 14, no. 21, pp. 4139–4158, 2014.

[37] M. Balvin, E. Sohn, T. Iracki, G. Drazer, and J. Frechette, “Directional locking and the role of irreversible interactions in deterministic hydrodynamics separations in microfluidic Devices,” *Phys. Rev. Lett.*, vol. 103, no. 7, pp. 2–5, 2009.

[38] J. A. Davis, D. W. Inglis, K. J. Morton, D. A. Lawrence, L. R. Huang, S. Y. Chou, J. C. Sturm, and R. H. Austin, “Deterministic hydrodynamics: Taking blood apart,” *Proc. Natl.*

Acad. Sci., vol. 103, no. 40, pp. 14779–14784, 2006.

[39] L. R. Huang, E. C. Cox, R. H. Austin, and J. C. Sturm, “Continous particle separation through deterministic lateral displacement,” *Science (80-.).*, vol. 304, no. 5673, pp. 987–991, 2004.

[40] T. Salafi, K. K. Zeming, and Y. Zhang, “Advancements in microfluidics for nanoparticle separation,” *Lab Chip*, vol. 17, no. 1, pp. 11–33, 2017.

[41] D. Di Carlo, D. Irimia, R. G. Tompkins, and M. Toner, “Continuous inertial focusing, ordering, and separation of particles in microchannels.,” *Proc. Natl. Acad. Sci. U. S. A.*, vol. 104, no. 48, pp. 18892–7, 2007.

[42] D. Di Carlo, J. F. Edd, D. Irimia, R. G. Tompkins, and M. Toner, “Equilibrium separation and filtration of particles using differential inertial focusing,” *Anal. Chem.*, vol. 80, no. 6, pp. 2204–2211, 2008.

[43] J. Oakey, R. W. A. Jr, E. Arellano, D. Di Carlo, and W. Steven, “Particle Focusing in Staged Inertial Microfluidic Devices for Flow Cytometry,” vol. 82, no. 9, pp. 3862–3867, 2011.

[44] J. Sun, M. Li, C. Liu, Y. Zhang, D. Liu, W. Liu, G. Hu, and X. Jiang, “Double spiral microchannel for label-free tumor cell separation and enrichment,” *Lab Chip*, vol. 12, no. 20, p. 3952, 2012.

[45] M. E. Warkiani, G. Guan, K. B. Luan, W. C. Lee, A. A. S. Bhagat, P. K. Chaudhuri, D. S.-W. Tan, W. T. Lim, S. C. Lee, P. C. Y. Chen, C. T. Lim, and J. Han, “Slanted spiral microfluidics for the ultra-fast, label-free isolation of circulating tumor cells.,” *Lab Chip*, vol. 14, no. 1, pp. 128–37, 2014.

[46] N. M. Karabacak, P. S. Spuhler, F. Fachin, E. J. Lim, V. Pai, E. Ozkumur, J. M. Martel, N. Kojic, K. Smith, P. Chen, J. Yang, H. Hwang, B. Morgan, J. Trautwein, T. a Barber, S. L. Stott, S. Maheswaran, R. Kapur, D. a Haber, and M. Toner, “Microfluidic, marker-free isolation of circulating tumor cells from blood samples.,” *Nat. Protoc.*, vol. 9, no. 3, pp. 694–710, 2014.

[47] L. Wang and D. S. Dandy, “High-Throughput Inertial Focusing of Micrometer- and Sub-Micrometer-Sized Particles Separation,” *Adv. Sci.*, vol. 4, no. 10, 2017.

[48] I. D. Johnston, M. B. McDonnell, C. K. L. Tan, D. K. McCluskey, M. J. Davies, and M. C. Tracey, “Dean flow focusing and separation of small microspheres within a narrow size range,” *Microfluid. Nanofluidics*, vol. 17, no. 3, pp. 509–518, 2014.

[49] A. Manuscript, “Particle separation by dielectrophoresis.pdf,” *Electrophoresis*, vol. 23, no. 13, pp. 1973–1983, 2009.

[50] N. G. Green and H. Morgan, “Dielectrophoretic separation of nano-particles,” *J. Phys. D. Appl. Phys.*, vol. 30, no. 11, pp. 3–7, 1997.

[51] F. Y. H. Lin, M. Sabri, J. Alirezaie, D. Li, and P. M. Sherman, “Development of a nanoparticle-labeled microfluidic immunoassay for detection of pathogenic microorganisms.,” *Clin. Diagn. Lab. Immunol.*, vol. 12, no. 3, pp. 418–25, Mar. 2005.

[52] A. Xiang, F. Wei, X. Lei, Y. Liu, Y. Liu, and Y. Guo, “A simple and rapid capillary chemiluminescence immunoassay for quantitatively detecting human serum HBsAg,” *Eur. J. Clin. Microbiol. Infect. Dis.*, vol. 32, no. 12, pp. 1557–1564, Dec. 2013.

[53] J.-Y. Kim and M.-K. Yeo, “A fabricated microfluidic paper-based analytical device (μPAD) for in situ rapid colorimetric detection of microorganisms in environmental water samples,” *Mol. Cell. Toxicol.*, vol. 12, no. 1, pp. 101–109, Mar. 2016.

[54] O. Schwartz and M. Bercovici, “Microfluidic Assay for Continuous Bacteria Detection Using Antimicrobial Peptides and Isotachophoresis,” *Anal. Chem.*, vol. 86, no. 20, pp. 10106–10113, Oct. 2014.

[55] Y. Wang, W. Knoll, and J. Dostalek, “Bacterial Pathogen Surface Plasmon Resonance Biosensor Advanced by Long Range Surface Plasmons and Magnetic Nanoparticle Assays,” *Anal. Chem.*, vol. 84, no. 19, pp. 8345–8350, Oct. 2012.

[56] P. B. Lillehoj, C. W. Kaplan, J. He, W. Shi, and C.-M. Ho, “Rapid, Electrical Impedance Detection of Bacterial Pathogens Using Immobilized Antimicrobial Peptides,” *J. Lab. Autom.*, vol. 19, no. 1, pp. 42–49, Feb. 2014.

[57] G. Cabral-Miranda, A. R. Cardoso, L. C. S. Ferreira, M. G. F. Sales, and M. F. Bachmann, “Biosensor-based selective detection of Zika virus specific antibodies in infected individuals.,” *Biosens. Bioelectron.*, vol. 113, no. April, pp. 101–107, Aug. 2018.

[58] K. F. Lei, C.-H. Huang, R.-L. Kuo, C.-K. Chang, K.-F. Chen, K.-C. Tsao, and N.-M. Tsang, “Paper-based enzyme-free immunoassay for rapid detection and subtyping of influenza A H1N1 and H3N2 viruses,” *Anal. Chim. Acta*, vol. 883, pp. 37–44, Jul. 2015.

[59] S. Wang, F. Inci, T. L. Chaunzwa, A. Ramanujam, A. Vasudevan, S. Subramanian, A. Chi Fai Ip, B. Sridharan, U. A. Gurkan, and U. Demirci, “Portable microfluidic chip for detection of Escherichia coli in produce and blood.,” *Int. J. Nanomedicine*, vol. 7, pp. 2591–600, 2012.

[60] A. Kah, P. Tay, B. L. Khoo, and M. E. Warkiani, “Microfluidics for Fast and Frugal Diagnosis of Malaria, Sepsis, and HIV/AIDS.”

[61] S. Sharma, H. Byrne, and R. J. O’Kennedy, “Antibodies and antibody-derived analytical biosensors.,” *Essays Biochem.*, vol. 60, no. 1, pp. 9–18, 2016.

[62] G. M. Birnbaumer, P. A. Lieberzeit, L. Richter, R. Schirhagl, M. Milnera, F. L. Dickert, A. Bailey, and P. Ertl, “Detection of viruses with molecularly imprinted polymers integrated on a microfluidic biochip using contact-less dielectric microsensors,” *Lab Chip*, vol. 9, no. 24, p. 3549, Dec. 2009.

[63] C.-H. Weng, C.-J. Huang, and G.-B. Lee, “Screening of aptamers on microfluidic systems for clinical applications.,” *Sensors (Basel).*, vol. 12, no. 7, pp. 9514–29, 2012.

[64] P. J. Hudson, “Recombinant antibody fragments,” *Curr. Opin. Biotechnol.*, vol. 9, no. 4, pp. 395–402, Aug. 1998.

[65] D. Saerens, L. Huang, K. Bonroy, and S. Muyldermans, “Antibody fragments as probe in biosensor development,” *Sensors*, vol. 8, no. 8, pp. 4669–4686, 2008.

[66] G. Vasapollo, R. Del Sole, L. Mergola, M. R. Lazzoi, A. Scardino, S. Scorrano, and G. Mele, “Molecularly imprinted polymers: present and future prospective.,” *Int. J. Mol. Sci.*, vol. 12, no. 9, pp. 5908–45, 2011.

[67] Z.-T. Lin, V. DeMarr, J. Bao, and T. Wu, “Molecularly Imprinted Polymer-Based Biosensors: For the Early, Rapid Detection of Pathogens, Biomarkers, and Toxins in Clinical, Environmental, or Food Samples,” *IEEE Nanotechnol. Mag.*, vol. 12, no. 1, pp. 6–13, Mar. 2018.

[68] O. K. Koo, Y. Liu, S. Shuaib, S. Bhattacharya, M. R. Ladisch, R. Bashir, and A. K. Bhunia, “Targeted Capture of Pathogenic Bacteria Using a Mammalian Cell Receptor Coupled with Dielectrophoresis on a Biochip Targeted Capture of Pathogenic Bacteria Using a Mammalian Cell Receptor Coupled with Dielectrophoresis on a Biochip,” vol. 81, no. 8, pp. 3094–3101, 2009.

[69] A. V. Lakhin, V. Z. Tarantul, and L. V. Gening, “Aptamers: Problems, solutions and prospects,” *Acta Naturae*, vol. 5, no. 19, pp. 34–43, 2013.

[70] K. V. R. Reddy, R. D. Yedery, and C. Aranha, “Antimicrobial peptides: Premises and promises,” *Int. J. Antimicrob. Agents*, vol. 24, no. 6, pp. 536–547, 2004.

[71] D. Ivnitski, I. Abdel-Hamid, P. Atanasov, and E. Wilkins, “Biosensors for detection of pathogenic bacteria,” *Biosens. Bioelectron.*, vol. 14, no. 7, pp. 599–624, 1999.

[72] M. J. Wolcott, “Advances in nucleic acid-based detection methods.,” *Clin. Microbiol. Rev.*, vol. 5, no. 4, pp. 370–86, Oct. 1992.

[73] L. Wang, M. Veselinovic, L. Yang, B. J. Geiss, D. S. Dandy, and T. Chen, “A sensitive DNA capacitive biosensor using interdigitated electrodes,” *Biosens. Bioelectron.*, vol. 87, pp. 646–653, 2017.

[74] K. C. Ho, C. Y. Chen, H. C. Hsu, L. C. Chen, S. C. Shiesh, and X. Z. Lin, “Amperometric detection of morphine at a Prussian blue-modified indium tin oxide electrode,” *Biosens. Bioelectron.*, vol. 20, no. 1, pp. 3–8, 2004.

[75] J. Wang, D. Xu, A. N. Kawde, and R. Polsky, “Metal nanoparticle-based electrochemical stripping potentiometric detection of DNA hybridization,” *Anal. Chem.*, vol. 73, no. 22, pp. 5576–5581, 2001.

[76] Y. Xu, Y. Jiang, H. Cai, P. G. He, and Y. Z. Fang, “Electrochemical impedance detection of DNA hybridization based on the formation of M-DNA on polypyrrole/carbon nanotube modified electrode,” *Anal. Chim. Acta*, vol. 516, no. 1–2, pp. 19–27, 2004.

[77] R. Bunde, “Piezoelectric quartz crystal biosensors,” *Talanta*, vol. 46, no. 6, pp. 1223–1236, 1998.

[78] M. MEHRVAR, C. BIS, J. M. SCHARER, M. M.- YOUNG, and J. H. LUONG, “Fiber-Optic Biosensors. Trends and Advances.,” *Anal. Sci.*, vol. 16, no. 7, pp. 677–692, 2000.

[79] J. Mairhofer, K. Roppert, and P. Ertl, “Microfluidic systems for pathogen sensing: A review,” *Sensors (Switzerland)*, vol. 9, no. 6, pp. 4804–4823, 2009.

[80] H. L. L. Yu, A. Maslova, and I. M. Hsing, “Rational Design of Electrochemical DNA Biosensors for Point-of-Care Applications,” *ChemElectroChem*, vol. 4, no. 4, pp. 795–805, 2017.

CHAPTER 2: HIGH-THROUGHPUT INERTIAL FOCUSING OF MICRON- AND SUBMICRON-SIZED PARTICLES SEPARATION[1]

2.1 Introduction

The ability to continuously and reliably concentrate and separate small diameter bioparticle ($D_p \leq 2$ μm) suspensions, such as bacteria, subcellular organelles and even virus that are flowing through microchannels, offers significant potential for biomedical,[1] environmental,[2,3] food analysis,[4] and biofuel production[5] applications. Typically, bioparticle concentration and separation are accomplished through industrial or laboratory centrifugation, where there is a correlation between the size and density of the particles and the rate that they separates from a heterogeneous mixture.[6] When the particle size is very small and its density is comparable to the mixture medium, as with bacteria, virus and subcellular organelles, a high speed or even ultra-high speed centrifuge operating for a long periods of time is required.[6] For moderate volumes of small bioparticle suspensions, centrifugation will work but may result in mechanical damage to the cells due to high shear forces.[7,8] In typical clinical samples where the bacteria/virus numbers are often low and the sample volume is small, centrifugation may be inadequate at concentrating or separating the suspension constituents.[9,10] On the other hand, in industry applications such as cyanobacteria harvesting for biofuel production, large-scale concentration of a dilute cell suspension entails significant power requirements associated with high speed centrifugation.[11]

---

[1] This chapter is published in the following: Wang L, Dandy D.S., (2017) High-throughput Inertial Focusing of Micron- and Submicron-sized Particles Separation Adv. Sci., 2017 May 30;4(10):1700153.

Consequently, a simple but robust platform able to provide significant improvements over current concentration techniques is needed. Ideally, a concentration/separation device for small diameter particle/bioparticle suspensions would be as simple as possible in its design, not require additional reagents or external electronics, and be inexpensive to fabricate and operate. Also, the device should be readily scalable so that the basic technology could be applied to sample volumes ranging from milliliters to hundreds of liters. And the device needs to be sufficiently small to potentially integrate with other point-of-care platforms.

The use of microfluidics has streamlined many traditional laboratory techniques, due to the advantages of ease to operation, low-cost, and miniaturized size.[12] In the specific application to particle/bioparticle concentration and separation, inertial focusing is a very promising approach that relies solely on channel geometry and intrinsic hydrodynamic forces.[13–18] The application of inertial focusing devices has been used for precise manipulation of erythrocyte-sized cell suspensions for a number of applications in clinical diagnostics.[14,19–21] However, separation of smaller, micron-sized bioparticles is challenging using current inertial microfluidics approaches.[16,21–23]

To address the challenge, a better understanding on the mechanism of inertial focusing is necessary to find potential solutions. The inertial focusing phenomenon arises from lateral forces exerted on particles in a dilute suspension as they are transported in flow with a non-uniform velocity profile under laminar conditions. The equilibrium migration location of particles depends on a number of factors, including the ratio of the particle size to the channel dimensions and the Reynolds number, *Re*,[16,20] which is a dimensionless parameter quantifying the ratio of inertial forces to viscous forces.[14] In laminar channel or tube flow, each particle experiences a force associated with the parabolic velocity profile. This force, the shear gradient lift force (F_{SL}), pushes particles away from channel centerline. At the same time, the channel wall exerts a wall-effect lift force (F_{WL}) that pushes the particles away from the channel or tube wall[16]. The net lift force (F_L) in a rectangular channel can be expressed as[16]

$$F_L = \frac{\rho U_m^2 a^4}{D_h^2} f_c \tag{1}$$

where ρ is the fluid density, U_m is the maximum channel velocity, a is the particle diameter, f_c is the lift coefficient, and $D_h = 2hw/(h+w)$ is the hydraulic diameter, where h and w are the height and width of the channel cross-section, respectively. As shown in equation (1), the net lift force will decrease significantly with relatively small changes in particle size due to the fourth-order dependence. To overcome this effect and obtain a focused particle stream, smaller cross-sections and larger velocities are needed. In this study, a channel with appropriately scaled dimensions for small particle/bioparticles suspensions has been designed and fabricated.

The working flow rates in current inertial focusing microfluidics platforms are usually at modest Reynolds numbers (*Re* ≈ 100),[16,22,24] which limits the ability to focus small particles at high throughput in a single microchannel. However, when higher velocities are required, the low elastic modulus of the widely used material Polydimethylsiloxane (PDMS) makes its use problematic for this microfluidics application, resulting in cross section deformation and a loss of focusing at higher flow rates.[21,23] Other polymers with comparably simple fabrication procedures—but much higher rigidity—are needed. A benefit of using higher flow rates is the potential for reduction in channel length, from several centimeters[16] down to millimeters. The reduced size should also lead to reduced pressure drops and pumping requirements.[16]

To get a better separation outcome, fewer particle equilibrium positions are favorable. In a tube of circular cross section, randomly distributed particles are known to focus to an annulus located six-tenths of the distance from the axis to the tube wall,[13] whereas in a channel of a square cross-section the particles focus to four equilibrium regions centered near each face.[16] The number of focused particle streams can be reduced by introducing curvature to the flow path.[14] The inertia of the fluid moving through a channel bend creates secondary swirling motion, known as Dean flow.[14,15] The resulting hydrodynamic drag enhances the lateral migration of particles across the channel. There are two major classes of curved channels: a spiral geometry[18,25,26] and a serpentine channel geometry with asymmetric[14,15,27] or symmetric configurations.[28,29] In this design, an serpentine channel is used to reduce the number of focused particle streams. An added benefit of this slightly increased geometric complexity is a reduced flow length required to achieve focusing relative to straight channels.[16,30] The linear layout of the asymmetric curved channel has one more advantage—its ability to be parallelized, which allows for increased throughput.

In sum, a simple, robust device for inertial focusing of micron- and submicron-sized particles and bioparticles for concentration and separation at high throughput has been designed, constructed, and validated. There are a broad set of potential applications for this platform, such as pathogen and subcellular organelle isolation, separation of virus from bacteria, microalgae harvesting, and monitoring heterogeneous response of bacteria in drug susceptibility testing.

2.2 Experimental Section

2.2.1 Microfluidic Device Fabrication

For TPE chip fabrication, we first created a SU-8 2008 mold (Microchem, MA, USA) using conventional photolithography.[31] The SU-8 patterned silicon master was treated by vapor deposition with hexamethyldisilazane (HMDS) (Sigma-Aldrich, MO, USA) in a 60°C oven for 4 h prior to replica molding with TPE. TPE was prepared by mixing 20 g resin (TAP

Clear-Lite Casting Resin, CA, USA) with 0.2 g MEPK catalyst (TAP plastics, CA, USA), and then the mix was stirred and degassed to remove air bubbles. A piece of PDMS was cut to form a mold surround, which confined the mix in a specific area on the master. Then the TPE mix was poured onto the mold. A piece of transparency film was used as a top cover over the mix to ensure a flat surface. The TPE is placed in a 65°C oven for 10 minutes, after which the TPE replica is peeled from the master. A biopsy punch (Technical Innovations) was used to create 1.5 mm diameter inlet and outlet ports. The TPE replica and a glass substrate were then placed in a plasma chamber and pumped down to 200 mTorr, and the pieces exposed to plasma (Plasma Etch, Carson City, NV, USA) for 1 min, at pressures between 100 and 200 mTorr, and 30 W applied to the RF coil. After removal from the plasma chamber the TPE piece is brought into contact with the glass. The TPE-glass chip is then left to cure in a 60°C oven for 5 min. To enable pressure-driven flow through the TPE-glass hybrid devices, tubing connectors (Nanoport, WA, USA) are attached to the chip using room temperature cured epoxy.

2.2.2 Experimental Setup and Method

During each experiment, the 2 µm red or 0.92 µm green fluorescent polystyrene microsphere suspensions (Thermo Scientific, MA USA) with specific concentrations (0.01, 0.1, and 1 v/v%) in DI water were pumped into the microfluidic device at varying flow rates using a high pressure injection syringe pump (Harvard Apparatus, MA, USA) to generate a stable and continuous flow. The inlet of the device was connected to a syringe by Tygon tubing. For the cell experiments, known concentrations (0.01 v/v% ~ 2.5×10^6 mL^{-1}; 0.1 v/v% ~ 2.5×10^7 mL^{-1}; and 1 v/v% ~ 2.5×10^8 mL^{-1}) of cyanobacteria culture in the syringe were pumped into the device in the same manner as fluorescent microspheres. The suspending medium for the cyanobacteria in the inertial focusing experiments is a liquid BG-11 medium.

2.2.3 Cyanobacteria Source and Cultivation

Cyanobacterium Synechocystis sp. PCC 6803 was grown in liquid BG-11 medium.[32] The strain was inoculated at an initial concentration of 10^6 mL^{-1} and cultured in 250 mL Erlenmeyer flask with 50 mL culture medium in an INNOVA 44 Incubator Shaker (New Brunswick Scientific, Enfield, CT) at a speed of 225 rpm under 30°C at an average light intensity of 100±9 $\mu mol/m^2 \cdot s$. These 50 mL suspensions were cultured to a final concentration between 2×10^8 and 5×10^8 mL^{-1}. The suspension was then diluted or concentrated to achieve the desired density for the inertial focusing studies.

2.2.4 Fluorescence Imaging

TPE-glass devices were mounted onto the stage of an inverted fluorescent microscope (AMG, Mill Creek, Washington). Fluorescent streak images were obtained using a GFP light cube (excitation/emission: 470/510 nm) with exposure times of 200 ms. Recorded images were processed using ImageJ (http://rsb.info. nih.gov/ij/).

2.2.5 High-speed Imaging

The flow of the cyanoabcteria suspension was recorded at 2000 frames per second (495 μs interval) with a 5 μs shutter speed using a high-speed camera (Fastcam SA3, Photron, USA) connected to an Olympus IX 71 Inverted optical Microscope (Olympus, Japan).

2.2.6 Image Analysis and Measurement

Image analysis was conducted using ImageJ (http://rsb.info.nih.gov/ij/). The concentrations of cyanobacteria were measured by a hemocytometer (hausser Scientific Partnership, Horsham, PA), and the suspension concentrations were then calculated from three different hemocytometry measurements.

2.3 Results and Discussion

2.3.1 Design of the Focusing Device.

The experiments done here have successfully demonstrated inertial focusing of 2 µm red and 920 nm green fluorescent polystyrene spheres using an asymmetric serpentine channel. **Figure 2.1a**, at the center of Figure 1, shows the top-view a schematic of the entire microfluidic device, for which there are five functional components: (1) an inlet to introduce the homogeneous suspension; (2) a filter region to prevent channel clogging by trapping larger particles; (3) a 33.3 mm-long asymmetric serpentine channel to focus the particles (doubling back to reduce the device length); (4) a separation region to isolate particle streams from media; and (5) three collection outlets. The serpentine microchannel geometry was selected because it enhances the rate of lateral particle migration. That is, at a sufficiently large value of the Dean number (*De*), at which point the Dean drag the same order of magnitude as the lift force, curved channels result in faster focusing to predicted equilibrium positions than straight channels for the same Reynolds number[16,30]. It is noted that the lift force is the dominant focusing mechanism moving particles to their equilibrium positions; the additional force from Dean flow does not focus particles, but it serves to reduce the number of equilibrium positions from four to one and to speed up the focusing process. Due to the small size of the particles, a correspondingly small channel cross section is needed to enable and maintain inertial focusing.

In studies with 2 µm particles and bioparticles, the microchannel height is a uniform 10 µm and the serpentine channels have a width of 20 µm on the small curvature bends, both of which are critical parameters that determine focusing performance. One small and one large turn is defined as a unit, such that the length of 3 units is 1 mm. The separation channels are designed to range from 12 units (4 mm) to 100 units (33.3 mm). Figures. 2.1b’, c’ and d’ show the progression of inertial focusing processes for 2 µm red fluorescent polystyrene spheres in a 12-unit configuration. The particle suspension is introduced into the inlet by a syringe pump, and the suspension enters the serpentine channel region after passing through the filter. At the beginning of the suspension section (Figure. 2.1b’), the band of red fluorescent particles spans the width of the microchannel. However, as the suspension passes through the units, the width of the particle stream continuously narrows to the point where the particles are focused (Figure. 2.1c’). After the focused stream leaves the serpentine section it is isolated from the particle-free liquid in the separation region.

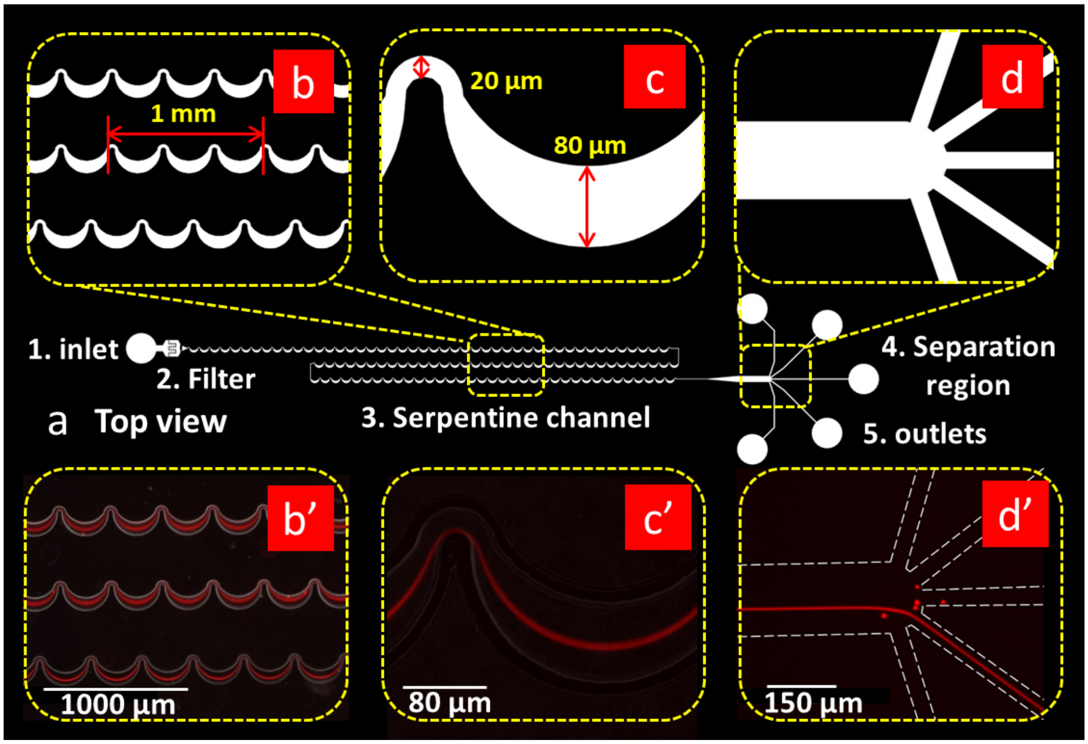

Figure 2.1 Images showing the design and use of a serpentine microfluidic network for focusing for 2µm red fluorescent spheres. (a) A schematic top view of the entire inertial focusing platform. The total length of the serpentine curved microchannel section is 4.5 cm in this design. (b) Enlarged image of the serpentine curved channel. (b’) Fluorescence image of the 2µm red fluorescence particles streams in locations corresponding to (b). (c) Magnified image of one serpentine unit, in which the channel width of the small bend is 20 µm and the width of the large bend is 80 µm. (c’) Fluorescence images of the focused 2µm red fluorescence particle stream at a location corresponding to Figure (c). (d) Magnified image of the

isolation region. (d’) Fluorescence images of the focused 2μm red fluorescence particle stream in the isolation region. The white dashes represent the boundaries of microchannels.

As discussed above, the small size of the particles requires a higher flow rate (*Re*) relative to larger particles, to obtain a sufficiently large lift force. And because of the linear relationship between flow rate and pressure drop per unit length in Poiseuille flow, significant pressure is applied to the liquid. Under these circumstances, despite its fabrication simplicity and widespread use, PDMS is a not an appropriate choice for the microchannel material; pressure-induced deformation of the channel cross section results in a total loss of the focusing effect.[21,23] Thermoset polyester (TPE) was identified as an alternative polymeric material with similar fabrication procedures to PDMS as well as optical transparency, but with much higher rigidity.[21] Young’s modulus for TPE is approximately 1.2 GPa, or 1,000× higher than 1:10 PDMS.[21] The inertial focusing microfluidic chip was fabricated in TPE by single-layer soft photolithography with several processing changes from reported methods [33–37] to obtain needed versatility for a wider range of applications. First, a 3 min UV light curing step[33,35,37] was replaced with a 10 min 65°C thermal cure. This modification eliminates the need for photo initiator in the resin mix for UV curing, and results in improved optical transparency of the TPE layer and also reduces the cost for chip fabrication. Second, although fully cured TPE is a rigid polymer, it was still possible to use standard PDMS punches to create inlet and outlet ports by doing a partial thermal cure, punching the inlets and outlets, and then completing the cure with room temperature O_2 plasma treatment for sealing. The detailed procedure is illustrated in supplementary **Figure. 2.2** and described in Materials and Methods.

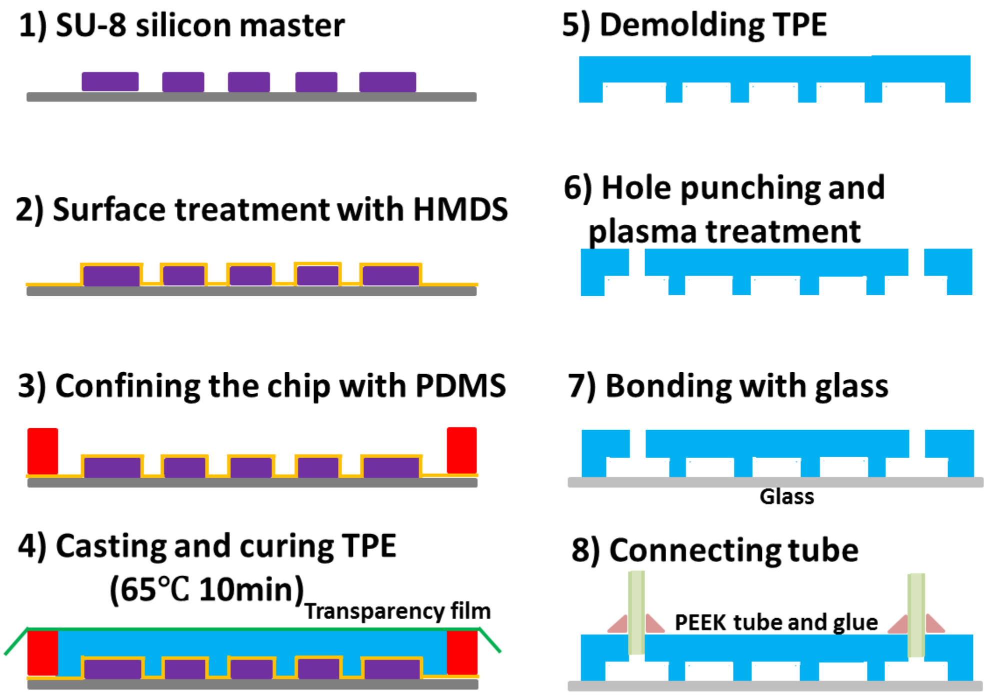

Figure 2.2 Schematics illustrating the procedure to fabricate the thermoset polyester (TPE) inertial focusing microfluidic system.

2.3.2 Effect of Particle Size.

Within the curved channel region, the theory associated with the superposition of the lateral lift forces and secondary flow is complicated, but there is a dimensionless parameter, the inertial force ratio,[16] that quantifies the magnitude of this effect:

$$R_f = \frac{a^2 R}{h^3} \tag{2}$$

This parameter contains the particle size a, the largest radius of curvature, R, and the smallest channel dimension, which is h in this device. When $R_f > 0.04$, the coupling of lift force and Dean flow will guide particles to a stable equilibrium position.[16] By design, for the 2 µm particles in the network shown in Figure. 2.1 the ratio is $R_f = 0.6$, which is well above the necessary threshold. **Figure. 2.3**b shows results for focusing experiments with a 0.01 v/v%

suspension of the 2 µm spheres at a flow rate of 500 µL/min (*Re* = 554). The streak width, that is, the full width at half maximum (FWHM) of the intensity profile is 2.12 µm at this flow rate. When the measured FWHM is less than twice the particle diameter, the particle stream is defined as focused.[16] There is a common view that it is difficult to precisely focus microparticles in asymmetric serpentine channels [38] because the steak widths are often two to three times the particle diameter in size.[27,39] However, the results from this study show that the streak width is essentially the same as the particle diameter at low particle concentrations, strongly indicating that the suspension flows single file along a pathline. The ability to truly focus particles in a curved channel network depends strongly on two quantities, the flow rate and channel cross section dimensions. As indicated above, the Reynolds number in this experiment significantly exceeds 100, which is a typical value reported in other inertial focusing studies.[27,39] This operating condition is clearly important since the magnitude of the lift force scales as the square of the maximum fluid velocity, as shown in **equation (1)**. At the same time, the magnitude of the secondary flow velocity, U_D, also varies as the square of that maximum velocity as

$$U_D \approx \frac{De^2 \mu}{\rho h} \tag{3}$$

where $De = Re(h/2R)^{1/2}$ is the Dean number, and µ and ρ are the liquid dynamic viscosity and density, respectively.[18] For these studies the cross-section dimensions and particle size are fixed, so flow rate plays a major role in the focusing process. The reason that the focusing effect is lost under these conditions when using PDMS is also evident in equation (1); the higher pressure expands the channel cross section like a balloon, resulting in unwanted increases in D_h.

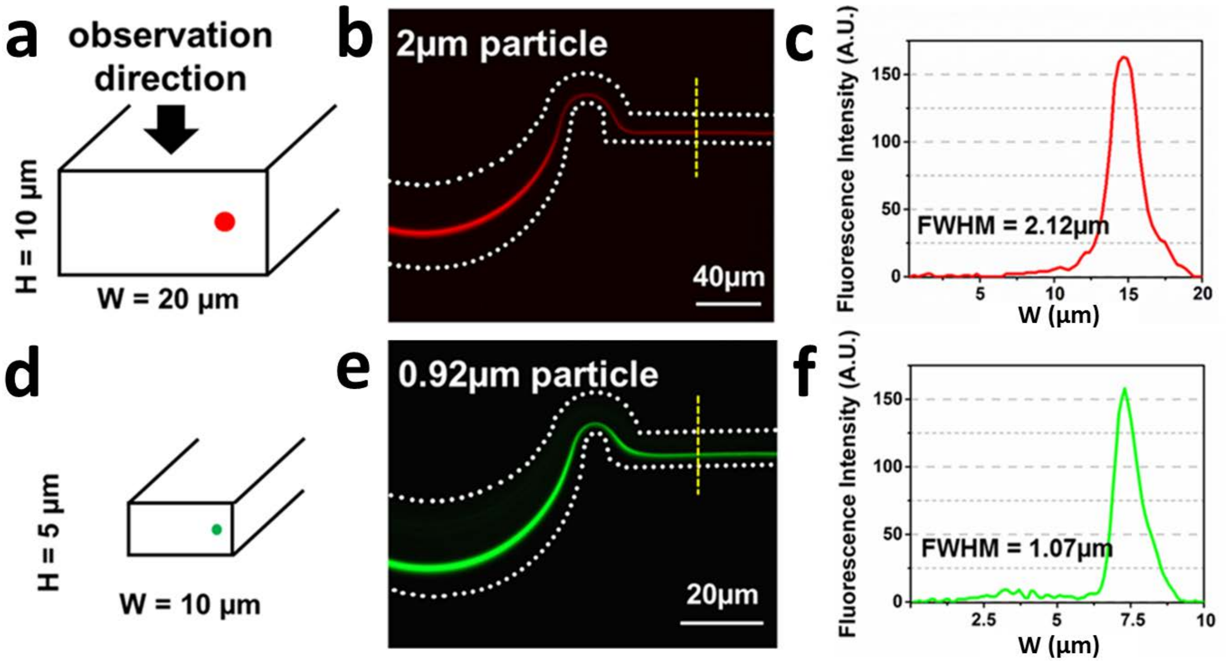

Figure 2.3 The effect of particle size on focusing efficiency. (**a**) The channel cross-section of 20 µm × 10 µm is designed for 2 µm particle focusing. (**b**) Fluorescence image of 2 µm red fluorescent particles in the final curve of the serpentine microchannel. A single equilibrium focusing location is seen in the straight channel region. (**c**) The corresponding fluorescence intensity profile across the width (w) of the straight channel region. (**d**) The channel cross-section of 10 µm × 5 µm is designed for 0.92 µm particle focusing. (**e**) Fluorescence image of 0.92 µm green fluorescent particles in the final curve of the same serpentine microchannel. (**f**) The corresponding fluorescence intensity profile across the width (w) of the straight channel region. The FWHM is calculated from a fitted Gaussian curve. The white dashed lines represent the microchannel boundaries.

A suspension of smaller 0.92 µm spheres was also flowed through this serpentine network at the same flow rate and concentration as the 2 µm spheres. As shown in supplementary **Figure. 2.4**, the FWHM streak width is 4.10 µm, which is 4.5 times the 0.92 µm sphere diameter. This relatively reduced focusing effect is simply due to the smaller particle size and resulting net lift force. However, despite the fact that these particles are, technically, not focused, the lift ratio is R_f = 0.13 and the relative narrowness of the streak width is significant because the magnitude of the lift force on the 0.92 µm spheres is less than 5% of that experienced by 2 µm spheres. The inertial migration effect isn't sufficiently large enough to more tightly group the smaller particles, but it nevertheless displaces them with surprising efficiency. These results indicate that further tuning of channel dimensions offers the possibility of focusing submicron particles. In follow on studies, a microchannel with reduced cross-section (w= 10 µm and h= 5 µm) was designed and tested with the 0.92 µm green fluorescent microspheres at the same flow rate. There, the FWHM is 1.07 µm, as shown in Figure. 2.3 f. This result demonstrates that submicron-sized particles can also be focused using inertial forces. One disadvantage of this separation technique is that the fixed channel dimensions constrain operation to a relatively narrow range of particle sizes. However, it is possible to design a serial microchannel network configuration with different channel cross-section dimensions in each stage or segment, whereby particles are focused and removed in order of decreasing particle size. For similar-sized particles (e.g., 2 µm and 3 µm), a single channel could be used to produce a separation of the two sizes. Both sizes would be focused, but on distinguishable pathlines, and the outlet microchannel configuration designed based on knowledge of the different equilibrium positions.

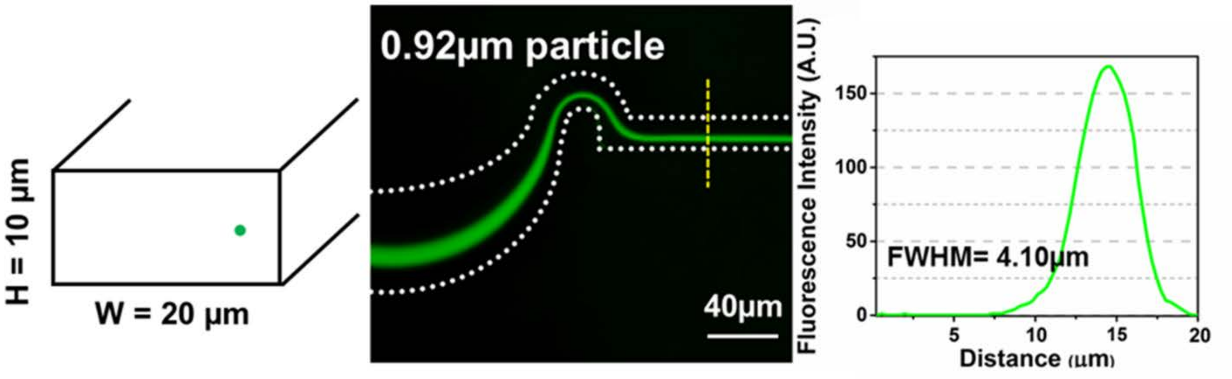

Figure 2.4 Fluorescence image of 0.92 µm-sized green fluorescent particles in the final curve of the serpentine microchannel. The corresponding fluorescence intensity profile across the width of the straight channel region (w = 20 µm, h = 10 µm). The FWHM is calculated from a fitted Gaussian curve. The white dashed lines represent the microchannel boundaries.

2.3.3 Effect of Channel Length.

The channel length is ultimately a critical factor in fabrication cost and power consumption, as well as the ability to scale up to process larger volumes, e.g., in the mL/s range. A logical issue to address, then, is the minimum length of the serpentine section required to focus the micron-sized particles. Typical channel lengths reported in the literature are on the order of several centimeters.[14,17,38,39] In this study, 100 units of the serpentine channel (33.3 mm total length) were chosen for focusing the 2 µm spherical particles in large part because of much lower flow rates that were initially investigated.

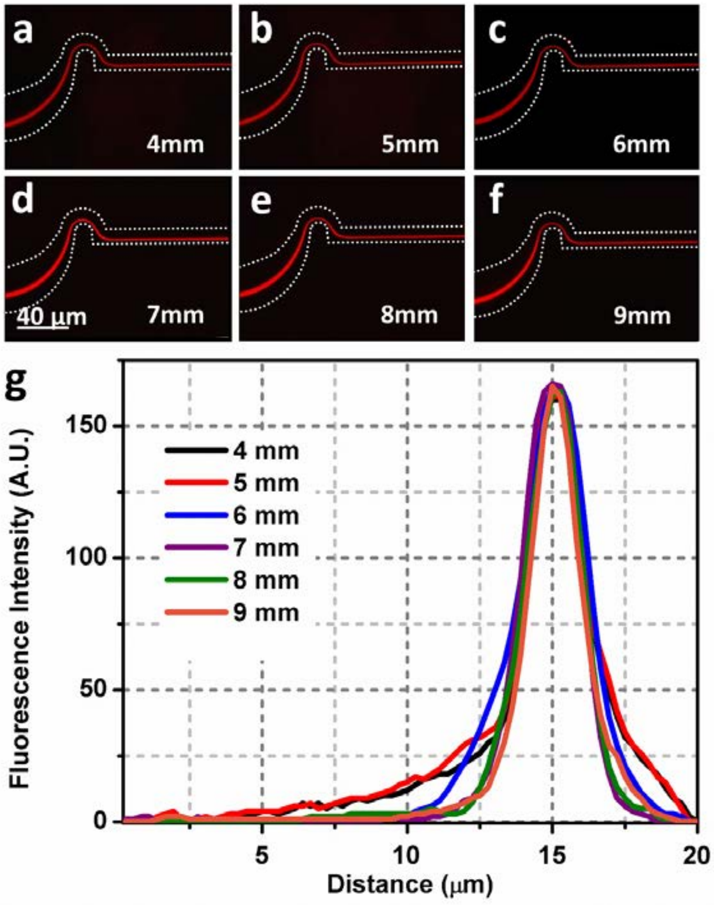

Figure 2.5 The dependence of focusing efficiency on serpentine focusing region length. (**a**) – (**f**) Fluorescence images of 2 µm red fluorescent particles in the final curve of serpentine microchannel for channel lengths ranging from 4mm to 9mm. (**g**) The fluorescence intensity profiles across the width of the straight channel for each of the serpentine channel lengths. The white dashes represent the microchannel boundaries.

As shown in **Figure. 2.5**, this length did result in very good focusing characteristics. Subsequently, serpentine channel lengths ranging from 4 mm to 9 mm have been designed and tested. The flow rate is fixed at 700 µL/min (*Re* = 776) in all runs, and the 2 µm fluorescent spheres introduced at a concentration of 0.01 v/v%. The fluorescence images and scanned profiles are shown in Figure. 2.5 For all of the different channels lengths the microspheres are tightly focused into a single particle stream and the lateral position of each particle stream is the same regardless of focusing region length. The minimum serpentine channel length considered here, 4 mm, is almost one tenth that of the most reported inertial focusing channel lengths.[14,17,22,38]

To investigate the minimum length of serpentine channel required to focus 2 µm particles, additional serpentine channels, ranging in length from 1 mm to 4 mm, were designed and tested with a 0.01 v/v% suspension concentration. The resulting fluorescence images for these different microchannel lengths are shown in Supplementary **Figure. 2.6** for a range of flow rates. The degree of focusing as a function of flow rate and channel length follows an interesting pattern. In the longest channel (4 mm), the 2 µm particles are focused at all flow rates 100 µL/min and higher, whereas in the 3 mm microchannel the particles are only focused at intermediate flow rates; and in the 2 mm microchannel focusing only occurs at a single flow rate. In the shortest channel, focusing isn't observed at any flow rate. Together, these results indicate that a minimum channel length (6 serpentine units, or 2 mm) and a minimum flow rate (100 µL/min) are both required to successfully focus 2 µm particles. An important advantage gained by obtaining a shorter focusing distance is decreased hydraulic resistance, and therefore, decreased pressure drop and power required to drive the flow.

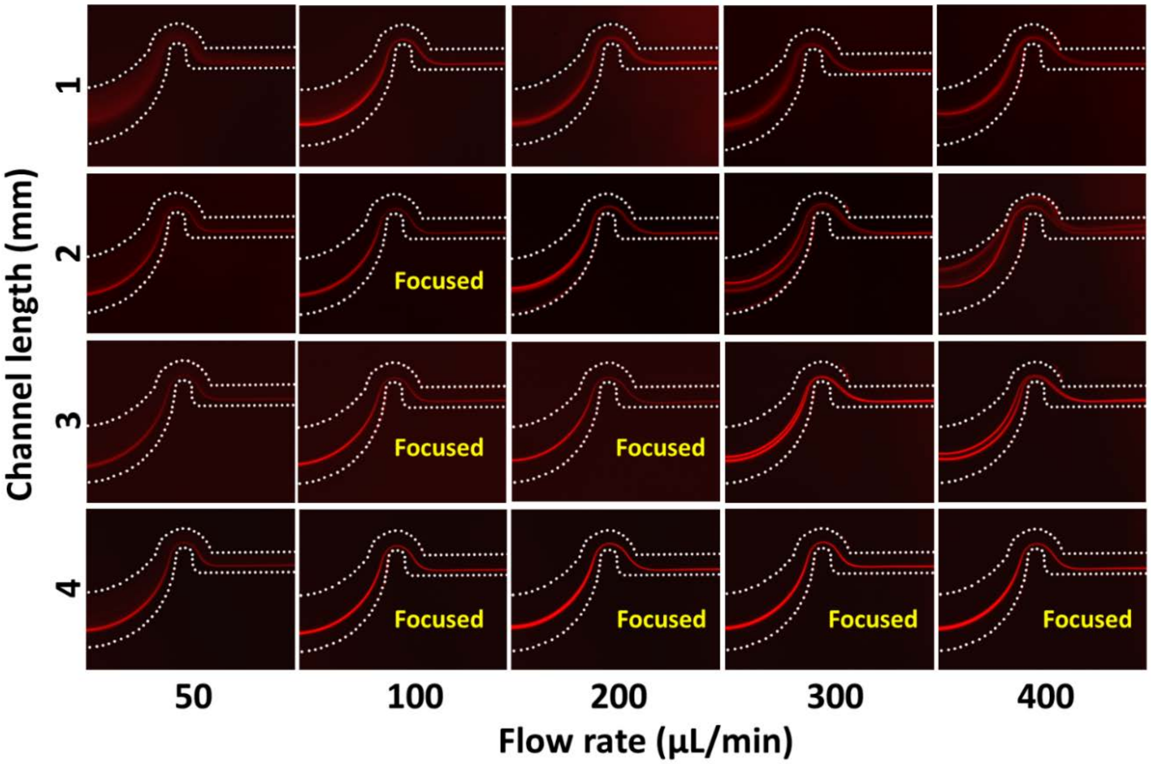

Figure 2.6 The minimum serpentine microchannel length required for inertial focusing of micron-sized particles. Fluorescence images of 2 μm red fluorescent particles in the final curve of the serpentine microchannel for serpentine channel lengths ranging from 1 mm to 4 mm and flow rates ranging from 50 μL/min (*Re* = 55.4) to 400 μL/min (*Re* = 443). The white dashed lines represent the microchannel boundaries.

2.3.4 Effect of Flow Rate.

Just as reducing channel length increases throughput-per-footprint, so does an increase in the maximum practical flow rate. To further explore the effect of this parameter on device operation, a range of flow rates, from 10 μL/min (*Re* = 11.1) to 1,400 μL/min (*Re* = 1,550) were investigated. **Figure. 2.7** shows fluorescence images in the straight channel section immediately downstream of the serpentine region, as well as the intensity scan across the channel width. It may be seen that, for this 0.01 v/v% concentration, the degree of focusing continuously improves as flow rate is increased from 10 μL/min (*Re* = 11.1) to 100 μL/min (*Re* = 111). As the flow rate is increased beyond this value, however, there is no noticeable effect on focusing because the particles already lie on a single pathline. This result is in contrast to observations made in straight focusing channels at similar values of *Re*.[23] Specifically, in another study using straight focusing channels, the number of focused streams varied from one to three as flow rate increased.[23] This difference is consistent with the observation that Dean flow in serpentine channels efficiently aligns the particles into equilibrium positions that remain stable in the downstream straight channel section, and enables focusing to a smaller subset of equilibrium positions that are stable in the presence of the superposed secondary flow. As for the correlation between the strength of the secondary flow and the particle distribution, there is no straightforward relationship because a number of parameters (e.g., microchannel dimensions, particle size, channel radii of curvature, and Reynolds number) are involved, as indicated in the expressions above for the inertial force ratio and Dean number. In this design, the only adjustable parameter is Reynolds number. Therefore, the magnitude of secondary flow and Reynolds number are proportionally related by a constant. One thing that does vary with the Reynolds number or secondary flow in the current system is the lateral equilibrium position of the focused stream. Although the effect is small, the particle stream moves closer to the channel sidewall as Reynolds number or secondary flow strength is increased. Note that the apparent width of the particle streams is larger at higher flow rates. This effect is an artefact of the visualization technique that results in an increased number of particles passing through detection region during the same exposure time.

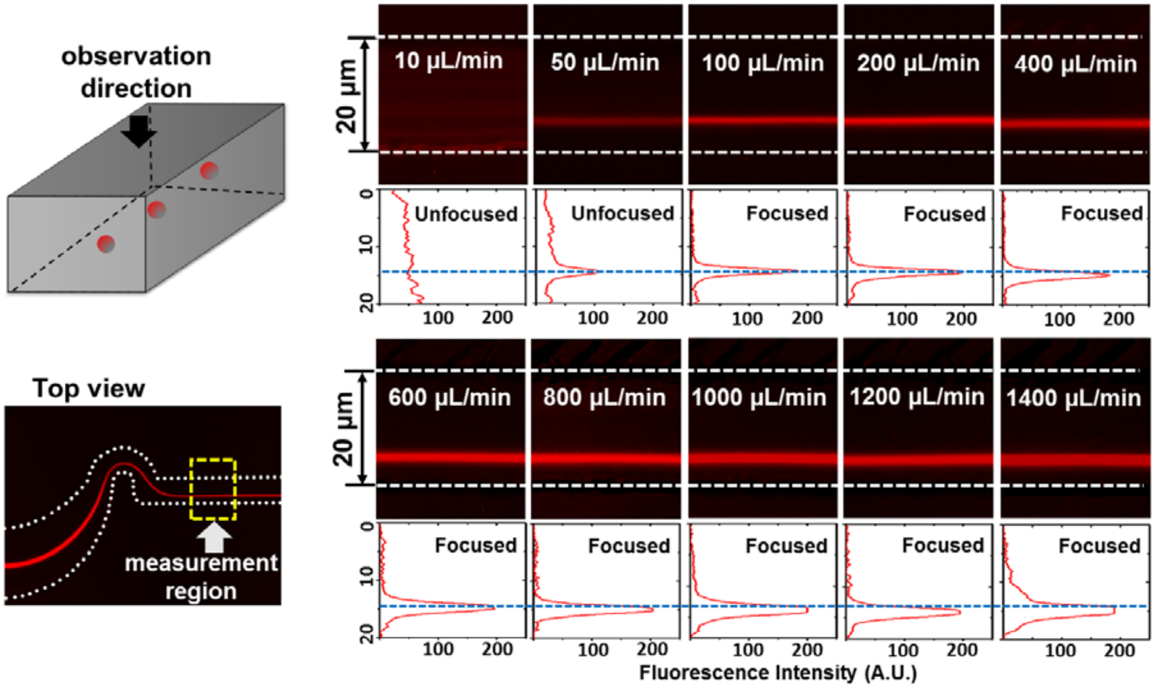

Figure 2.7 Flow rate dependence of inertial focusing efficiency for micron-sized particles. The left two images show the observation direction and observation region for the images on the right. The intensity images and scans show the fluorescence intensity from 2 µm particles under the flow rates ranging from 10 µL/min (*Re* = 11.1) to 1400 µm/min (*Re* = 1550). The horizontal blue dashed line in each scan demonstrates the shift in particle streak location toward the sidewall as flow rate is increased. The white dashes represent the microchannel boundaries.

2.3.5 Effect of Suspension Concentration.

Another important feature of a high throughput device is the ability to focus and separate a wide range of suspension concentrations, while at the same time, recognizing that this phenomenon is concentration dependent.[16,27,38]. Specifically, focusing suspensions with high concentrations can be problematic due to particle-particle interactions that work against the lateral lift force mechanism. As shown in **Figure. 2.8**a, the width of focused 2 µm particle streams increases as particle concentration increases from 0.01 v/v% (FWHM = 2.07 ± 0.03 µm) to 1 v/v% (5.98 ± 0.03 µm). For these experiments, the flow rate was held constant at 1000 µL/min and the serpentine channel length was 4 mm. The images and plots in Figure. 2.8

illustrate several phenomena. First, the FWHM of the particles streams are much less than twice the particle diameter when the particle concentrations are low (0.01 and 0.1 v/v%), which conclusively demonstrates focusing,[24] as shown in the lower left (pink) region of Figure. 2.8b. Second, the locations of the particle streams do not change appreciably as particle concentration increases. Third, it is found that, at 1 v/v%, the FWHM of the stream is 5.98 µm, which is almost three times the particle diameter. Based on the standard definition applied at the lower concentrations,[24] this stream would be considered unfocused. However, simply due to geometric constraints there is a tendency for the particles to line up on adjacent pathlines and form "particle trains".[40] To explain this higher concentration phenomenon, a length fraction λ is introduced, where this quantity is the number of particle diameters per channel length[16]. The length fraction (λ) can be related to the suspension volume fraction as

$$\lambda = \frac{aA_cV_f}{V_p} = \frac{6whV_f}{\pi a^2} \tag{4}$$

where V_f is the suspension volume fraction, A_c is the channel cross-sectional area, w is the channel width, and h is the channel height.[16] In theory, when $\lambda < 0.5$, there can be a single train of aligned particles; the minimum number of particle trains increases from one to two when $\lambda > 0.5$, which is shown in the middle region (green) in Figure. 2.8b, and then three trains when $\lambda > 1$, represented by the rightmost (blue) region.[40] For the suspension concentrations used here, the corresponding λ values are 0.0095 (0.01 v/v%), 0.0955 (0.1 v/v%), and 0.9549 (1 v/v%), as shown in Figure. 2.8b. There needs to be a minimum of two particle trains when the suspension concentration is 1%, and the focusing criterion is thereby adjusted to be FWHM $\leq 2aN_t$, where N_t is the minimum possible number of particle trains. In this study, then, the 1.0 v/v%

suspension is focused because the FWHM < 8 µm. The upper limit of length fraction considered in this study is 1 to avoid defocusing due to strong particle interactions and crowding.[38]

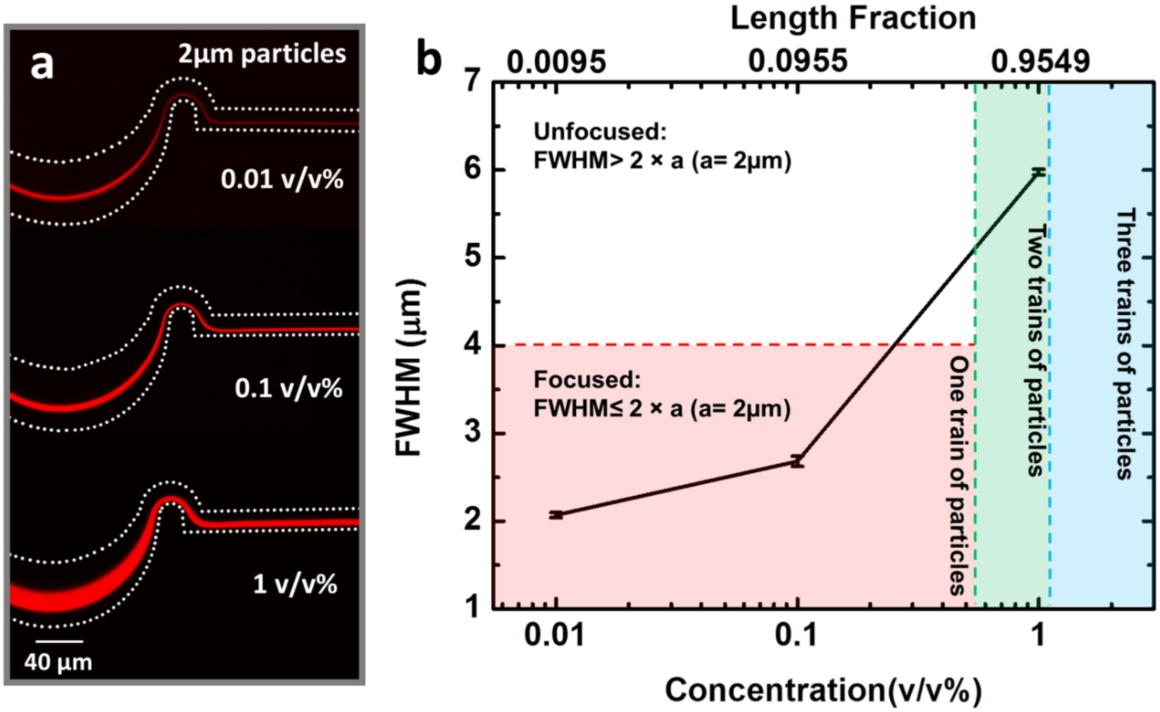

Figure 2.8 The dependence of focusing efficiency on the initial suspension concentration for 2 µm particles. (**a**) The measured FWHM visibly increases as particle concentration is increased. (**b**) The lower left region (pink) denotes the range of 2µm particle concentrations that theoretically can be focused onto a single particle train (pathline). The data points in this region demonstrate that focusing is achieved. The region above this (white) represents unfocused operation. The adjacent region (green) corresponds to a range of particle concentrations (~0.52 to 1.05 v/v%) that cannot physically fall onto a single pathline, but may form two adjacent particle trains. Using this as a focusing criterion, the results for the 1 v/v% suspension indicate that focusing is achieved. The final region in the plot (blue) demotes focusing for concentrations above ~1.05 v/v%. The white dashes represent the microchannel boundaries. Error bars represent standard deviation with a sample size of three.

As discussed above, this device is effective at focusing a dilute suspension (0.01 v/v%) of 2 µm particles at high flow rates, up to 1400 µL/min, using short (4 mm) channel lengths. The ability of the device to focus and concentrate higher suspension densities—0.1 and 1.0 v/v%—was also quantified. For the outlet configurations shown in Supplementary **Figure. 2.9**a, concentration performance (yield efficiency) was measured. As shown in Supplementary Figure.

2.9b, at 500 µL/min, the yield efficiencies for the higher concentrations (0.1 v/v% and 1 v/v%) rival the performance of the lowest concentration (0.01 v/v%). At 700 µL/min (Supplementary Figure. 2.9c), the yield percentage is similar to the 0.01% performance, that is, above 99%. Thus, a concentration factor of over 100 with high yield efficiency is feasible if the channels were configured as a cascade, with the product stream of one flowing to the inlet of another.

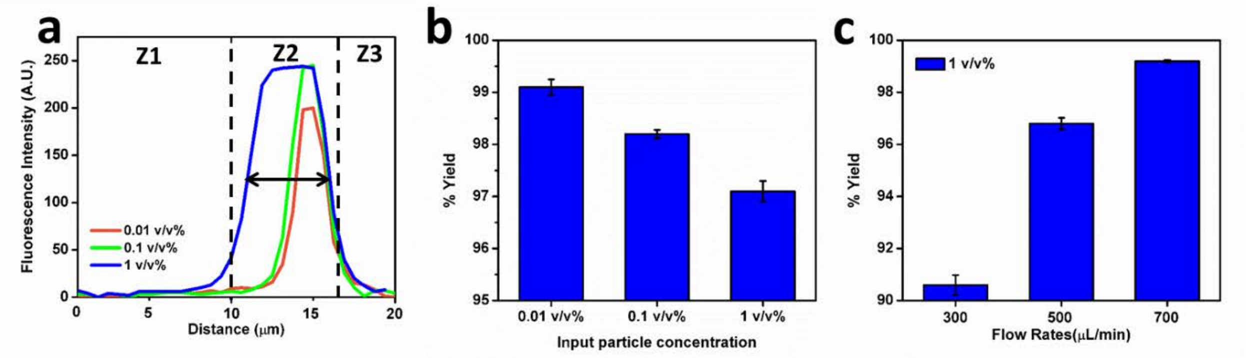

Figure 2.9 The concentration profiles of the 2 µm particle suspensions for a range of inlet suspension densities. (a) The outlet design is based on the predicted locations of focused particle streams for separation into three zones. Z1 and Z3 are intended for the waste (particle-free) streams, and Z2 is designed for the concentrated product stream. (b) The yield percentage of 2 µm particles at a flow rate of 500 µL/min. (c) the yield percentage of 2 µm particles in the 1 v/v% suspension at three different flow rates. Error bars represent the standard deviation with a sample size of three.

A suspension concentration of 0.01 v/v% is equivalent to 10^7 mL^{-1}, and this is approximately the highest concentration of cyanobacteria in a fully cultured state (e.g., in an open pond).[41] In other words, a 0.01 v/v% concentration covers most of the applications in industrial or laboratory settings, for example, bacteria sample pre-concentration for nucleic acid extraction, or bacteria separation in water or milk. For some specific industry applications, highly concentrated bacteria suspensions are needed to extract bio-products. Cyanobacteria-based biofuel production is a good example for this. The suspension concentration after the culture process is not high enough in these applications for harvesting or dewatering to be economically feasible, and additional processes are needed to further increase the concentration.

The higher working concentrations of 0.1 v/v% (10^8 mL^{-1}) and 1.0 v/v% (10^9 mL^{-1}) tested in this microfluidic device demonstrate that the technique is suitable for such applications.

2.3.6 Micron and submicron particle separation.

There have been several recent investigations into separating micron and submicron particles using microfluidic platforms. [42,43] Among these, there are few reports of inertial focusing based particle separations in the micron and submicron range, but in one a spiral configuration was used to separate 3.2 µm and 2.1 µm particles, with 1.0 µm particles remaining unfocused.[22] At the same time, the separation of micron- and submicron-sized particles/bioparticles has significant utility. For example, the separation of rod-shaped bacterial cells (200 nm × 2 to 8 µm) from virus particles (20 to 200 nm) has immediate clinical utility as part of sample preparation or purification. In this study, separation experiments have been carried out for particles ranging from 2 µm to 200 nm. Merged fluorescence images and intensity profiles of individual particles are shown in **Figure. 2.10**. In the 20 µm × 10 µm serpentine microchannel, 2 µm particles with 920 nm or 200 nm particles were studied to demonstrate the device's ability to separate a typical bacterial cell from virus. At a modest flow rate (80 µL/min), the 2 µm particles (red) can be focused while the 920 nm particles (green) remain diffuse. Although the 2 µm and 920 nm particles are relatively close in size, this work represents the first time that these two sizes have been separated using inertial focusing. The 10 µm × 5 µm serpentine channel was then used to demonstrate the extraction of 200 nm particles (0.01 v/v%) from a mixture with 920 nm particles (0.01 v/v%). The 920 nm particles (green) equilibrated near the wall of microchannel, while the 200 nm particles (red) remain unfocused and evenly distributed. This approach can be used for separation of nanoparticles and bioparticles such as bacteria and virus.

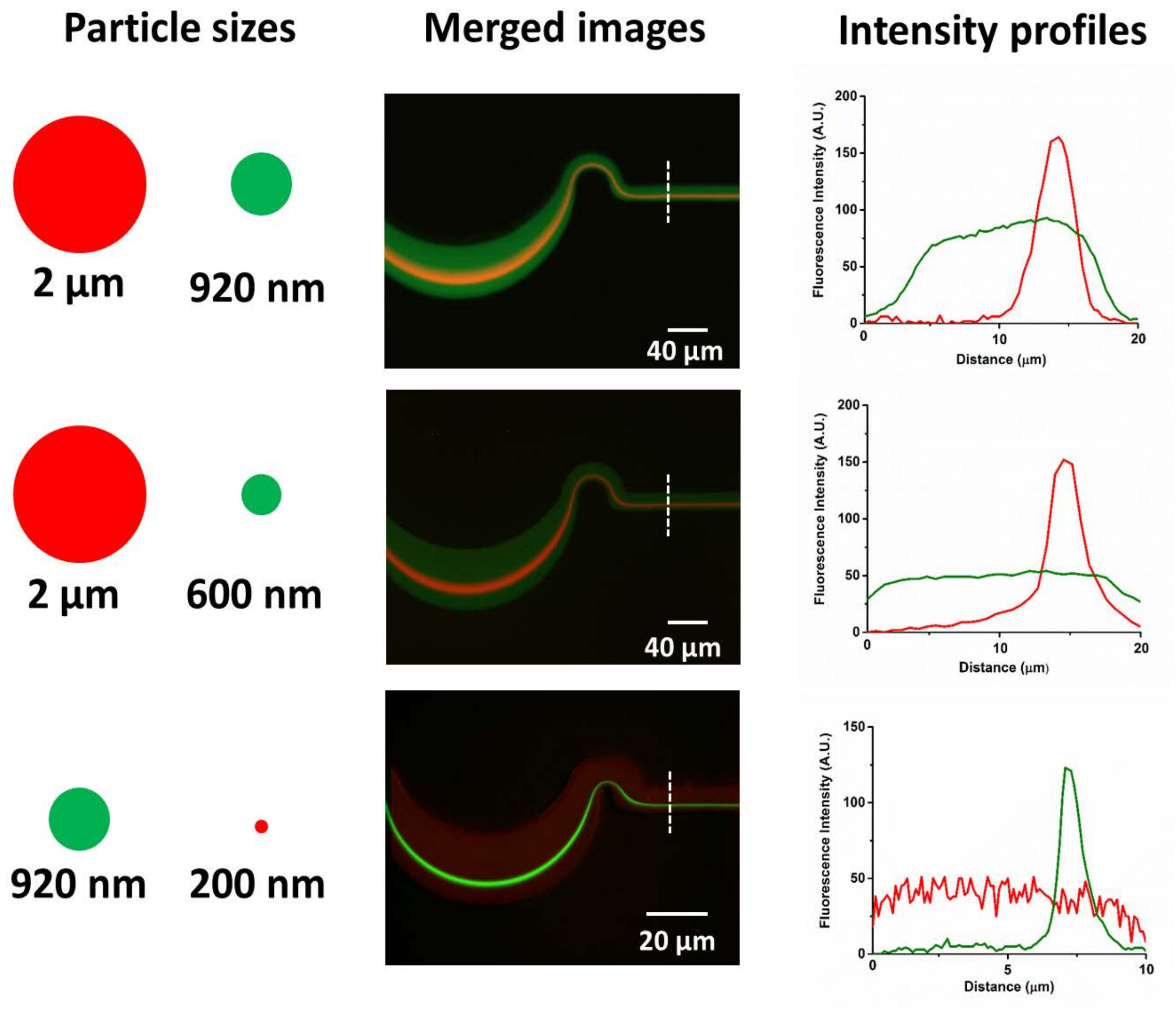

Figure 2.10 Micron and submicron particle separation. The left legends show the relative particles sizes and their corresponding florescence colors; the middle images are the merged fluorescence photos of two particles with difference sizes tested in the same microchannel at the same flow rates; the right plots are the intensity profiles of corresponding particles.

2.3.7 Application to Bioparticles.

Although rigid particles have been used here as a simple model to quantify inertial focusing effects on micron-size particles, bioparticles are typically not rigid and will deform under normal and shear stresses present in the flow field. To determine the effects of deformability on focusing, a suspension of Cyanobacterium *Synechocystis* sp. PCC 6803, with a typical size of 2 µm[44] was introduced into a microfluidic chip with a 4 mm-long serpentine section. The cyanobacteria used here have been modified to express GFP.[45]

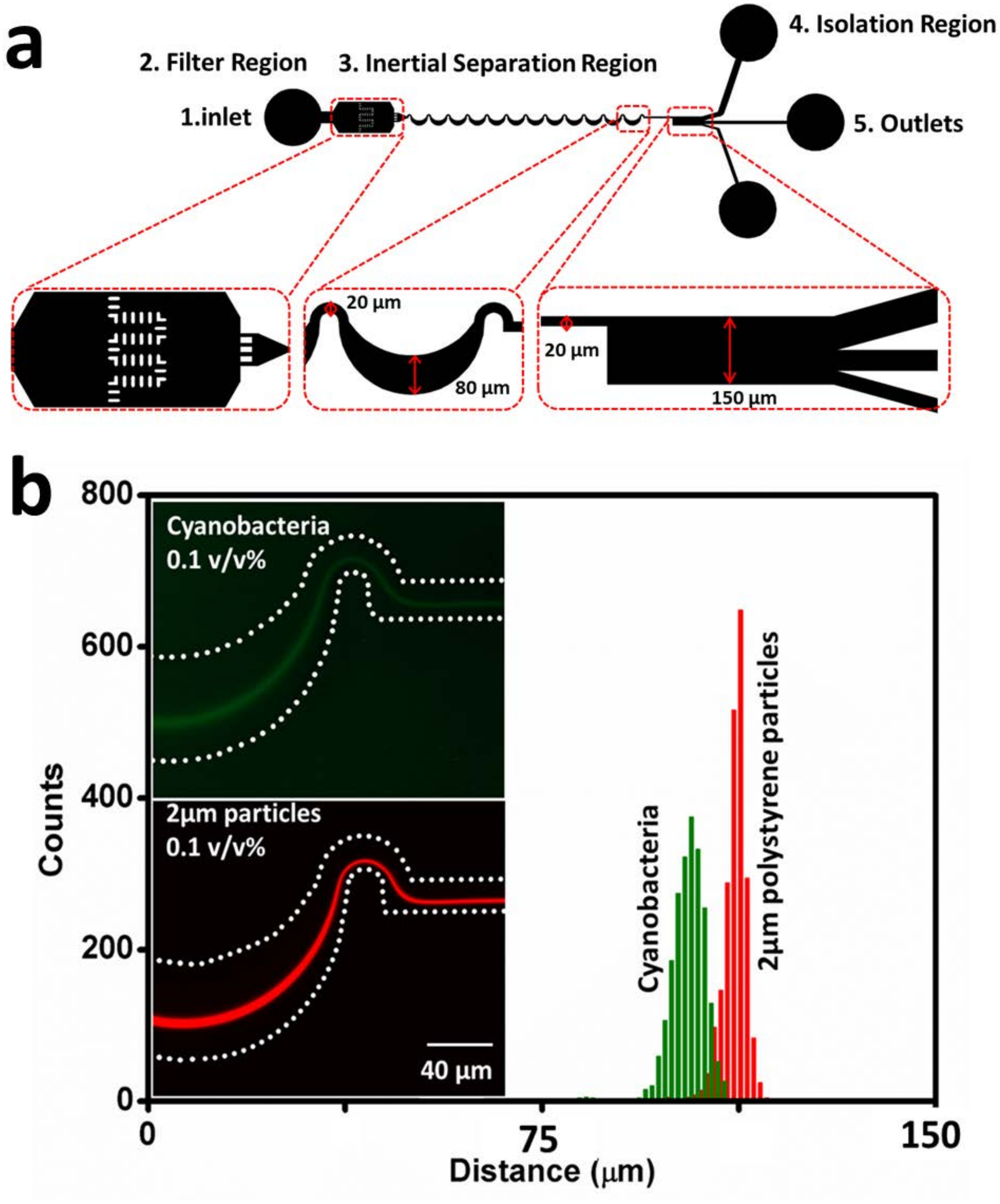

Figure 2.11 The dependence of equilibrium particle streak location on particle deformability. (a) Schematics showing the layout of a serpentine microfluidic network for focusing for 2 µm spheres and cyanobateria. This figure represents a top view of the design, and enlarged images for each region. There are five functional components: an inlet for the homogeneous suspension, a filter region to prevent

downstream channel clogging, an asymmetric serpentine channel to focus the particles, an isolation region to separate the particle stream from liquid media, and three collection outlets. Green dots represent cyanobacteria pathlines. (**b**) The two fluorescence intensity images on the left part are the focused GFP-modified cyanobacteria and red fluorescent particles in the last curve. The white dashes represent the microchannel boundaries. Shown at right are fluorescence distribution histograms the 2 µm cyanobacteria and 2 µm particles across the width of the expanded isolation region leading to the three outlet channels.

Figure. 2.11 shows fluorescence images of the 2 µm cyanobacteria (0.1 v/v%) and 2 µm fluorescent polystyrene spheres (0.1 v/v%) at the final curve of the focusing region. For both cases the flow rate was 300 µL/min. A scan of the fluorescence intensity across the downstream isolation channel width demonstrates distinct differences in the equilibrium position of these comparably sized particles. To quantify this shift, the distributions of 5,000 counts of both 2 µm red fluorescent polystyrene particles and cyanobacteria across the straight channel section are plotted. The cyanobacteria peak is 1.05 µm closer to the centerline than the polystyrene spheres. This shift might be the result of the bioparticle's shape and deformability. Although most of the cyanobacteria are spherical in shape under quiescent conditions, they will form a transient ellipsoidal shape while undergoing division, as shown in Supplementary **Figure. 2.12** The equilibrium position of nonspherical particles depends on their largest dimension, and results in a shift in equilibrium position away from wall[19], but in this system the effect of particle shape is expected to be small. The phenomenon of a shift in equilibrium positions for rigid and deformable particles has also been observed in a study done to classify different cell types using size and deformability as distinguishing markers.[46] The equilibrium position shift observed in this study also appears to be due to the deformability of the cyanobacteria.[17] Our result indicates that bioparticle equilibrium position in this serpentine micro channel for micron-sized particles/bio-particles depends on their shape and deformability.

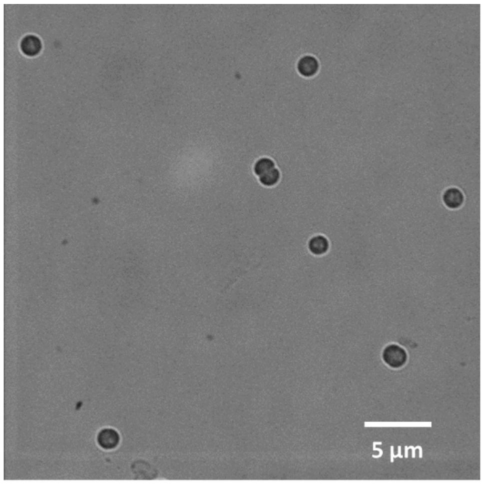

Figure 2.12 An image of cultured cyanobacteria at 100× magnification. Although most of the cyanobacteria are spherical in shape under quiescent conditions, they will form a transient ellipsoidal shape while undergoing division.

2.4 Conclusion

In this study, a serpentine channel inertial focusing microfluidic system has been designed, fabricated and tested to demonstrate that inertial migration and Dean flow can be effectively and efficiently applied to achieve focusing of dilute suspensions. The focusing of micron-sized particles was accomplished through two advancements: unique chip designs for 2 µm and 0.92 µm particles and the use of a rigid, easy-to-fabricate polymer. At flow rates greater than 100 µL/min, very tight focusing of 2 µm particles and cells is achieved with this new chip, and even sub-micron particles are focused on the chip in a predictable manner. To increase the throughput-per-footprint for processing large samples, a number of factors were systematically investigated, including the effects of channel length, flow rate, and particle concentration on inertial focusing. To ensure focusing of the 2 µm particles and cells, the minimum length of the serpentine channel is found to be 4 mm, which is significantly shorter than in other published studies. In this 4 mm chip, it was observed that a stable, focused particle stream was achieved for all flow rates between 100 µL/min and 1,400 µL/min. A wide range of suspension concentrations—from 0.01 v/v% to 1.0 v/v%—were tested in this chip, and it was found that 0.01 and 0.1 v/v% suspensions were focused according to the standard definition. The highest concentration, 1.0 v/v%, where the particles are geometrically constrained from occupying a single pathline, suggests that a new definition for focusing be adopted that takes into account the minimum number of adjacent pathlines or trains required to accommodate all of the particles in the suspension. It was also demonstrated that the device is capable of separating disparate sized particles from one another, in particular, particles with sizes characteristic of bacteria and virus. Last, the focusing performance of the chip for deformable bioparticles has been investigated, and it is found that bacterial cells are focused as effectively as rigid particles. This study has pushed the boundary in inertial focusing to demonstrate the ability to isolate and separate smaller, micron- and submicron-sized particles, which opens up new applications for bacteria and subcellular organelles in cytometry and digital microfluidics.

REFERENCES

[1] K. Zand, T. Pham, A. Davila, D. C. Wallace, and P. J. Burke, “Nanofluidic platform for single mitochondria analysis using fluorescence microscopy,” *Anal. Chem.*, vol. 85, no. 12, pp. 6018–6025, 2013.

[2] M. Shannon, P. W. Bohn, M. Elimelech, J. G. Georgiadis, B. J. Mariñas, and A. M. Mayes, “Science and technology for water purification in the coming decades,” *Nature*, vol. 452, no. March, pp. 301–310, 2008.

[3] H. Bridle, D. Balharry, B. Gaiser, and H. Johnston, “Exploitation of Nanotechnology for the Monitoring of Waterborne Pathogens: State-of-the-Art and Future Research Priorities,” *Environ. Sci. Technol.*, vol. 49, no. 18, pp. 10762–10777, 2015.

[4] A. Ahmed, J. V. Rushworth, N. A. Hirst, and P. A. Millner, “Biosensors for whole-cell bacterial detection,” *Clin. Microbiol. Rev.*, vol. 27, no. 3, pp. 631–646, 2014.

[5] A. I. Barros, A. L. Gonçalves, M. Simões, and J. C. M. Pires, “Harvesting techniques applied to microalgae: A review,” *Renew. Sustain. Energy Rev.*, vol. 41, pp. 1489–1500, 2015.

[6] S. O. Majekodunmi, “A Review on Centrifugation in the Pharmaceutical Industry,” *Am. J. Biomed. Eng.*, vol. 5, no. 2, pp. 67–78, 2015.

[7] B. W. Peterson, P. K. Sharma, H. C. van der Mei, and H. J. Busscher, “Bacterial cell surface damage due to centrifugal compaction,” *Appl. Environ. Microbiol.*, vol. 78, no. 1, pp. 120–125, 2012.

[8] L. B. Leverett, J. D. Hellums, C. P. Alfrey, and E. C. Lynch, “Red Blood Cell Damage By Shear Stress,” *Biophys. J.*, vol. 12, pp. 257–273, 1972.

[9] A. O. Ogunniyi, C. M. Story, E. Papa, E. Guillen, and J. C. Love, “Screening individual hybridomas by microengraving to discover monoclonal antibodies.,” *Nat. Protoc.*, vol. 4, no. 5, pp. 767–782, 2009.

[10] J. Warrick, B. Casavant, M. Frisk, and D. Beebe, “A microfluidic cell concentrator,” *Anal. Chem.*, vol. 82, no. 19, pp. 8320–8326, 2010.

[11] E. Molina Grima, E. H. Belarbi, F. G. Acién Fernández, A. Robles Medina, and Y. Chisti, “Recovery of microalgal biomass and metabolites: Process options and economics,” *Biotechnol. Adv.*, vol. 20, no. 7–8, pp. 491–515, 2003.

[12] C. Haber, “Microfluidics in commercial applications; an industry perspective.,” *Lab Chip*, vol. 6, no. 9, pp. 1118–1121, 2006.

[13] G. Segré and A. Silberberg, “Radial Particle Displacements in Poiseuille Flow of

Suspensions," *Nature*, vol. 189, no. 4760, pp. 209–210, 1961.

[14] D. Di Carlo, D. Irimia, R. G. Tompkins, and M. Toner, "Continuous inertial focusing, ordering, and separation of particles in microchannels.," *Proc. Natl. Acad. Sci. U. S. A.*, vol. 104, no. 48, pp. 18892–7, 2007.

[15] D. Di Carlo, J. F. Edd, D. Irimia, R. G. Tompkins, and M. Toner, "Equilibrium separation and filtration of particles using differential inertial focusing," *Anal. Chem.*, vol. 80, no. 6, pp. 2204–2211, 2008.

[16] D. Di Carlo, "Inertial microfluidics.," *Lab Chip*, vol. 9, no. 21, pp. 3038–3046, 2009.

[17] H. Amini, W. Lee, and D. Di Carlo, "Inertial microfluidic physics," *Lab Chip*, vol. 14, no. 15, pp. 2739–2761, 2014.

[18] J. Zhang, S. Yan, D. Yuan, G. Alici, N.-T. Nguyen, M. Ebrahimi Warkiani, and W. Li, "Fundamentals and Applications of Inertial Microfluidics: A Review," *Lab Chip*, vol. 16, pp. 10–34, 2016.

[19] J. M. Martel and M. Toner, "Inertial focusing in microfluidics.," *Annu. Rev. Biomed. Eng.*, vol. 16, pp. 371–96, 2014.

[20] E. S. Asmolov, "The inertial lift on a spherical particle in a plane Poiseuille flow at large channel Reynolds number," *J. Fluid Mech.*, vol. 381, pp. 63–87, 1999.

[21] E. Sollier, C. Murray, P. Maoddi, and D. Di Carlo, "Rapid prototyping polymers for microfluidic devices and high pressure injections," *Lab Chip*, vol. 11, no. 22, p. 3752, 2011.

[22] I. D. Johnston, M. B. McDonnell, C. K. L. Tan, D. K. McCluskey, M. J. Davies, and M. C. Tracey, "Dean flow focusing and separation of small microspheres within a narrow size range," *Microfluid. Nanofluidics*, vol. 17, no. 3, pp. 509–518, 2014.

[23] A. T. Ciftlik, M. Ettori, and M. A. M. Gijs, "High throughput-per-footprint inertial focusing," *Small*, vol. 9, no. 16, pp. 2764–2773, 2013.

[24] J. M. Martel and M. Toner, "Inertial focusing dynamics in spiral microchannels," *Phys. Fluids*, vol. 24, no. 3, pp. 1–13, 2012.

[25] J. Sun, M. Li, C. Liu, Y. Zhang, D. Liu, W. Liu, G. Hu, and X. Jiang, "Double spiral microchannel for label-free tumor cell separation and enrichment," *Lab Chip*, vol. 12, no. 20, p. 3952, 2012.

[26] M. E. Warkiani, G. Guan, K. B. Luan, W. C. Lee, A. A. S. Bhagat, P. K. Chaudhuri, D. S.-W. Tan, W. T. Lim, S. C. Lee, P. C. Y. Chen, C. T. Lim, and J. Han, "Slanted spiral microfluidics for the ultra-fast, label-free isolation of circulating tumor cells.," *Lab Chip*, vol. 14, no. 1, pp. 128–37, 2014.

[27] J. Oakley, D. Di Carlo, S. Graves, and M. Toner, “Particle Focusing in Staged Inertial Microuidic Devices for Flow Cytometry,” *Anal. Chem.*, vol. 82, no. 9, pp. 3862–3867, 2010.

[28] J. Zhang, S. Yan, R. Sluyter, W. Li, G. Alici, and N.-T. Nguyen, “Inertial particle separation by differential equilibrium positions in a symmetrical serpentine micro-channel.,” *Sci. Rep.*, vol. 4, no. ii, p. 4527, 2014.

[29] J. Zhang, W. Li, M. Li, G. Alici, and N. T. Nguyen, “Particle inertial focusing and its mechanism in a serpentine microchannel,” *Microfluid. Nanofluidics*, vol. 17, no. 2, pp. 305–316, 2014.

[30] D. R. Gossett and D. Di Carlo, “Particle focusing mechanisms in curving confined flows,” *Anal. Chem.*, vol. 81, no. 20, pp. 8459–8465, 2009.

[31] L. Wang, W. Liu, Y. Wang, J. Wang, Q. Tu, R. Liu, and J. Wang, “Construction of oxygen and chemical concentration gradients in a single microfluidic device for studying tumor cell-drug interactions in a dynamic hypoxia microenvironment.,” *Lab Chip*, vol. 13, no. 4, pp. 695–705, 2013.

[32] Y. E. Cheah, A. J. Zimont, S. K. Lunka, S. C. Albers, S. J. Park, K. F. Reardon, and C. A. M. Peebles, “Diel light: Dark cycles significantly reduce FFA accumulation in FFA producing mutants of Synechocystis sp. PCC 6803 compared to continuous light,” *Algal Res.*, vol. 12, pp. 487–496, 2015.

[33] G. S. Fiorini, M. Yim, G. D. M. Jeffries, P. G. Schiro, S. A. Mutch, R. M. Lorenz, and D. T. Chiu, “Fabrication improvements for thermoset polyester (TPE) microfluidic devices,” *Lab Chip*, vol. 7, no. 7, p. 923, 2007.

[34] J. Kim, A. J. deMello, S.-I. Chang, J. Hong, and D. O’Hare, “Thermoset polyester droplet-based microfluidic devices for high frequency generation,” *Lab Chip*, vol. 11, no. 23, p. 4108, 2011.

[35] G. S. Fiorini, R. M. Lorenz, J. Kuo, and D. T. Chiu, “Rapid prototyping of thermoset polyester microfluidic devices,” *Anal. Chem.*, vol. 76, no. 16, pp. 4697–4704, 2004.

[36] G. S. Fiorini, G. D. M. Jeffries, D. S. W. Lim, C. L. Kuyper, and D. T. Chiu, “Fabrication of thermoset polyester microfluidic devices and embossing masters using rapid prototyped polydimethylsiloxane molds.,” *Lab Chip*, vol. 3, no. 3, pp. 158–63, 2003.

[37] J. A. Vickers, B. M. Dressen, M. C. Weston, K. Boonsong, O. Chailapakul, D. M. Cropek, and C. S. Henry, “Thermoset polyester as an alternative material for microchip electrophoresis/electrochemistry,” *Electrophoresis*, vol. 28, no. 7, pp. 1123–1129, 2007.

[38] A. J. Chung, D. R. Gossett, and D. Di Carlo, “Three dimensional, sheathless, and high-throughput microparticle inertial focusing through geometry-induced secondary flows,” *Small*, vol. 9, no. 5, pp. 685–690, 2013.

[39] A. A. S. Bhagat, S. S. Kuntaegowdanahalli, N. Kaval, C. J. Seliskar, and I. Papautsky, “Inertial microfluidics for sheath-less high-throughput flow cytometry,” *Biomed. Microdevices*, vol. 12, no. 2, pp. 187–195, 2010.

[40] K. J. Humphry, P. M. Kulkarni, D. A. Weitz, J. F. Morris, and H. A. Stone, “Axial and lateral particle ordering in finite Reynolds number channel flows,” *Phys. Fluids*, vol. 22, no. 8, pp. 1–5, 2010.

[41] P. T. Pienkos and A. Darzins, “The promise and challenges of microalgal-derived biofuels,” *Biofuels, Bioprod. Biorefining*, vol. 3, no. 4, pp. 431–440, Jul. 2009.

[42] C. Liu, B. Ding, C. Xue, Y. Tian, G. Hu, and J. Sun, “Sheathless Focusing and Separation of Diverse Nanoparticles in Viscoelastic Solutions with Minimized Shear Thinning,” *Anal. Chem.*, p. acs.analchem.6b04564, 2016.

[43] M. Fouet, M.-A. Mader, S. Iraïn, Z. Yanha, A. Naillon, S. Cargou, A.-M. Gué, and P. Joseph, “Filter-less submicron hydrodynamic size sorting,” *Lab Chip*, vol. 16, no. 4, pp. 720–733, 2016.

[44] H. Iijima, Y. Nakaya, A. Kuwahara, M. Y. Hirai, and T. Osanai, “Seawater cultivation of freshwater cyanobacterium Synechocystis sp. PCC 6803 drastically alters amino acid composition and glycogen metabolism,” *Front. Microbiol.*, vol. 6, no. APR, pp. 1–10, 2015.

[45] S. C. Albers, V. A. Gallegos, and C. A. M. Peebles, “Engineering of genetic control tools in Synechocystis sp. PCC 6803 using rational design techniques,” *J. Biotechnol.*, vol. 216, pp. 36–46, 2015.

[46] A. J. Mach, J. H. Kim, A. Arshi, S. C. Hur, and D. Di Carlo, “Automated cellular sample preparation using a Centrifuge-on-a-Chip,” *Lab Chip*, vol. 11, no. 17, pp. 2827–2834, 2011.

CHAPTER 3: A MICROFLUIDIC CONCENTRATOR FOR CYANOBACTERIA HARVESTING[2]

3.1 Introduction

Although there is great opportunity and potential advantages for microalgae/cyanobacteria to replace significant quantities of petroleum-based fuels, these biofuels are not yet economically feasible at commercial scales. There remain a number of technical challenges to address in order for microalgae-based biofuels to become commercially viable [1]. These challenges include the production of sufficient algal biomass in bioreactors [2–3], metabolic engineering of new strains of that are sufficiently robust and productive [4-5], creation of a low-cost method to harvest the microalgae/cyanobacteria [1,6–8], and development of a life-cycle assessment tool to evaluate the sustainability, economics, and scalability of the entire production process [9]. Among the different processing steps, cell harvesting is a critical economic component, because it can account for 20 to 30% of the total cost [1,7,8]. The primary challenge for harvesting is the need to concentrate a suspension of dilute, micron-sized cells from 0.5 g/L (0.05 wt%) to 200 g/L (20 wt%), after which lipid extraction may be carried out with relatively high efficiency [10,11]. Many harvesting methods have been developed, such as gravity sedimentation, filtration and centrifugation. However, the cost of the traditional harvesting methods still failed to be economically feasible. The costs for the dewatering technologies include both capital and operational costs (e.g., power consumption, maintenance). The base case capital costs of settling ponds, membranes, and centrifuges discussed in a National Renewable Energy Laboratory (NREL) report are \$5.80/(m^3/day), \$178/(m^3/day) and

---

[2] This chapter is published in the following: Wang L, Dandy D.S., (2017) A Microfluidic Concentrator for Cyanobacteria Harvesting *Algal Res*, 26:481-489.

\$478/(m^3/day), respectively [1]. Thus, viable harvesting methods that are economically feasible and scalable for commercial use still need to be identified. Recently, there are a number of new or improved technologies under development, such as electrocoagulation [11], magnetic separation [7], and ultrasonic separation [1]. The investigation of emerging technologies may yield a harvesting strategy that meets needed efficiencies, costs, and longevity.

Microfluidic platforms provide a set of fluidic unit operations that enable the miniaturization, integration, and parallelization for specific applications. In contrast to isolated application-specific solutions, microfluidic platforms are designed for ready integration within a well-defined fabrication technology, allowing easy, fast, and cost-efficient implementation for a wide variety of different applications [12–14]. In addition, microfluidics technology is readily scalable to high volume, high throughput processes due to its intrinsic properties of miniaturization and parallelization [15–18]. An important characteristic of these platforms is that validation of a single microfluidic device’s working principles and subsequent optimization of its operating conditions is sufficient to demonstrate intrinsic scalability of the platform via a multilayer, parallelized design.

Inertial focusing in microfluidic devices is an emerging and robust approach to concentrate and isolate particles from a liquid medium based on size. The general approach capitalizes on microscale hydrodynamic physics resulting from flow through microchannels [19–22]. Due to the advantages of low device fabrication and operation costs, and throughput scalable to macroscale system requirements, inertial focusing microfluidics has been demonstrated as a promising approach for the continuous concentration of mammalian cells, and has replaced the need for centrifugation [23]. However, in contrast with most of the devices designed for operation with mammalian cells, which typically have a length scale greater than 10 µm, concentrating cyanobacteria-sized bio-particles (~2µm in size for Cyanobacterium *Synechocystis* sp. PCC 6803) remains a challenge using inertial microfluidics. Our previous work has demonstrated that inertial focusing could be applied to efficiently focus and isolate polystyrene microspheres with a size comparable to Cyanobacteria, in devices where substantial changes were made in microchannel design and fabrication [19–22].

In this study, a unique approach is presented that integrates microfluidics and cyanobacteria concentration, and which has significant potential for process throughput scale up that is required to meet large-scale biofuel production needs. The critical feature of this technology is its intrinsic scalability. Although the focus of this study is proof of principle, fabrication of a massively parallel microchannel network for processing large volumes, with multiple sequential stages for increased concentration factors, is anticipated to be a straightforward process. In this study, to demonstrate and quantify the new approach, the mechanism for concentration of 2 μm cyanobacteria is presented. Then, the specific design for harvesting cyanobacteria is described in detail and the fabrication steps for this polymeric prototype are outlined. High-speed camera images of the concentration and cell isolation process have been recorded, and were subsequently used to analyze cyanobacteria distribution patterns across the microchannel width. The associated effects of operating parameters such as flow rate and inlet suspension concentration were characterized based on the data from the video; from that data the harvest efficiency was evaluated using the measured concentration factor and recovery efficiency. Since the cost of algal harvesting is a major factor in the overall economics of large-scale operation, device fabrication cost and energy consumption (pumping cost) have been calculated and presented in this article.

3.2 Material and methods

3.2.1 Device Fabrication

The inertial focusing microfluidic device was fabricated using soft lithography [24] with thermoset polyester (TPE). First, the channel pattern was designed using AutoCAD (AutoCAD 2014, AutoDesk, Inc). Following that step the CAD design was printed at 20,000 dots per inch (dpi) onto a photomask. Then, a mold was fabricated in a single step process under a UV lamp (OmniCure S2000, Lumen Dynamics Group Inc., Ontario, Canada).

Before fabricating the microfluidic device, the mold was exposed to hexamethyldisilazane (HMDS) (Sigma-Aldrich, MO, USA) for 4 h at 60°C. A well-mixed and degassed resin (TAP Clear-Lite Casting Resin, CA, USA) with MEPK catalyst (TAP plastics, CA, USA) (resin: catalyst = 10:1 w/w) was poured on the mold and surrounded by a piece of PDMS, which confined the mix within the mold. A piece of transparency film (3M Scotchpak 9744, MN, USA) was used as a top cover over the mix to ensure a flat surface. Then, the mold with resin was baked for 8 min at 60°C, after which the TPE replica was peeled from the master. A biopsy punch (Technical Innovations, FL, Inc. USA) was used to create 1.5 mm diameter inlet and outlet ports.

To generate an enclosed channel, the TPE replica and a piece of glass substrate (or a piece of coverslip for high-speed camera imaging) are placed in a plasma chamber and pumped down to 200.3 mTorr, followed by purging with O_2 gas for 20 s. Then the pieces are exposed to oxygen plasma (Plasma Etch, NV, USA) for 1 min. After removal from the chamber, the TPE piece is brought into contact with the glass, and left to cure in a 60°C oven for 5 min. To achieve pressure-driven liquid flow of the suspensions in these TPE-glass hybrid devices, tubing connectors (Nanoport, WA, USA) are attached to the ports on the chip using room temperature cured epoxy.

3.2.2 Cyanobacteria Source and Cultivation

Cyanobacterium *Synechocystis* sp. PCC 6803 was grown in liquid BG-11 medium [25]. The strain was inoculated at an initial concentration of 10^6 mL^{-1} and cultured in a 250 mL Erlenmeyer flask with 50 mL culture medium in an INNOVA 44 Incubator Shaker (New Brunswick Scientific, NJ, USA) at 30°C and a speed of 225 rpm, and an average light intensity was 100±9 $\mu mol \cdot m^{-2} \cdot s^{-1}$. These 50 mL suspensions were cultured to a concentration between 2×10^8 and 5×10^8 mL^{-1} for future use, at which time the culture was diluted or concentrated to the desired cell density for the inertial focusing tests.

3.2.3 Experimental setup and method

The inlet of the device was connected to one syringe using Tygon tubing. The cyanobacteria culture in a syringe with known concentration (2.4×10^7 mL^{-1}; 2.4×10^8 mL^{-1} or 2.4×10^9 mL^{-1}) was delivered into the inertial focusing microfluidic chip at specified flow rates using a syringe pump (New Era Pump Systems, NY, USA) to generate stable and continuous volumetric flow. The inlet concentration of the cyanobacteria suspension was measured with a hemocytometer (Hausser Scientific Partnership, PA, USA) three times.

3.2.4 High-speed Imaging and data analysis

The TPE-glass hybrid device was mounted onto the stage of an Olympus IX 71 Inverted optical Microscope (Olympus, Japan), and connected to a high-speed camera (Fastcam SA3, Photron, USA). Using the high-speed camera the cyanobacteria concentration process in the isolation region of the chip was recorded at 2,000 frames per second (495 µs interval) with a 5 µs shutter speed. After images were acquired and stored, analysis conducted using ImageJ (http://rsb.info.nih.gov/ij/) counted the number of cyanobacteria in each frame and recorded the horizontal *xy* location of each cell. Performance of this chip for cyanobacteria harvesting was assessed using the measured recovery efficiency and concentration factor.

3.3 Theory

The concept of inertial migration has been introduced in this discussion to provide a qualitative background for the physics of system operation, and to indicate how modifications may be made to existing design to facilitate focusing of micron-sized cyanobacteria. The first studies of inertial migration involved macro-scale systems in the laminar flow regime, and were demonstrated by Segré and Silberberg [26] in 1961. Their experiments in tubes of circular cross section showed that rigid, 1 mm diameter spherical particles migrated to an annular region located approximately six-tenths of the distance from the axis to the wall in a 1 cm diameter cylinder. Di Carlo *et al*. first carried out studies to accomplish inertial focusing of smaller particles in a microfluidics format under laminar flow conditions [27]. Those results demonstrated the potential for concentrating micron-sized particles/bio-particles in a microfluidic chip without externally applied forces or fields.

In a two-dimensional pipe flow such as that shown as shown in Fig. 1A, particles in laminar flow experience a force resulting from gradients in the parabolic velocity profile, which is called the shear gradient lift force (F_{SL}), pushing particles away from channel centerline. At the same time, the channel wall induces a surface-effect lift force (F_{WL}), which moves particles away from the channel or tube wall [20]. The net force is referred to as the lift force. When these two forces balance one another the particles are located in a stable equilibrium position within the cross section of the microchannel. This net lift force may be written as [28]:

$$F_L = \frac{\rho U_m^2 a^4}{D_h^2} f_c \quad (1)$$

where ρ is the liquid density, U_m is the maximum channel velocity, a is the particle diameter, f_c is a lift coefficient, and D_h is the hydraulic diameter of the channel, defined as $D_h = 2hw/(h + w)$, where h and w are the height and width of the channel cross-section, respectively. This equation illustrates the strong dependence of lift force on particle diameter, specifically, to the fourth order. Because of this dependence on a, to focus smaller particles in a given geometry, much higher U_m and a reduced microchannel cross-sectional area are required compared to other devices for larger bio-particles, such as those used with mammalian cells. In straight, square channels (Fig. 1B), particles focus to four equilibrium regions centered on each face. In straight rectangular channels (Fig. 1C), particles migrate to two equilibrium positions, which are located at the middle of the long channel faces. For optimal separations in this study, even fewer equilibrium positions are needed in order to maximize the concentration factor of the product stream. To accomplish this reduction in the number equilibrium cell locations, inertial focusing is coupled with Dean flow, which may be generated through use of a curved channel (Fig. 1D) that results in a mismatch of the velocity magnitude in the downstream direction between the center and near-wall regions [20]. Dean drag (F_D) scales as $F_D \sim \rho U_m^2 a D_h^2/r$, where r is the radius of curvature of the channel.

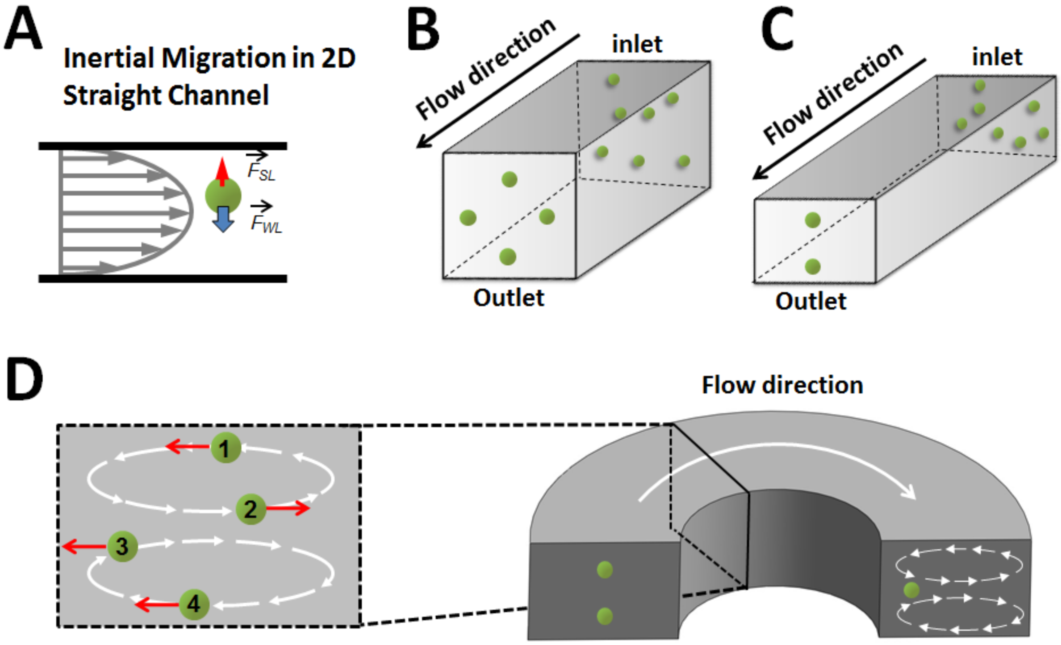

Figure 3.1 Inertial lift forces. (A) In two-dimensional or axisymmetric geometries, particles in flow experience opposing forces associated with shear gradient lift (F_{SL}) and wall-effect lift (F_{WL}) that balance when the particles reach equilibrium lateral positions. (B) In a square channel, the randomly distributed inlet suspension will be focused into four equilibrium regions centered at each face. (C) For rectangular channels, the randomly distributed particles migrate to two equilibrium positions which are located near the middle of the long channel faces. (D) Dean flow creates two counter-rotating vortices (white arrows) perpendicular to the primary flow direction; red arrows show the overall effects of both lift force and Dean drag (location 1: lift force – Dean drag; location 2: lift force + Dean force; location 3: only Dean force; location 4: only Dean force).

3.4 Results and Discussion

3.4.1 Design of the inertial focusing device for cyanobacteria harvesting

As mentioned above there are a number of challenges when concentrating small particles such as cyanobacteria using an inertial migration approach. First, because cyanobacteria (2 µm) are small relative to mammalian cells (≥ 10 µm), a reduced microchannel cross-section is required because of the non-linear dependence on cell size, which complicates the design and fabrication of correspondingly small microchannel dimensions. Another important challenge is the high pressure drop required to achieve flow rates (as represented by U_m) necessary to focus cyanobacteria under conditions that may be scaled up for commercial use. In particular, these pressure drops become problematic when standard materials are used to fabricate the microfluidic networks. An example of such a material is Poly(dimethylsiloxane) (PDMS), which is a relatively soft elastomer used in many microfluidic chip applications. In that device, however, that material exhibits large deformation of the microchannel cross-section when flow rates are increased to enhance particle focusing, with the result that the particles are actually de-focused. Consequently, fabrication procedures for this device have been modified to allow use of standard lithographic techniques with a different polymeric material, thermoset polyester (TPE), which is a polymer alternative to PDMS with similar fabrication procedures but higher rigidity for high-pressure flow applications. TPE resin is a readily acquired, inexpensive feedstock, currently costing $84.25 per gallon (TAP Plastics Inc., CA, USA) As a reference point, a single chip in these studies requires only 1 mL of the TPE resin. Thus, the research cost of raw materials is $0.02 per chip of 10 parallel channels, and bulk use of material for large-scale parallelized designs can be expected to further lower the cost. Importantly, it is anticipated that the use of this rigid polymer will serve as an intermediary for the smooth transition from laboratory devices to other thermoplastics more ideally suited for commercial use [29].

The use of serpentine channels provides an efficient geometry for inertial focusing, and it has been demonstrated that less linear distance is required as compared to straight channels, plus the fact that the serpentine geometry is readily parallelized for scale up to high throughput operation. The microchannel design, which is optimized for cyanobacteria harvesting, is shown in Fig. 2A. There are five functional components: an inlet for the homogeneous suspension, a filter region to prevent downstream channel clogging, an asymmetric serpentine channel to focus the particles, an isolation region to separate the particle stream from liquid media, and three collection outlets. The microchannel height is a uniform 10 µm, which was necessary to focus particles as small as cyanobacteria. The curved channels have a width of 20 µm on the small radius turns and a width of 80 µm on the large radius turns. The entire serpentine region is 4 mm in extent. The width of the isolation region is 150 µm, and there are outlet three branches connected to that region. From top to bottom in Fig. 2C, the branch widths are 30 µm, 45µm and 75 µm. Based on this isolation region and outlet channel configuration, the maximum possible concentration factor is 3.33. Using three-dimensional computational fluid dynamics simulations, it was predicted that outlet 2 should contain the product stream, and outlets 1 and 3 would, ideally, collect particle-free waste streams. Video from the high-speed camera showing the cyanobacteria concentration process in the isolation region is shown in a SI Video (see supplementary information Video). The camera captured images at 2000 fps, and this rate is adjusted to 100 fps in video 1 to facilitate viewing.

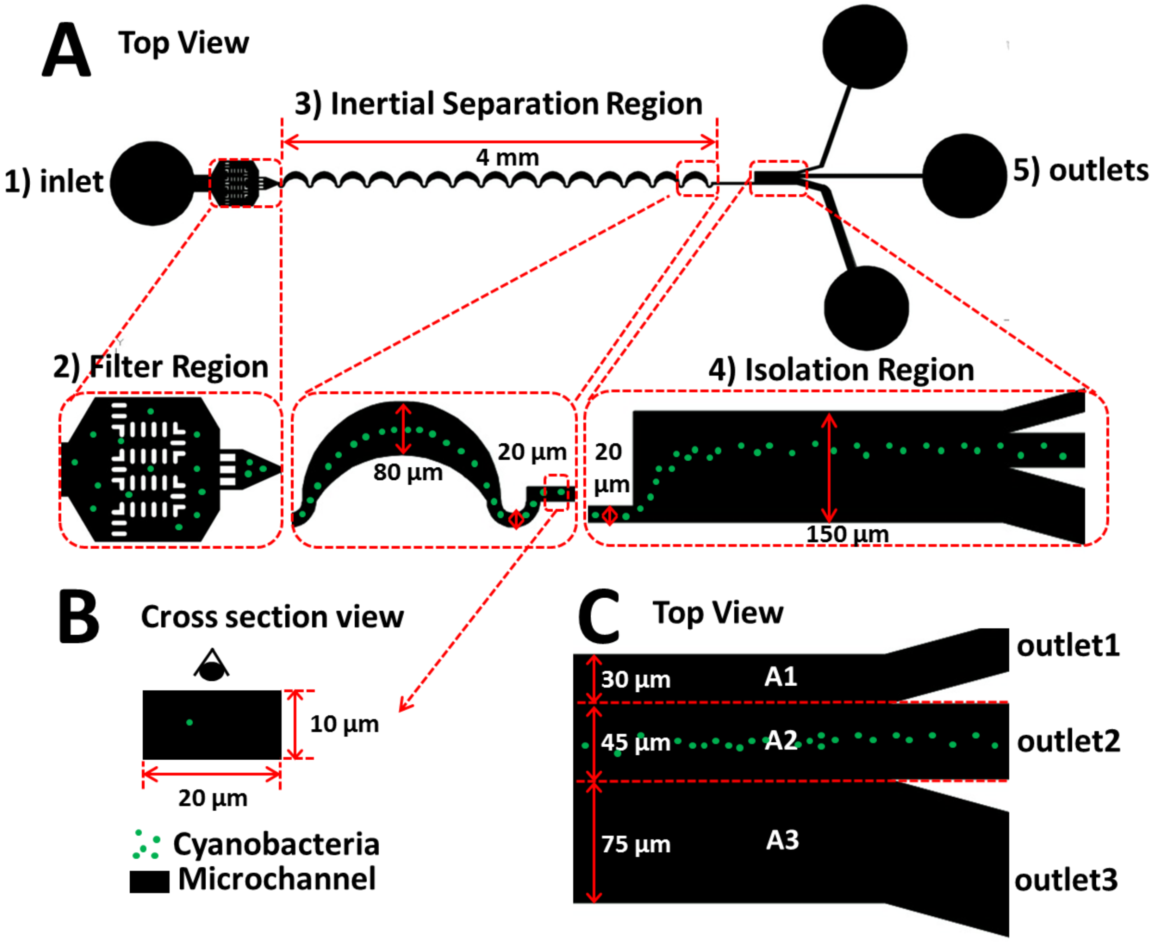

Figure 3.2 Design of the microfluidic device for concentrating cyanobacteria. (A) Top view of the design and enlarged images for each region. There are five functional components: an inlet for the homogeneous suspension, a filter region to prevent downstream channel clogging, an asymmetric serpentine channel to focus the particles, an isolation region to separate the particle stream from liquid media, and three collection outlets. Green dots represent cyanobacteria pathlines. (B) Cross section view of cyanobacteria focusing in the straight channel after the last curve. (C) Detailed view and scale of the isolation region. The A1 and A3 regions fed outlets 1 and 3, which carried the waste streams, and A2 fed outlet 2, which was intended for collecting the concentrated cyanobacteria product stream.

3.4.2 Effect of flow rate on cyanobacteria distribution

Fig. 3 shows the histogram (left) and heat map (right) of cyanobacteria distribution across the isolation part of the microchannel (150 µm) for an inlet concentration of 0.1 vol-% (2.4×10^{8} mL^{-1}), for flow rates between 100 µL/min and 700 µL/min. The distribution of lateral cyanobacteria cell positions can be depicted using a histogram plot as well as a heat map. Each cell's horizontal (*x*,*y*) position was measured from a single image stack, and then all positions from all 2000 image stacks were plotted onto a single histogram and heat map. The histogram allows for the visualization of the cyanobacteria distribution across the microchannel relative to the locations of the three outlets. Fitted Gaussian curves, which are used to quantify the width of the distribution, are shown as red dotted lines for all histograms. At the same time, the heat map enables qualitative visualization of cyanobacteria locations in the isolation region of the microchannel as shown in Fig. 3B. Flow rate played a critical role in the distribution of cyanobacteria across the 150 µm microchannel width. Cyanobacteria distribution histograms show increasing focusing efficiency at higher flow rates, that is, the width of the fitted Gaussian profiles become narrower. As flow rate, and thus velocity increase, inertial forces increase in magnitude relative to viscous forces, with the result that the shear gradient lift force and wall-effect lift force both increase and confine the particle stream to a narrower region. This effect may be quantified using the Reynolds number, which is a dimensionless parameter that indicates the significance of inertial forces with respect to viscous forces [20]. It is desirable to achieve as high degree of focusing (as narrow a distribution) as possible, because that condition will result in the highest possible recovery efficiency and concentration factor. Here, recovery efficiency is defined as the ratio of the number of cyanobacteria in the product channel to the total number of cyanobacteria. The concentration factor is defined as the ratio of output cyanobacteria concentration to input cyanobacteria concentration. Recovery efficiency and concentration factor are important indices used to evaluate the performance of the algal harvesting platform.

The horizontal location of the profile peak also depends on the volumetric flow rates, such that it shifts further away from the centerline toward the side wall as flow rate is increased.

The reason for the shift is that, at higher flow rates, the increase in the shear gradient lift force (F_{SL}) becomes dominant, and pushes the cyanobacteria nearer to the side wall [20]. At the same time, the Dean drag force acting on the particles is proportional to the square of the maximum velocity in the curved channel region, with the result that the cyanobacteria experience a stronger Dean drag directing them toward the inner wall as flow rate (or Reynolds number, Re) is increased [30]. These two effects result in the observed shift in the location of the peak cyanobacteria distribution toward the side wall at higher flow rates (Re). Knowledge of the location of the focused cyanobacteria stream is a key factor in the design of the microfluidic concentrator isolation region and the geometry of the outlet channels.

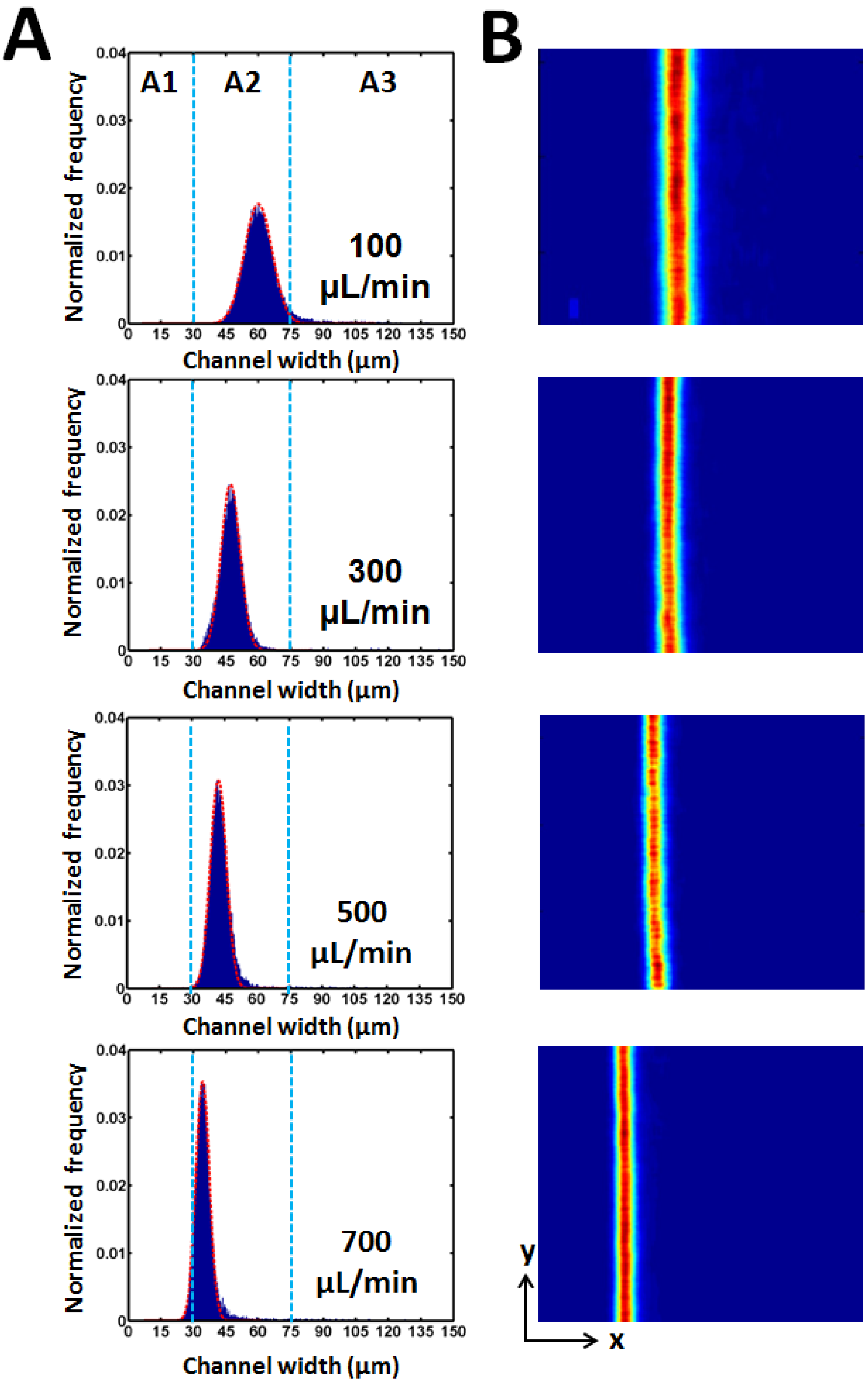

Figure 3.3 Cyanobacteria distribution across the isolation region at different flow rates, for an 0.1 vol-% inlet concentration. (A) The histogram shows the distribution of cyanobacteria in regions A1, A2, and A3, where fitted Gaussian curves are shown as red dotted lines for all histograms. (B) Heat map for the corresponding histogram on the left.

3.4.3 Effect of input concentration on cyanobacteria distribution

To use this platform to concentrate the cyanobacteria culture from its initial dilute state to a suspension with a hundred- to thousand-fold increase in cell density, it is necessary for the microchannel configuration to successfully focus a wide range of suspension concentrations. The inertial focusing approach has been demonstrated when suspension concentrations are low (< 0.01 vol-%) [27], but device performance at higher cells concentrations has yet to be quantified. In this study a wide range of cyanobacteria culture concentrations—0.01 vol-%, 0.1 vol-% and 1 vol-%—have been investigated using this microfluidic concentrator platform. As expected, the degree to which the cell suspension was focused depended on the initial concentration. In the studies, a high-speed camera recorded the cyanobacteria distributions across the width of the isolation region for different cyanobacteria suspension concentrations. In those experiments the flow rate was held constant at 300 μL /min. A video of this process with a 0.1 vol-% cyanobacteria suspension inlet concentration is shown in the SI Video (see the supplementary information Video). Fig. 4 shows the histogram (left) and heat map (right) of the cyanobacteria distributions across the channel width. As the concentration increased from 0.01 vol-% (2.4×10^{7} mL^{-1}) to 1 vol-% (2.4×10^{9} mL^{-1}), the locations of the maximum cell densities were similar, approximately 48 μm (48.8 μm for 0.01 vol-%, 47.4 μm for 0.1 vol-%, 48.3 μm for 1 vol-%), which confirms the theoretical result that, for given particle size and channel geometry, the flow rate (or, *Re*) determines the location of the profile peak. As concentration increases from 0.01 to 1 vol-%, the FWHM (full width at half maximum) of the cyanobacteria cell distribution increases from 7.79 μm to 19.9 μm, where the FWHM was calculated from a fitted Gaussian distribution to the cyanobacteria distribution histogram. All cyanobacteria profile widths are greater than 3 times the cell diameter (2 μm), and this spread is due to the decrease in velocity from the focusing region to the expanded isolation region; there is a measurable defocusing effect that occurs which impacts achievable concentration factors. On top of this phenomenon, the streak widths reflect a concentration dependence, which may be explained as follows: first, the number of cyanobacteria per unit length of the channels is fixed, based on the initial concentration; at lower concentrations it is theoretically possible for all cells to be focused onto a single pathline, but at the highest concentration, 1 vol-%, this is no longer the case [31]. Second, at higher concentrations there is increased inter-particle interactions, which tend to be repulsive due to surface charge effects [20]. Although the salt in the media mitigates surface charge effects, the close proximity of the cells upon focusing also tends to defocus the particle trains. Thus, it is necessary not only to know the location of the focused particle streams, but also to take into account the streak broadening in order to ensure as a high recovery efficiency as possible. The isolation region design used in this study works well for cyanobacteria suspensions with inlet concentrations up to 1 to 2 vol-%.

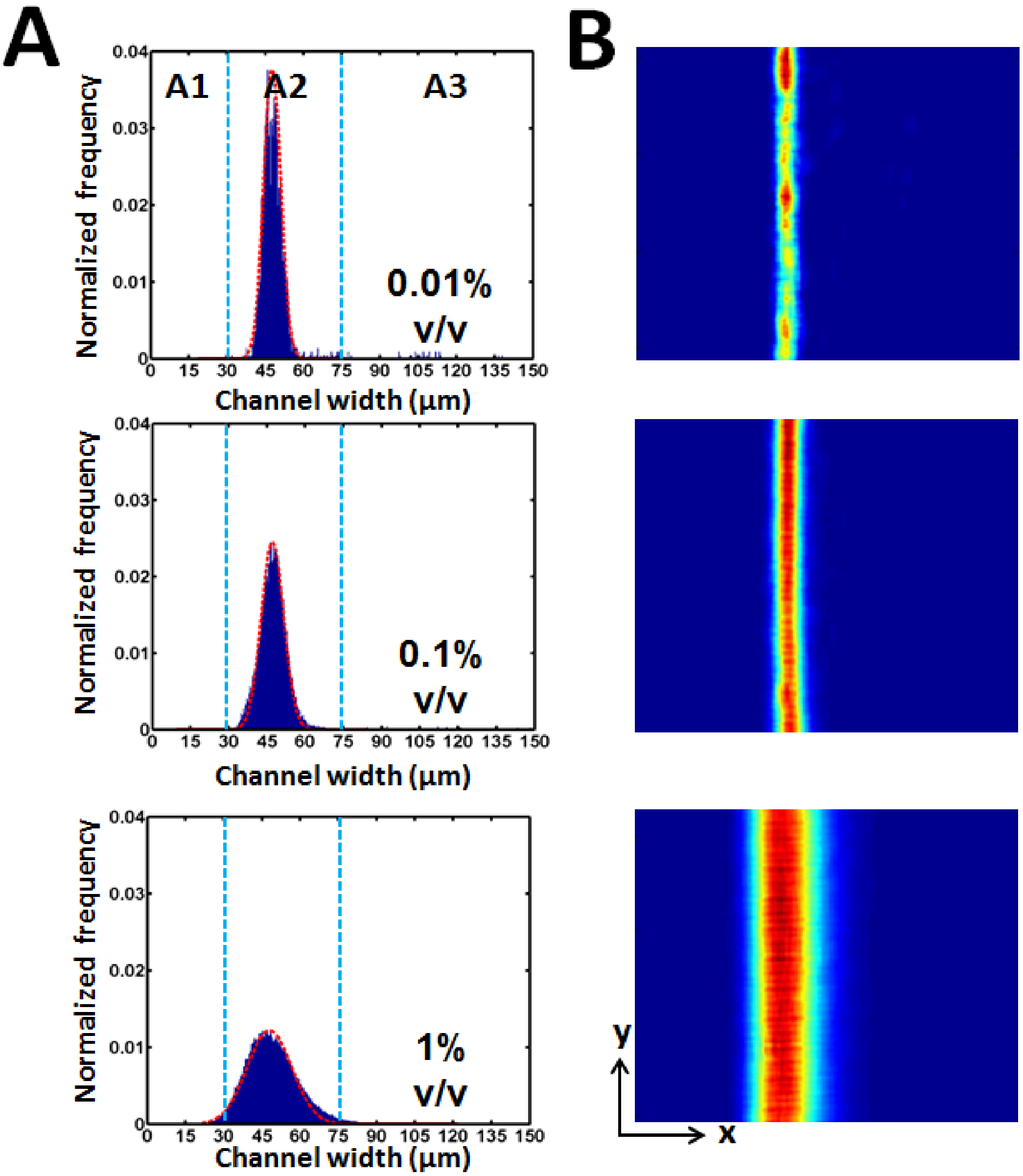

Figure 3.4 Cyanobacteria distribution across the isolation region for different inlet cyanobacteria suspension concentrations, at a flow rate of 300 μL/min. (A) The histogram shows the distribution of cyanobacteria in A1, A2 and A3 regions, and fitted Gaussian curves are shown as red dotted lines for all histograms. (B) Heat map for the corresponding histogram on the left.

3.4.4 Effect of flow rate on concentration effectiveness

To quantify the ability of this inertial migration based microfluidics platform to concentrate cyanobacteria, the effect of flow rate on cyanobacteria recovery efficiency and concentration factor were investigated, and the results are shown in Fig. 5 for a 0.1 vol-% inlet suspension concentration. Flow rates had a positive influence on cyanobacteria harvesting, specifically, recovery efficiencies increased as the flow rate was increased up to 500 µL/min, with a decrease in efficiency at 700 µL/min. All of the recovery efficiencies were above 96.3±0.3% (mean ± standard deviation), with the highest at 98.4±0.2%. Concentration factor was found to follow the same trend as a function of flow rate. Based on outlet channel geometries, the maximum possible concentration factor for the current design is 3.33, and the experimental results yielded concentration factors above 3.2 for all the flow rates that were tested. The decrease in both recovery efficiency and concentration factor at the highest flow rate, 700 µL/min, can be explained by the distribution of the cyanobacteria across the microchannel. It was observed that, although the width of cyanobacteria streak is narrower at 700 µL/min than at the lower flow rates, its location shifts toward the side wall. As a result, some cells were directed into outlet 1 instead of outlet 2. If the outlet channel geometries were redesigned to take this shift into account, higher recovery efficiencies and concentration factors would be achieved.

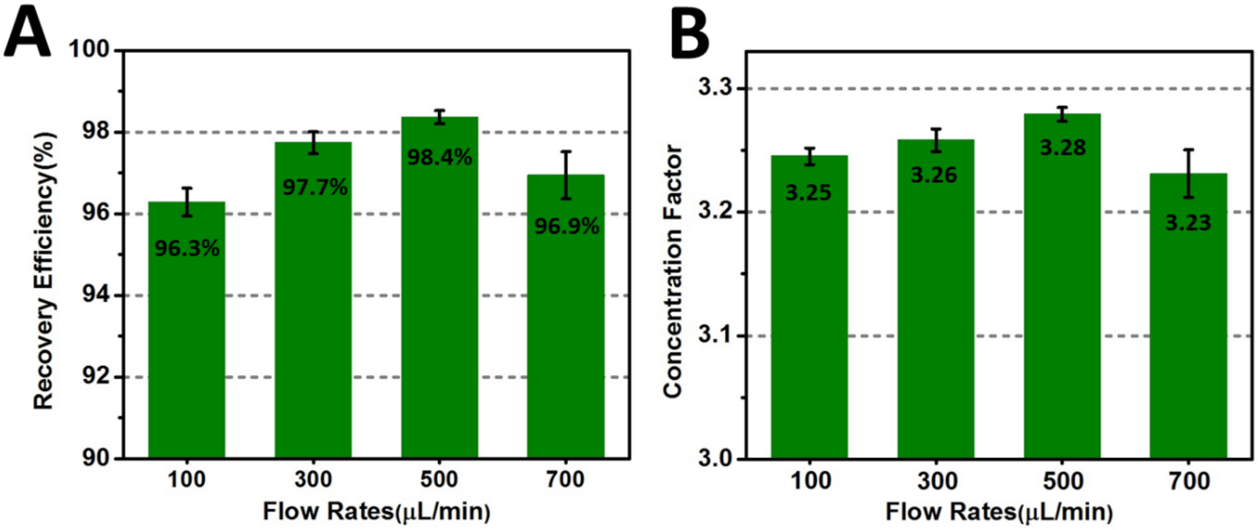

Figure 3.5 Effect of flow rate on chip concentration performance of Cyanobacterium *Synechocystis* sp. PCC 6803. (A) Effect of flow rates on recovery efficiency. (B) Effect of flow rates on concentration factor. Cyanobacteria concentration: 0.1 vol-% (2.4×10^{8} cells/ mL).

3.4.5 Effect of inlet cell density on concentration effectiveness

The Cyanobacteria inlet suspension concentration is also a key factor in the harvesting process. If the current single channel design were operated in series, such that the inlet concentration is the outlet product concentration from the previous stage, then there is a monotonic increase in suspension density with each pass or stage. In this manner an initially dilute suspension can be concentrated 120-fold after four stages. To ensure successful operation over a wide range of cell densities, the platform was tested with different inlet concentrations ranging from 0.01 vol-% (2.4×10^7 mL^{-1}) to 1 vol-% (2.4×10^9 mL^{-1}) to quantify its performance. As opposed to flow rate, the suspension density had a slightly negative effect on harvesting efficiency, as shown in Fig. 6. The recovery efficiency and concentration factor both dropped slightly as concentration increased two orders of magnitude. The average drop in recovery efficiency was 2.2%, and at the same time, the average reduction in concentration factor was 0.073, or 2.4%. These performance metrics demonstrate that there is very small degradation in performance for a wide range of suspension concentrations, and the basic device design is suitable for implementation in a series format to obtain a concentrated suspension in a multi-pass configuration. Note that concentrations below 0.01 vol-% were not investigated, because it is known that device operation only improves at lower concentrations [20]. The current device is relevant as a first stage dewatering technology, since it can process large volumes if thousands to tens of thousands of microchannels operate in parallel, and it can achieve overall concentration factors greater than 100 if operated in series. Also, work continues on the addition of functional structures into this device to significantly increase the throughput and the concentration factor in single channel.

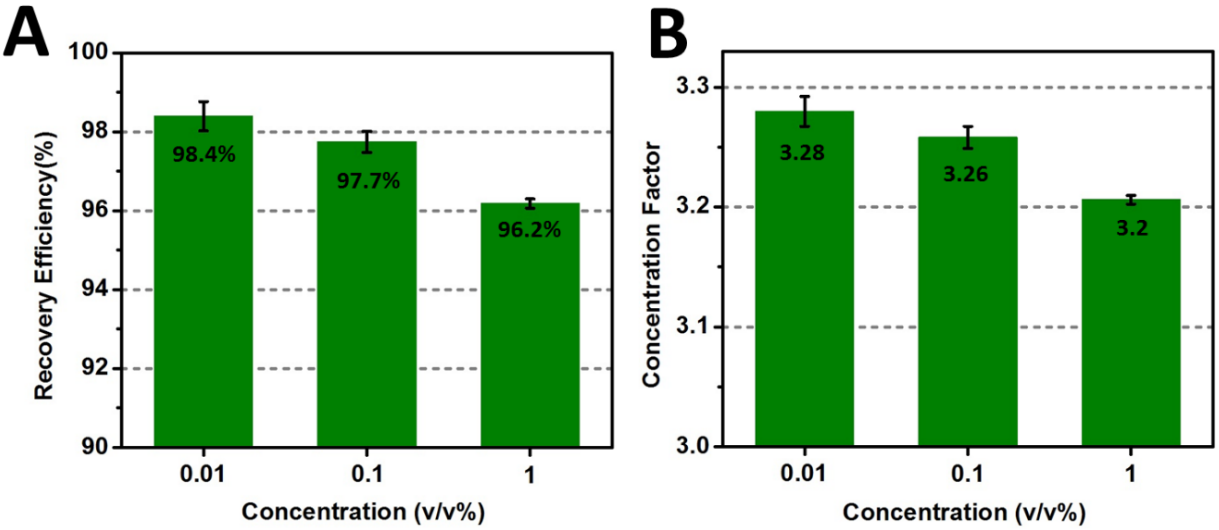

Fig 3.6 Effect of inlet suspension concentrations on chip performance at 300 µL/min for Cyanobacterium *Synechocystis* sp. PCC 6803. (A) Effect of inlet concentration on recovery efficiency. (B) Effect of inlet concentrationss on the concentration factor.

3.4.6 Power consumption

One essential component of the biofuel processing stream is power consumption, and this aspect has been a major roadblock on the path toward economic viability. The results presented above conclusively demonstrate that the inertial focusing based microfluidic concentrator (µFC) is capable of continuous operation for harvesting cyanobacteria with a high recovery efficiency. As a complement to those studies, power consumption calculations have been carried out to quantify the energy required per unit volume of suspension in order to determine whether the energy consumption is comparable to reported data for other harvesting technologies. In practice, the major consumption of power in this microfluidics platform comes from the fluidic pressure drop in each microchannel. The pressure drop down the length of a channel may be computed as [32]

$$Q_f = \frac{-\Delta p}{\kappa} \qquad (2)$$

where Q_f is the volumetric flow rate, K is the hydraulic resistance to flow within the microchannel, and Δp is the pressure drop in each microchannel. The resistance K can be calculated as [32]

$$K = \frac{12\mu L}{w^3 h}\left[1 - \frac{192\, w}{\pi^5 h}\sum_{n=1,3,5,..}^{\infty}\frac{1}{n^5}\tanh\left(\frac{n\pi h}{2w}\right)\right]^{-1} \tag{3}$$

The power consumption, or shaft work (*W*) can then be determined as

$$W = \Delta p \times Q_f \tag{4}$$

From Eq. (4) it may be seen that the energy required per unit volume, or W/Q_f, is just equal to the pressure drop. With the advent and now ubiquitous use of soft lithography techniques, it is straightforward to construct multi-layer, massively parallel microfluidic networks. In a parallel microchannel system, the pressure drop of a single channel is equal to the overall pressure drop of the whole system. Therefore, there is an advantage to implement a parallel large-scale design to increase the throughput without compromising the low power consumption per unit sample volume. Of course, the power consumption per unit volume will increase, more or less linearly, in a serial system, where the number of sequential stages will determine the overall concentration factor to be achieved. The calculated pressure drop, power consumption, and energy consumed per unit volume as a function of serial stages (concentration factor) are shown in Table S1. Table 1 shows the calculated power consumption per unit volume for different concentration factors in the cyanobacteria microfluidic concentrator as well as for other technologies for which power consumption data are reported [33]. The single-microchannel flow rate used in Table 1 is 100 µL/min, which is an intermediate flow rate for purposes of demonstration; lower (10 µL/min) and higher (1000 µL/min) flow rates can also work in this system (data not shown). The calculated power consumption of the microfluidic concentrator is comparable to other reported centrifuge methods, with even lower energy consumption than a decanter bowl centrifuge at the same concentration factor. The energy consumption per unit volume of our microfluidics device with the current flow rate (100 µL/min) is comparable or even lower than conventional methods. But this is still not optimal based on the challenging target of being less than \$0.013/GGE (GGE: U.S. gallon of gasoline equivalent), as set by the National Alliance for Advanced Biofuels and Bioproducts (NAABB) in 2009. Every kWh/m^3 consumed at the first stage of harvesting contributes approximately \$1/GGE to the cost of algal biofuel [1]. This NAABB target necessitates reducing the energy requirements of the microfluidics approach by at least a factor of 10 relative to the Table 1 values. A ten-fold decrease in power requirements can be realized if the flow rate is reduced to 10 µL/min, which would be significantly lower than other reported power consumption per unit volume and approaching the algae harvesting energy consumption targets set by NAABB. Based on these simple power consumption analyses, it may be concluded that the microfluidic concentrator approach is a promising alternative for harvesting cyanobacteria for biofuel production.

3.4.7 Capital cost

The cost of fabricating a module capable of processing 300 L/h of cyanobacteria suspension to obtain a concentration factor of about 120 is considered here. Regarding the physical size, to process 300 L/h at 100 µL/min/channel, it would require 50000 parallel channels. Given the channel geometries used here, a 50-layer device with 1000 parallel microchannels per layer would have a width of 0.5 m, a height of 0.1 m, and length (in the direction of flow) of 0.01 m. That length represents a single pass through the concentrator, so sequential processing would require a module length of 0.01N, where N is the number of passes or concentration steps. If this device is constructed using thermoset polyester, as was done in this proof-of-concept study, the total cost of materials (retail) would be \$120, including the silicon wafer mold, photoresist, and monomer. A pump capable of processing this volumetric flow rate could be purchased for less than \$500. If we assume that the microfluidic module to be replaced 4 times a year due to fouling or mechanical failure, then the capital cost of the proposed system would be \$0.40/(m^3/day). This capital cost is less than one tenth of the settling pond, which has the lowest base costs of traditional harvesting approaches discussed in the introduction section. It must also be noted that there is a trade-off between the capital cost and the energy consumption for the microfluidic concentrator. As the proposed scale-up strategy is linear, capital costs would increase linearly with decreasing flow rate. For example, the capital cost would be \$4.0/(m^3/day) to process 300 L/h at 10 µL/min/channel, but the energy (pumping) costs would decrease by a factor of 10.

Table 3.1 Power consumptions of microfluidic concentrator and other concentrating approaches

Harvesting technology	Concentration factor (vol. in/vol. out)	Energy consumed per unit volume ($kWh \cdot m^{-3}$)
Decanter bowl centrifuge [33]	11	8.0
Self-cleaning, disc-stack centrifuge [33]	120	1.0
Nozzle discharge centrifuge [33]	20-150	0.9
Microfluidic Concentrator	3	1.6
	11	3.2
	36	4.8
	118	6.4
	390	8.1

Table 3.2 The calculated pressure drop, power consumption and energy consumed per volume unit based on increased concentration factor.

Concentration factor (cells out/cells in)	Pressure drop ($N\cdot m^{-2}$)	Power consumption (W)	Energy consumed per volume unit ($kWh\cdot m^{-3}$)
3	5.83×10^{6}	485.9	1.6
11	1.17×10^{7}	971.7	3.2
36	1.75×10^{7}	1457.6	4.8
118	2.33×10^{7}	1943.5	6.4
390	2.92×10^{7}	2429.4	8.1

3.5 Conclusion

A low cost, miniaturized microfluidic concentrator for cyanobacteria harvesting has been developed. The platform design is based on concepts from inertial migration and Dean flow theories, and it has the potential to be applied at commercial scales for harvesting of cyanobacteria at initial concentrations of 0.1, 0.01, or even 0.001 vol-%, with a final product stream that may have cell densities as high as 3.2 vol-%. Demonstrated recovery efficiencies in this device exceed 96%, and can reach 98% under continuous operating conditions, while at the same time resulting on concentration factors approaching the theoretical maximum. This device is versatile, and it has been shown that higher recovery efficiencies and concentration factors may be achieved at higher flow rates and with optimized outlet channel geometries. Importantly, this device is tailored to Cyanobacteria concentration, but is by no means restricted to this microorganism. Many other microalgae or bacteria could be concentrated by adjusting the microchannel geometries. Compared with the capital cost of other microalgae/cyanobacteria harvesting technologies, the cost of device is very low (~$0.002 per channel), there are no residual chemicals in the harvested cyanobacteria or media, and there are no moving parts in the device itself. In addition, volumetric power consumption of this microfluidic concentrator is comparable and even lower relative to other traditional approaches. Scale up of this microfluidics concentrator is conceptually straight forward through parallel microchannel configurations and multilayer (stacking) operation. Additional opportunities to lower the microalgae harvesting costs using microfluidics technology lies in the trade-off in the inverse relationship between operating energy requirements and capital cost. Further studies using lower flow rates in the microfluidics device would be beneficial in reducing the overall cost and approaching the NAABB target. This microfluidic concentrator is a promising alternative approach for harvesting at commercial scale, and may help with overall process economics and feasibility.

REFERENCES

[1] J. E. Coons, D. M. Kalb, T. Dale, and B. L. Marrone, “Getting to low-cost algal biofuels: A monograph on conventional and cutting-edge harvesting and extraction technologies,” *Algal Res.*, vol. 6, no. PB, pp. 250–270, 2014.

[2] A. Kumar, S. Ergas, X. Yuan, A. Sahu, Q. Zhang, J. Dewulf, F. X. Malcata, and H. van Langenhove, “Enhanced CO2 fixation and biofuel production via microalgae: Recent developments and future directions,” *Trends Biotechnol.*, vol. 28, no. 7, pp. 371–380, 2010.

[3] D. Kumar, L. K. Pandey, and J. P. Gaur, “Metal sorption by algal biomass: From batch to continuous system,” *Algal Res.*, vol. 18, pp. 95–109, 2016.

[4] C. Durall and P. Lindblad, “Mechanisms of carbon fixation and engineering for increased carbon fixation in cyanobacteria,” *Algal Res.*, vol. 11, pp. 263–270, 2015.

[5] C. Banerjee, K. K. Dubey, and P. Shukla, “Metabolic engineering of microalgal based biofuel production: Prospects and challenges,” *Front. Microbiol.*, vol. 7, no. MAR, 2016.

[6] A. I. Barros, A. L. Gonçalves, M. Simões, and J. C. M. Pires, “Harvesting techniques applied to microalgae: A review,” *Renew. Sustain. Energy Rev.*, vol. 41, pp. 1489–1500, 2015.

[7] S. K. Wang, A. R. Stiles, C. Guo, and C. Z. Liu, “Harvesting microalgae by magnetic separation: A review,” *Algal Res.*, vol. 9, pp. 178–185, 2015.

[8] W. Mo, L. Soh, J. R. Werber, M. Elimelech, and J. B. Zimmerman, “Application of membrane dewatering for algal biofuel,” *Algal Res.*, vol. 11, pp. 1–12, 2015.

[9] M. E. Hums, R. A. Cairncross, and S. Spatari, “Life-Cycle Assessment of Biodiesel Produced from Grease Trap Waste,” *Environ. Sci. Technol.*, vol. 50, no. 5, pp. 2718–2726, 2016.

[10] P. T. Pienkos and A. Darzins, “The promise and challenges of microalgal-derived biofuels,” *Biofuels, Bioprod. Biorefining*, vol. 3, no. 4, pp. 431–440, Jul. 2009.

[11] R. Davis, J. Markham, C. Kinchin, N. Grundl, E. C. D. Tan, D. Humbird, R. Davis, J. Markham, C. Kinchin, N. Grundl, E. C. D. Tan, and D. Humbird, “Process Design and Economics for the Production of Algal Biomass : Algal Biomass Production in Open Pond Systems and Processing Through Dewatering for Downstream Conversion Process Design and Economics for the Production of Algal Biomass : Algal Biomass P,” no. February, 2016.

[12] D. Mark, S. Haeberle, G. Roth, F. von Stetten, and R. Zengerle, “Microfluidic lab-on-a-chip platforms: requirements, characteristics and applications.,” *Chem. Soc. Rev.*, vol. 39,

no. 3, pp. 1153–82, 2010.

[13] L. Xu, I. L. Brito, E. J. Alm, and P. C. Blainey, “Virtual microfluidics for digital quantification and single-cell sequencing,” *Nat. Methods*, vol. 13, no. 9, pp. 759–762, 2016.

[14] C. Haynl, E. Hofmann, K. Pawar, S. Förster, and T. Scheibel, “Microfluidics-Produced Collagen Fibers Show Extraordinary Mechanical Properties,” *Nano Lett.*, p. acs.nanolett.6b02828, 2016.

[15] T. J. Levario, B. Lim, S. Y. Shvartsman, and H. Lu, “Microfluidics for High-Throughput Quantitative Studies of Early Development,” no. February, pp. 285–309, 2016.

[16] B. L. Wang, A. Ghaderi, H. Zhou, J. Agresti, D. A. Weitz, G. R. Fink, and G. Stephanopoulos, “Microfluidic high-throughput culturing of single cells for selection based on extracellular metabolite production or consumption,” *Nat Biotech*, vol. 32, no. 5, pp. 473–478, 2014.

[17] S. C. Hur, H. T. K. Tse, and D. Di Carlo, “Sheathless inertial cell ordering for extreme throughput flow cytometry.,” *Lab Chip*, vol. 10, no. 3, pp. 274–280, 2010.

[18] J. Lim, O. Caen, J. Vrignon, M. Konrad, V. Taly, and J. C. Baret, “Parallelized ultra-high throughput microfluidic emulsifier for multiplex kinetic assays,” *Biomicrofluidics*, vol. 9, no. 3, 2015.

[19] D. Di Carlo, J. F. Edd, D. Irimia, R. G. Tompkins, and M. Toner, “Equilibrium separation and filtration of particles using differential inertial focusing,” *Anal. Chem.*, vol. 80, no. 6, pp. 2204–2211, 2008.

[20] D. Di Carlo, “Inertial microfluidics.,” *Lab Chip*, vol. 9, no. 21, pp. 3038–3046, 2009.

[21] H. Amini, W. Lee, and D. Di Carlo, “Inertial microfluidic physics,” *Lab Chip*, vol. 14, no. 15, pp. 2739–2761, 2014.

[22] J. M. Martel and M. Toner, “Inertial focusing in microfluidics.,” *Annu. Rev. Biomed. Eng.*, vol. 16, pp. 371–96, 2014.

[23] J. M. Martel, K. C. Smith, M. Dlamini, K. Pletcher, J. Yang, M. Karabacak, D. a Haber, R. Kapur, and M. Toner, “Continuous Flow Microfluidic Bioparticle Concentrator.,” *Sci. Rep.*, vol. 5, p. 11300, 2015.

[24] L. Wang, W. Liu, Y. Wang, J. Wang, Q. Tu, R. Liu, and J. Wang, “Construction of oxygen and chemical concentration gradients in a single microfluidic device for studying tumor cell-drug interactions in a dynamic hypoxia microenvironment.,” *Lab Chip*, vol. 13, no. 4, pp. 695–705, 2013.

[25] Y. E. Cheah, S. C. Albers, and C. A. M. Peebles, “A novel counter-selection method for markerless genetic modification in Synechocystis sp. PCC 6803,” *Biotechnol. Prog.*, vol.

29, no. 1, pp. 23–30, 2013.

[26] G. Segré and A. Silberberg, “Radial Particle Displacements in Poiseuille Flow of Suspensions,” *Nature*, vol. 189, no. 4760, pp. 209–210, 1961.

[27] D. Di Carlo, D. Irimia, R. G. Tompkins, and M. Toner, “Continuous inertial focusing, ordering, and separation of particles in microchannels.,” *Proc. Natl. Acad. Sci. U. S. A.*, vol. 104, no. 48, pp. 18892–7, 2007.

[28] E. S. Asmolov, “The inertial lift on a spherical particle in a plane Poiseuille flow at large channel Reynolds number,” *J. Fluid Mech.*, vol. 381, pp. 63–87, 1999.

[29] E. Sollier, C. Murray, P. Maoddi, and D. Di Carlo, “Rapid prototyping polymers for microfluidic devices and high pressure injections,” *Lab Chip*, vol. 11, no. 22, p. 3752, 2011.

[30] J. Sun, M. Li, C. Liu, Y. Zhang, D. Liu, W. Liu, G. Hu, and X. Jiang, “Double spiral microchannel for label-free tumor cell separation and enrichment,” *Lab Chip*, vol. 12, no. 20, p. 3952, 2012.

[31] K. J. Humphry, P. M. Kulkarni, D. A. Weitz, J. F. Morris, and H. A. Stone, “Axial and lateral particle ordering in finite Reynolds number channel flows,” *Phys. Fluids*, vol. 22, no. 8, pp. 1–5, 2010.

[32] N. S. Lynn and D. S. Dandy, “Passive microfluidic pumping using coupled capillary/evaporation effects.,” *Lab Chip*, vol. 9, no. 23, pp. 3422–3429, 2009.

[33] E. Molina Grima, E. H. Belarbi, F. G. Acién Fernández, A. Robles Medina, and Y. Chisti, “Recovery of microalgal biomass and metabolites: Process options and economics,” *Biotechnol. Adv.*, vol. 20, no. 7–8, pp. 491–515, 2003.

CHAPTER 4: A SENSITIVE DNA CAPACITIVE BIOSENSOR USING INTERDIGITATED ELECTRODES[3]

4.1 Introduction

As universal biological information storage entities, nucleic acids (DNA and RNA) are unique biorecognition molecules, and the detection of pathogen genomic DNA or RNA provides one of the most reliable methods for viral infectious disease diagnostics. Emerging and remerging infectious pathogens, such as Ebola, Middle East Respiratory Syndrome (MERS), West Nile, dengue and Zika viruses create a strong need for a low-cost, point-of-care (POC) diagnostic platform that would enable rapid and sensitive pathogen detection[1–4]. Early and accurate detection of viral infectious diseases is of crucial importance in preventing epidemic disease outbreaks as well as in improving the efficacy of POC diagnostic technologies [5,6]. In use since the early 1990s, quantitative real-time polymerase chain reaction (qPCR) amplification has been a gold standard in viral diagnostics [7,8]. While qPCR offers high specificity with low limits of detection, it and other similar existing diagnostic methods have their drawbacks, such as the use of expensive devices for repeated thermal cycling, specialized non-reusable reagents, the need for sensitive fluorescence detection optics, and laborious assay preparation steps requiring trained personnel [9]. For example, a typical qPCR will require highly trained technicians 4 to 8 hours from sample preparation to completion using reagents such as specific TaqMan probes and

---

[3] This chapter is published in the following: Wang L, Veselinovic M, Yang L, Geiss BJ, Dandy DS, Chen T. A sensitive DNA capacitive biosensor using interdigitated electrodes. *Biosens Bioelectron*. 2017 Jan 15;87: 646-653. Lei Wang, MilenaVeselinovic and Lang Yang designed and performed experiments and analyzed data. Lei Wang, MilenaVeselinovic and Lang Yang wrote the manuscript, on which Brain Geiss, David Dandy and Tom Chen also assisted.

matching master mixes with reverse transcriptase enzymes and DNA polymerase, costing up to hundreds of dollars per assay depending on sample number and origin. Consequently, such analytical methods do not align with the need for a rapid, inexpensive, highly specific and sensitive point-of-care platform [5,6,10].

One of the cost-effective alternatives to PCR-based detection of pathogen genomic DNA relies on measurement of electrical property changes (resistance, capacitance, and complex impedance) due to DNA-DNA hybridization at probe-target binding sites without labeling. Such a sensing modality has been used successfully to detect specific DNA molecules in complex mixtures in a number of different assays, making it attractive for reliable classification of target DNA [11–14]. Electrode configuration and geometry can have a significant effect on sensor performance [15]. One of the widely used electrode configurations, especially for sensors measuring capacitance changes due to DNA-DNA hybridization (capacitive biosensors), is the interdigitated microelectrode. Microelectrodes are often made using modern photolithographic and deposition techniques on glass, silicon, or other solid substrates [15–17]. When they are tightly integrated with the back-end measurement circuits, they have significant advantages over conventional carbon-based electrodes [18] for analytical measurements, such as low resistance, high signal-to-noise ratio, rapid attainment of steady state, and the use of small solution volumes [19–21].

Operating modalities of biosensors using interdigitated electrodes (IDEs) can be non-faradaic [22] or faradaic [23]. The biosensor presented in this paper operates in the non-faradaic mode based on changes in capacitance between interdigitated electrodes to indicate molecular binding events at the electrode surface. Biosensors operating in the faradaic mode are often based on electrochemical impedance spectroscopy (EIS) [24,25] by measuring electron transfer resistance and double layer capacitance within a frequency range. Comparing to capacitive biosensors, biosensors based on EIS have been widely explored for their ability to capture complex resistance changes due to binding events at biosensor's electrode sites. However, they are more complex from an electronics and experimental protocol perspective, requiring a wide-range frequency sweep and the use of a potentially hazardous redox couple (e.g. Fe(CN)6 3-/4-) for measuring faradaic current. With the simplicity of measuring capacitance change between electrodes due to DNA-DNA hybridization between targets and probes, combined with low limit of detection (LOD) and high specificity, the results from this paper show that label-free capacitive biosensors have the potential as a baseline technology for low-cost, low-power, easy to use rapid detection POC platform [26].

To date, capacitive biosensors developed for DNA/RNA classification and pathogen detection have focused on improving the electrode surface modification process, achieving better transducer sensitivity, and increasing detection circuit sensitivity and signal-to-noise ratio (SNR). Berggren et al. [27] reported a label-free capacitive detection method for DNA detection, and pushed the limit of detection down to 25 complementary DNA targets per µL. Moreno-Hagelsieb et al. [28] demonstrated the use of an inexpensive Al/Al_2O_3 hybrid electrode to achieve good sensitivity. Guiducci et al. [29] elucidated a number of important details relevant to charge-based capacitance measurements, and provided insights into CMOS compatible implementation for integrated electronics. Stagni et al. [22] demonstrated a capacitive biosensor design with a detection range of 330 pF to 10 µF with good linearity. Lee et al. [30] developed CMOS circuitry based on charge/discharge theory for detecting capacitive signals to demonstrate its ability to detect 2 nM of target nucleic acid from H5N1 Influenza viruses. Qureshi et al. [31] achieved multiplexed detection using an interdigitated electrode array, with 25 pg/mL sensitivity to the complementary target. Eberhardt et al. [32] reported a bio-inspired artificial whisker to monitor fluid motion using capacitive sensing. Kallempud et al. [33] proposed a capacitance detection method using Fourier transform infrared spectroscopy (FT-IR) at high frequency, and achieved a 1ng/mL detection limit. Wright et al. [34] demonstrated an ultra-sensitive read-out circuit for measuring capacitance changes capable of sub-fF detection limit.

However, even with more than a decade of progress in capacitive biosensor development, significant challenges remain. A number of studies [31,35] reported poor sensor-to-sensor reproducibility. Non-uniformity of the self-assembled monolayer (SAM) and the covalently attached DNA probes on the sensor surface is a major contributing factor to poor sensor-to-sensor reproducibility. Sensor surface cleanliness greatly affects the uniformity of SAM layers [36]. Covalently attached ssDNA probes are largely affected by the presence of common contaminants in commercial thiolated DNA probes [30]. The lack of emphasis on electrode cleaning prior to assay functionalization may have also contributed to significant variations of the reported results. Stagni et al. [22] elucidated the importance of electrode surface cleaning in order to achieve uniform covalent binding of thiolated DNA probes. In addition, the total surface area of microelectrodes and the geometric relationship between two electrodes in a biosensor are other factors which directly affect sensor sensitivity and reproducibility, as measured capacitance output represents averaged values from all the fingers of the microelectrodes [37].

Here, a label-free, affinity-based capacitive IDE sensor is developed for unamplified nucleic acid detection, with high sensitivity and reproducibility. The proposed platform technology uses capacitance changes resulting from the solid-phase hybridization of nucleic acid targets with ssDNA probes immobilized on microelectrodes as the means of detection and identification. A 24-nucleotide DNA probe and target set was designed based on the West Nile virus sequence (Kunjin strain) and was applied as a model for nucleic acid based viral recognition and detection on the proposed capacitive biosensor [38,39]. The process of DNA probe preparation for the biosensor has been optimized to include steps to minimize the effect of contaminants associated with commercial thiolated DNA probes. It is demonstrated here that this new biosensor produces an output of more than 70nF in capacitance change in response to as few as 20 complementary DNA targets (0.25 attogram) at a concentration of ~1.5 aM. Due to the optimized cleaning process for the capacitive biosensor, including a pre-cleaning protocol, to improve covalent immobilization of purified single-stranded DNA probe oligomers onto the microelectrodes, the biosensor's reproducibility was improved compared to the reported results. In addition to the low detection limit, the biosensor showed a good dynamic range of detection from 1 μL^{-1} to 10^5 μL^{-1} target molecules (20 to 2 million total targets), making it suitable for sample analysis in a typical clinical application environment. The capacitance results obtained in this study were verified using fluorescently labeled oligonucleotides on a fluorescence scanner. Capacitive affinity-based assays have long been considered highly sensitive [40], but low specificity and reproducibility [27] hinder further improvement in their sensitivity. The results presented in this paper provide a potential path for practical use of capacitive sensing technology for viral pathogen detection in clinical settings.

4.2 Materials and Methods

4.2.1. DNA Oligonucleotides and Reagents

Validated HPLC purified DNA oligonucleotides were purchased from Integrated DNA Technologies (IDT, Inc., Coralville, IA). The sequences for single-strand DNA (ssDNA) oligonucleotides were based on the sequence of the West Nile Kunjin strain (Genbank Accession # AY274504) and were as follows:

DNA probe (Oligo 1):

5'-ThioMC6-D-TAGTATGCACTGGTGTCTATCCCT-3’

Complementary DNA target - 100% complementarity (Oligo 2):

5’-AGGGATAGACACCAGTGCATACTA-3’

Noncomplementary DNA target (Oligo 3):

5’-GCAATATAGATAACGCCAGATGGC-3’

Probe and target DNAs were resuspended in 1×TE-$MgSO_4$ buffer (TE stands for Tris-HCI and EDTA), which contained 100 µM magnesium sulphate ($MgSO_4$), 1 µM Tris-Hydrochloride (Tris-HCl) and 0.1 µM Ethylenediaminetetraacetic acid (EDTA), and were filtered through a 0.45 µm syringe filter (Millipore) prior to use. The 24-mer oligonucleotide DNA probe (Oligo1) was selected to form a stable duplex with its complementary target (Oligo 2) at room temperature, with minimal interference due to self-complementarity or secondary structure. The non-complementary target (Oligo 3) has 1 out of 24 base pairs complementary with oligo1 (4.16% complementarity).

For fluorescence detection, a second probe was generated that was 5'-thiolated (C6 propyl spacer) with a 3'-fluorescent Alexa Fluor 488 label (5'-ThioMC6-D/ TAGTATGCACTGGTGTCTATCCCT/AlexF488N/-3'), while complementary and non-complementary targets were 5'-labeled with fluorescent Alexa Fluor 594 dye (5'-Alex594N / AGGGATAGACACCAGTGCATACTA-3’ or 5’-Alex594N/GCAATATAGATAACGCCAGATGGC-3'). The 11-Mercapto-1-undecanol (MCU) (97%; Sigma-Aldrich, St. Louis, MO) was dissolved in water and filtered through a 0.45 µm syringe filter (Millipore) prior to use. Potassium hydroxide (KOH) and hydrogen peroxide (H_2O_2, 30% w/w in H_2O) (Sigma-Aldrich, St. Louis, MO) were used as received. Milli-Q water from Millipore (Billerica, MA) (18.2 MΩ·cm) was used in all experiments.

4.2.2 Gold Interdigitated Microelectrodes Sensor

Commercial gold coated IDE sensors were purchased from DropSens (Asturias, Spain). Each IDE has a finger width and spacing of 10 µm, with a total number of 125 fingers, a total electrode length of 6760 µm, and electrode surface area of 8.45 mm^2.

4.2.3 Capacitance Measurement Setup

Capacitance measurement data were collected using the Instek LCR-821 benchtop LCR meter (New Taipei City, Taiwan), which interfaces with a PC for data acquisition. A graphical user interface (GUI) on the PC was used for sending command signals to the LCR meter. Since the measurement is obtained from non-faradaic current, a 0 V DC bias voltage was applied across the IDE sensor. A 20 mV root mean square (RMS) AC voltage with 20 Hz frequency was applied to the IDE sensors. All capacitance readouts were recorded under 20 µL of 100 µM 1×TE-$MgSO_4$ buffer on the interdigitated electrodes and 50 data points were collected per reading. Capacitance data were analyzed using Matlab (Mathworks) and statistical tests were carried out with R (www.r-project.org). Only $p < 0.05$ values were considered as statistically significant.

4.2.4 Melt Curve Generation for Buffer Optimization

A CFX 96 Real Time system (C1000 Thermal cycler, Bio-Rad) was used to generate melt curves in order to follow DNA probe interactions with complementary and non-complementary target oligos through double stranded DNA (dsDNA) formation under different buffer types and concentrations. For each case fluorescence emission was detected every 5 s from 4 °C to 95 °C at 0.5 °C degree increments. The duplex (dsDNA) formation reaction was carried out under different buffer conditions, specifically, in 1 M and 100 mM 1×TE-NaCl, and 1 mM and 100 µM 1×TE-$MgSO_4$. The DNA probe to DNA target ratio was fixed at 1:1 for 1 µg/µL oligos for all reactions. SYBR Green nucleic acid gel stain (Life Technologies, Carlsbad, CA) was included in all reactions as a real time indicator of the presence of dsDNA.

4.2.5. Pretreatment of the Gold Electrodes Surface

Upon exposure to ambient conditions the gold microelectrode surface is subject to a variety of uncontrolled conditions and contaminants, which can affect thiol reaction kinetics and therefore the probe attachment chemistry; because of this variability, a cleaning step is required immediately prior to functionalization. To prepare the surfaces, the chips with the gold microelectrodes were immersed in a solution of 50 mM KOH and 25% H_2O_2 for 10 min (Fischer et al., 2009), and thoroughly rinsed in Milli-Q water to remove the reagents, followed by oxygen plasma treatment. Baseline capacitance was recorded immediately following chemical cleaning and prior to plasma cleaning and probe immobilization.

4.2.6. Pretreatment of Thiolated Single-Stranded DNA Oligomers

In order for thiol bond formation between the oligo and the gold surface to proceed as expected, the 5’ thiol-modified oligomers require a reduction of the disulfide bonds prior to application. Immobilized TCEP Disulfide Reducing Gel (Thermo Fisher Scientific, Waltham, MA) was washed several times with 100 µM 1×TE-$MgSO_4$ buffer prior to oligo addition in a 2:1 TCEP gel: oligo ratio, and the mixture was incubated for 1 h on a rocker platform at 23^{o}C. After incubation and a 1500 rpm spin for 2 min, the supernatant with reduced thiol-modified oligomers was transferred to a clean tube.

4.2.7 SH-Modified DNA Probe Oligonucleotide Immobilization

Gold IDE sensors were plasma-cleaned for 5 min in an O_2 Plasma Etch PE-25 (Plasma Etch, Carson City, NV, USA) at a pressure of 200 mTorr and 150 W applied to the RF coil immediately before DNA probe incubation. The 10 µM ssDNA probe solution was prepared in 100 µM 1×TE-$MgSO_4$ buffer, and the gold microelectrodes were immersed overnight (15 to 17 h) in 30 µL of the solution, then rinsed copiously with 100 µM 1×TE-$MgSO_4$ buffer and Milli-Q water, and dried with N_2. The IDE sensors were then passivated with 20 µL MCU (5 µM in water) for 45 min to fill vacant gold sites and promote linear orientation of the ssDNA probe molecules. After MCU passivation, the electrodes were rinsed with water and dried with N_2. All reactions were carried out at 23°C.

4.2.8. DNA target hybridization

The IDA sensors were immersed in 20 µL target DNA solutions for 30 min at room temperature, at target concentrations ranging from 1 μL^{-1} to 10^5 μL^{-1} in 100 µM 1×TE-$MgSO_4$ buffer. Following incubation, electrodes were copiously rinsed with 100 µM 1×TE-$MgSO_4$ buffer and dried with N_2.

4.2.9 Fluorescence scanning

Gold IDA sensors were scanned using a FLUOstar Omega fluorescence scanner (BMG LABTECH, Cary, NC). Fluorescent Alexa Fluor 488 and Alexa Fluor 594 signals from the sensors were quantified and analyzed using the FLUOstar Omega software against experimental controls. The paired *t*-test was used for statistical analysis and only $p < 0.05$ values were considered to be statistically significant.

4.3 Results and Discussion

4.3.1 Measurement Setup

The experiments carried out using the functionalized IDE sensors focus on quantifying the key sensor performance metrics of sensitivity and selectivity. To obtain these data, capacitance values of the IDE sensors were measured at four different stages of the sensing process:

1. Cleaned bare gold electrode surfaces. The initial cleaning step was always applied to provide a baseline capacitance response.

2. Electrodes after covalent attachment of thiolated ssDNA probes. The layer of immobilized DNA probes has the intrinsic ability to capture complementary single-stranded target oligonucleotides.
3. Electrodes after incubation with MCU. The measured capacitance at this stage is with the presence of buffer without any target DNA present in the buffer. The MCU is used to block any remaining unoccupied sites on the sensor surface and to align the probes perpendicular to the sensor surface in order to improve hybridization efficiency.
4. Electrodes after incubation and hybridization with ssDNA targets, both complementary and non-complementary.

Capacitance between IDE pairs was obtained by applying a 20 mV RMS AC voltage with a fixed frequency (stimulus) and by measuring the resulting current through the sensor IDE pair (response). The measurements of capacitance with the bare clean electrodes and with immobilized probes are mainly intended for verifying the state of probe immobilization. Unless otherwise stated, the change in capacitance after hybridization with either complementary or non-complementary targets is referred to as the difference between the capacitances before and after hybridization (i.e. capacitance difference between stage 3 and stage 4).

Fig. 4.1A shows a schematic of the IDE sensor and Figs. 4.1B, C, D, and E show the equivalent circuits for stages 1, 2, 3, and 4, respectively. The quantity R_{sol} is the intrinsic buffer solution resistance; R_{leak} is an equivalent resistance representing a leakage current going through the electrode-electrolyte interface; C_{dl} is the double layer capacitance created between the IDEs and adjacent buffer (Fig. 4.1B) resulting from the applied voltage; and C_{geo} is the geometric capacitance which depends on the geometry of the electrodes and their configuration, which may be negligible relative to the double layer capacitance. The quantity C'_{dl} is the double layer capacitance after probe immobilization, and is different from C_{dl} because the ssDNA attachment modifies the surface capacitive characteristics of the electrodes. The additional double layer capacitance $\Delta C_{dl,M}$ results from incubation with MCU, and $\Delta C_{dl,T}$ is the double layer capacitance change due to target hybridization.

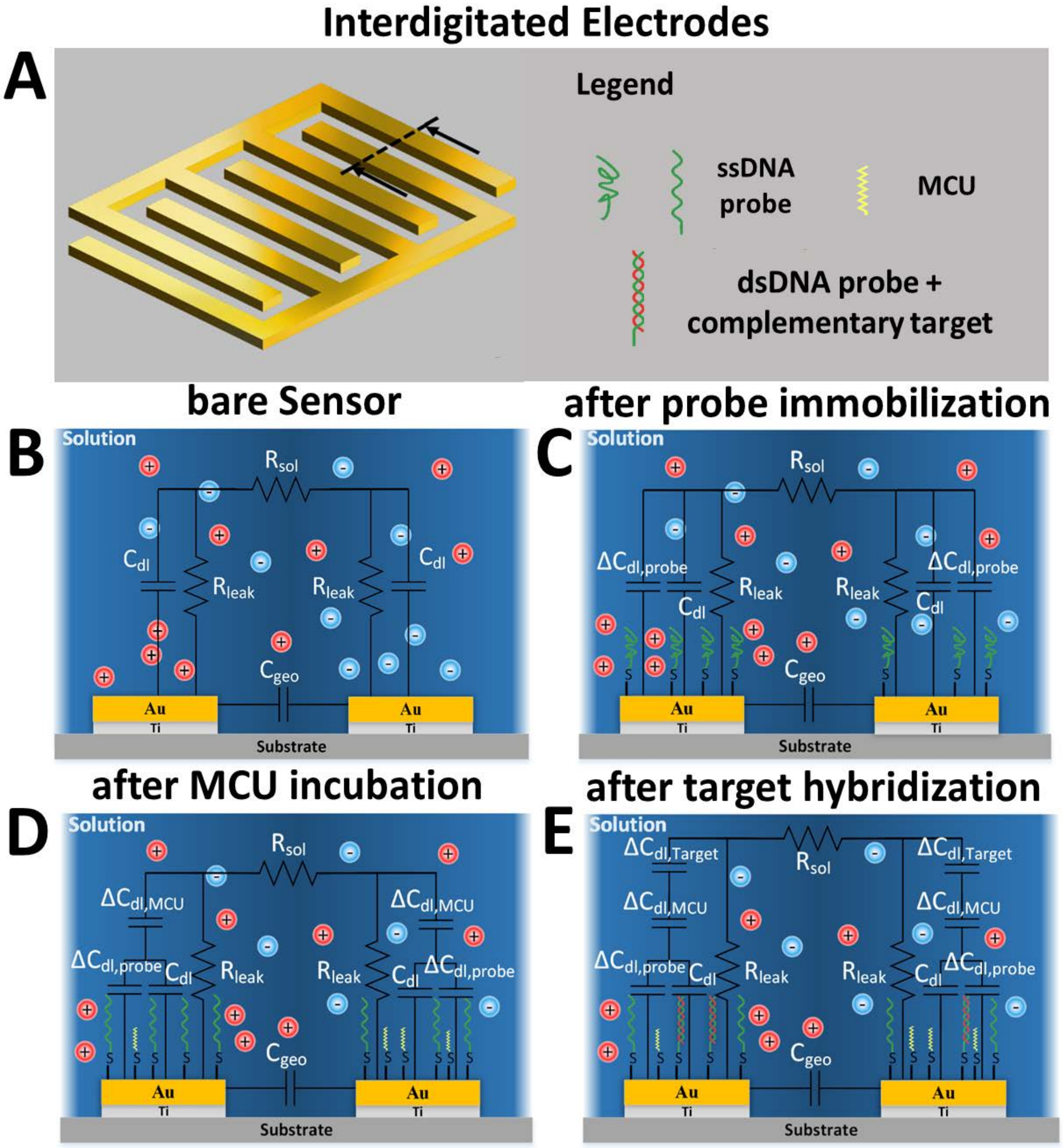

Figure 4.1 Equivalent circuit models on interdigitated electrode (IDE) sensors. (A) Bare IDEs with multiple fingers. (B) Equivalent circuit model for bare IDE sensors. (C) Equivalent circuit model after probe immobilization. (D) Equivalent circuit model after MCU incubation and before target hybridization. (E) Equivalent circuit model after target hybridization for complementary targets.

Because the MCU blocking agent acts as an insulation layer that pushes mobile ions away from the electrode into the solution, the total double layer capacitance is expected to decrease after the MCU step in stage 3. Similarly, after incubation and hybridization with the complementary and non-complementary target DNA in stage 4, the resulting duplex structures should act to repel additional ions away from the electrode surface, resulting in further decreases in the double layer capacitance. These behaviors are illustrated in Figs. 4.1C and D, where the sequential decreases in total double layer capacitance after the MCU and target incubation are denoted by $\Delta C_{dl,M}$ and $\Delta C_{dl,T}$ in a series configuration, and connected to the baseline double layer capacitance, C_{dl}.

4.3.2 Effect of Buffer Composition and Temperature on Hybridization

The specificity of an ssDNA probe is a critical factor that governs the performance characteristics of the biosensor, and which depends in part on electrolyte salt composition, concentration, and temperature. Two widely used salt buffers, each at two different ionic concentrations, 1 M and 100 mM 1×TE-NaCl, and 1 mM and 100 µM 1×TE-$MgSO_4$, were tested to quantify their effect on the degree of hybridization between the probe and complementary and non-complementary targets. Intercalation of the planar SYBR Green fluorophore into dsDNA increases its fluorescence emission dramatically, allowing detection of dsDNA by monitoring fluorescence intensity. SYBR Green fluorescence intensity in RFU (Relative Fluorescence Unit) in the presence of 24-base synthetic probe and complementary/non-complementary targets with increasing temperature is shown in Fig. 4.2A, illustrating double stranded DNA (dsDNA) formation due to DNA probe-target interactions in different buffer conditions and within 4–95°C temperature range. As temperature increases, dsDNA concentrations decrease resulting in decrease in SYBR green fluorescence intensity. To understand the effect of buffer composition on hybridization specificity, fluorescence intensity differences between complementary and non-complementary targets in each buffer type within the temperature range from 4°C to 95°C are shown in Fig. 4.2B. Non-complementary target RFU background seen in the melt curve assay, especially at the lower temperature range (Fig 4.2A), can be attributed to two factors. First, lower temperatures favor non-complementary binding and specificity of duplex formation is increased with an increase in reaction temperature. Second, the conditions with very high target and probe oligo concentrations enhance the formation of primer dimers which contributed to higher SYBR Green signal at the beginning of the assay in the non-complementary target samples.

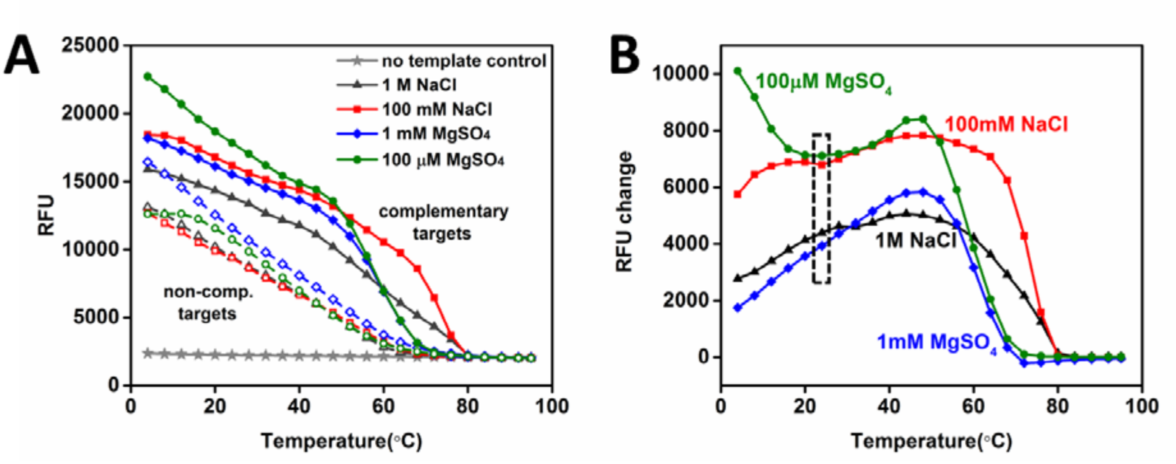

Figure 4.2 Effect of different buffers on DNA hybridization. (A) SYBR Green fluorescence in the presence of complementary (solid line) and non-complementary (dashed line) targets incubated with 24-base ssDNA probe in 1 M 1×TE-NaCl buffer (black), 100 mm 1×TE-NaCl buffer (red), 1mM 1×TE-$MgSO_4$ buffer (blue) and 100 µM 1×TE-$MgSO_4$ buffer (green) within temperature range from 4 ºC to 95 ºC. (B) Corresponding relative fluorescence change between the complementary and non-complementary targets in four different buffers. The black dashed box indicates the temperature used in all the experiments. RFU = Relative fluorescence units.

For three of the four buffers tested, the specificity increased with temperature up to 45°C with the trend reversing at temperatures above 45°C, except for the 100 µM 1×TE-$MgSO_4$ buffer. The specificity from using the 100 µM 1×TE-$MgSO_4$ buffer decreased with temperature up to 23°C, but it is still better than that for all other three salt buffers up to 45°C. For each salt type the specificity increased with decreasing ionic concentration, and this behavior is consistent with other results reported in the literature [41]. At the temperature used for all subsequent hybridization studies (23°C) the 100 µM 1×TE-$MgSO_4$ buffer demonstrates the best hybridization specificity. While low ionic concentrations are beneficial, in general, for achieving high specificity, a potential downside is that a low concentration of monovalent cations may hinder ssDNA probe immobilization on the IDE sensor surface [41]. The negatively charged DNA phosphate backbone, coupled with low cation concentration, may result in unacceptable electrostatic repulsion effects. However, the cation valence has a larger effect on probe immobilization than its concentration, so that bivalent cations, such as Mg^{2+}, can mitigate the repulsion effect, and therefore result in a higher density of immobilized probes on the IDE sensor surface [41]. Furthermore, low ionic concentration serves to reduce measurement interference from the leakage current that often occur due to sodium deposits on the sensor surface. Overall, the 100 µM 1×TE-$MgSO_4$ buffer was found to be the best compromise of composition and concentration to achieve high hybridization specificity without compromising ssDNA probe immobilization, and it was used as the electrolyte buffer for all remaining experiments.

4.3.3 Optimization of Stimulus Signal Frequency

The amount of change measured in double layer capacitance due to target binding is strongly dependent on the frequency of the stimulus AC signal. Since the double layer capacitance at the electrode-electrolyte interface is established due to the displacement of mobile ions in the fluid, it is expected that increasing the stimulus signal frequency will result in gradual disappearance of the double layer capacitance [37]. To gain a better understanding of the sensor's response characteristics as a function of the stimulus signal frequency, a 20 mV RMS AC voltage is applied at three separate frequencies (20 Hz, 100 Hz and 1 kHz). Capacitance values for all four stages were measured for all three frequencies. The results shown in Fig. 4.3A verify changes in capacitance due to probe immobilization compared to the bare clean electrodes (marked as "control" in Fig. 4.3A). The results in Fig. 4.3B illustrate that changes in capacitance before and after hybridization decrease with increase in operating frequency. To maximize sensor sensitivity, 20 Hz was used as the operating frequency for all remaining experiments.

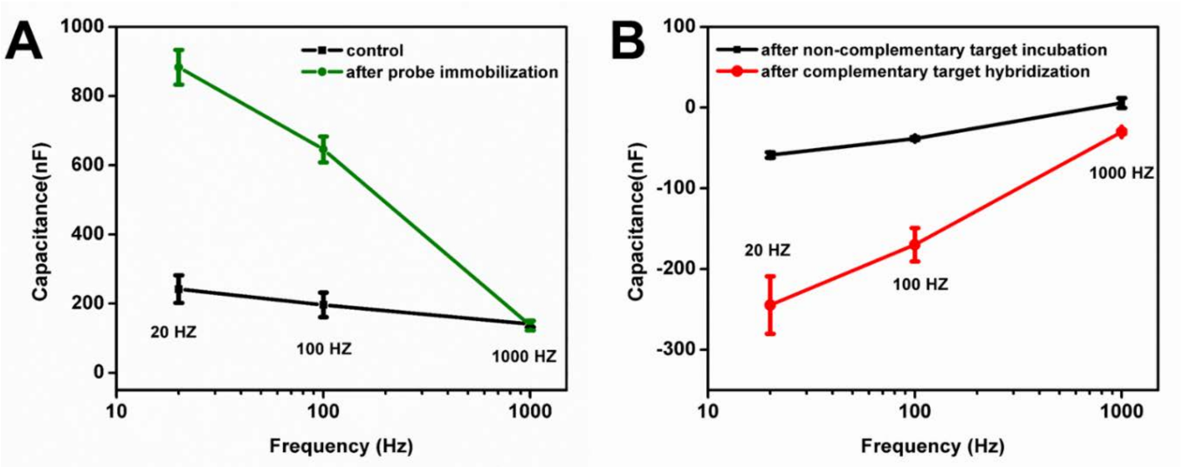

Figure 4.3 Frequency effects on capacitance during each step of sensor preparation/usage. (A) Changes in capacitance after probe immobilization at 20Hz, 100Hz, and 1 kHz frequencies. (B) Changes in capacitance after complementary and non-complementary (control) target hybridization at 20Hz, 100Hz, and 1 kHz frequencies.

4.3.4 Immobilization of Oligonucleotides Probes on Sensor Surface

A protocol for deposition of 5' thiol modified ssDNA probe molecules onto the gold IDE surface and passivation of the IDE surface was established. ssDNA immobilization can be significantly affected by the condition of the IDE surface, the incubation time of 5' thiol-modified ssDNA with the gold surface, and the concentration of ssDNA. In general, the cleaner the IDE surface the better thiol-modified molecules will attach to the gold surface [42]. The IDE sensor surface was cleaned with the protocol described in Section 2.5 and treated with oxygen plasma to promote ssDNA immobilization. In addition to surface cleanliness, ssDNA immobilization is also determined by time the thiol modified ssDNA is in contact with the gold surface. In general, twenty-four hour incubations are required to reach the saturation point for 1 μM ssDNA immobilization in 1M salt conditions, and further exposure results in little additional adsorption [43]. For ssDNA probe concentrations ranging from µM to mM, a surface density in the order of 10^3 cm^{-2} can be obtained after four hours of incubation [37]. In order to maximize sensor functionalization and the number of probes present on the functionalized sensor based on our previous work [19], overnight incubation was chosen for the 10 µM 5' thiol-modified ssDNA probe in our experiments. Probe concentration was set in the µM range based on previous work on the gold electrode DNA biosensors [19] and was further optimized with additional chemical and plasma oxygen cleaning steps to maximize sensor coverage and target capture in 100 µM 1×TE-$MgSO_4$ buffer. To validate 5' thiol-modified ssDNA immobilization on the IDE sensor surface, capacitance measurements were obtained from 3 individual sensors after overnight ssDNA probe incubation, but before passivation with MCU. Fig. 4.4A demonstrates a statistically significant difference ($p < 0.01$) between the average capacitance measurements before and after probe immobilization, indicating that ssDNA probe was immobilized on the IDE surface. To further validate the capacitance results, AlexF488N labeled ssDNA probes were immobilized on IDEs as a complementary assay to monitor probe deposition. Total IDE fluorescence intensities were obtained before and after probe immobilization (Fig. 4.4(B)), showing that incubation with fluorescent ssDNA probe resulted in a significant increase in fluorescence on the IDE ($p < 0.01$) similar to what was observed by capacitance measurements.

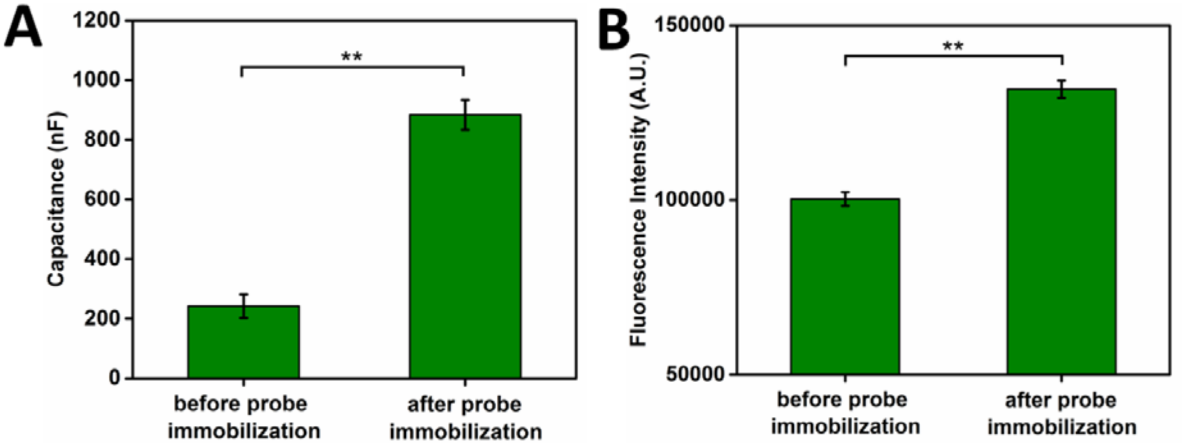

Figure 4.4 Validation of probe immobilization on IDE sensors. (A) Capacitance measurements before and after probe immobilization. (B) The fluorescence intensity before and after probe immobilization. ** paired t-test: $p < 0.01$.

4.3.5 Specificity

After probe immobilization and MCU incubation, specificity tests of complementary and non-complementary DNA targets were conducted. The rate of DNA hybridization is dependent on DNA length, with shorter duplex regions showing higher hybridization rates [38,44]. Based on the 24-base DNA target used in the experiments, target incubation was set for 30 minutes at room temperature (23°C). AlexF594N labeled complementary and non-complementary targets with the concentration of 10^5 μL^{-1} in 20 µL of 100 µM 1×TE-$MgSO_4$ buffer were incubated with the probe immobilized IDE surface, and excess target DNA was washed off. The average capacitance of sensors incubated with complementary and non-complementary target DNAs with the standard error of three individual sensors are shown in Fig. 4.5A. Non-complementary target DNAs did not induce a significant capacitance change, whereas complementary DNA induced a large capacitance change in the sensor. This is further validated using fluorescent target capture on the sensor surface (Fig. 4.5B). Decreased capacitance on IDE surfaces upon target binding has been previously reported in the literature. When ssDNA probes are immobilized on the IDE surfaces, the double layer of ions due to the polarized metal surface are displaced [45]. When complementary DNA strands bind with the probes, the distance between the charge on the surface of the electrode and the ions in the electrolyte increases, resulting in decreasing in the overall capacitance [27,37].

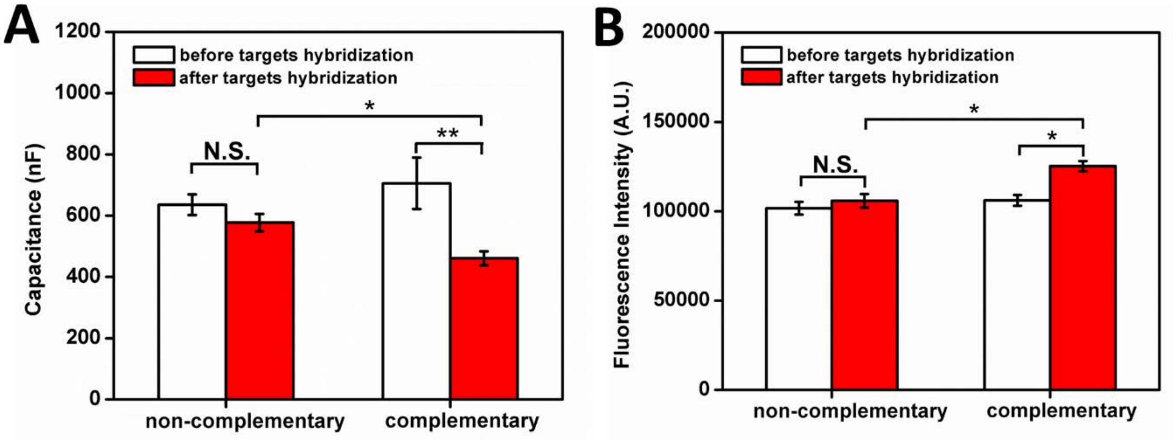

Figure 4.5 Specificity of target hybridization. (A) Capacitance measurements before and after complementary and non-complementary target hybridization. (B) Fluorescence intensity before and after complementary and non-complementary target hybridization. ** paired t-test: $p < 0.01$; * paired t-test: $p < 0.05$.

4.3.6 Sensitivity

To determine the sensitivity of the sensor, DNA concentrations between 0 to 2 million molecules, consistent with the range seen in typical clinical settings, were incubated on the sensor and capacitance was determined (Fig. 4.6). Complementary target DNAs displayed a significant capacitance change as few as 20 DNA molecules, whereas non-complementary DNAs did not significantly change capacitance even at 2×10^6 molecules. For target concentrations between 20 and 2 million DNA molecules, complimentary targets showed a linear response in capacitance change with increasing target concentration, indicating an excellent correlation between low-range target concentrations and capacitance responses. These results demonstrate that the label-free capacitive detection limit for the complementary targets is at least as low as 20

DNA molecules (~1.5 aM). Increasing complementary target concentrations increased capacitance changes, whereas increasing non-complementary DNA concentrations did not significantly increase capacitance. There have been a number of ultra-high sensitive biosensors reported to date which achieved limits of detection similar to the results presented in this paper. Most of these ultra-high sensitive approaches relied on novel amplification methods using nano-materials, such as nano-particles [46] and quantum dots [47]. Other approaches using nano-structures include the use of a novel molecular gate structure with carbon-nanotubes to control sensor's conduction state [48], the use of carbon nanotubes (CNTs) as a highly conductive agent to enhance redox current sensitivity [49], and the use of CNTs combined with Au nano-particles to increase sensor surface area [50]. However, these approaches incur additional costs related to additional sample preparation for nano-materials and amplication, and nano-scale device manufacturing. The biosensor presented in this paper achieved a high sensitivity comparable to those achieved using nano-materials for amplification and other enhancements, thus lowering the cost and simplifying sample processing and device manufacturing requirements.

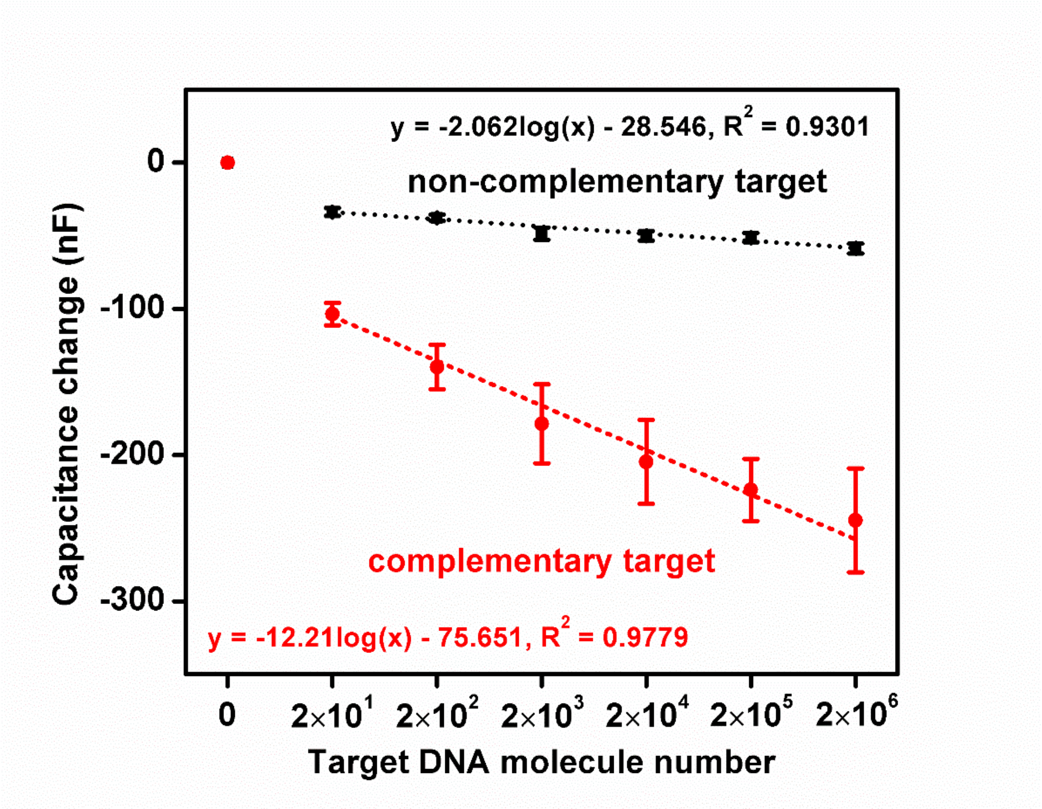

Figure 4.6 Capacitance response from 0 to 2x10^6 complementary (red line) and non-complementary (black line) DNA targets.

4.4 Conclusion

In this paper, a capacitive biosensor with high sensitivity and a wide dynamic detection range is presented. The carefully designed protocol for sensor surface preparation, probe immobilization, and hybridization strikes a balance among the competing factors of ease of immobilization, specificity, and the overall capacitance measurement quality. The reported biosensor improves the state of the art on three fronts. First, the sensor was able to produce an output of more than 70nF in capacitance change in response to as few as 20 complementary DNA targets (0.25 attogram) at a concentration of ~1.5 aM. The magnitude of capacitance change increases linearly with complementary target concentration in the range between 20 and

2 million target DNA molecules. The detection limit of this biosensor is among the lowest reported to date for a non-faradaic capacitive biosensor. Second, sensor specificity is clearly demonstrated by the capacitance change differential between complementary and non-complementary target binding. For non-complementary ssDNA target molecules, the measured change in capacitance is significantly less than that for the complementary ssDNA target and does not display an appreciable change in capacitance with non-complementary molecule concentration increases. Third, the sensor achieved a dynamic range for detection between 1 μL^{-1} and 10^6 μL^{-1} target molecules (20 to 2 million target DNA molecules) with excellent linearity in the measurement of capacitance changes. Combining its performance in sensitivity, specificity, and dynamic detection range, this capacitive biosensor demonstrates the potential to be a viable technology for low-cost, low-power, ease of use, and rapid detection technology that is a critical step toward POC pathogen detection. Areas where further investigations can provide more optimized conditions for the capacitive biosensor include optimized incubation time to decrease time for sample analysis. Furthermore, future development of this capacitive biosensor includes detection of viral nucleic acids (DNA and RNA) from complex biological samples, as well as platform multiplexing, with the ultimate goal of developing a POC device for rapid and multiplexed diagnosis of viral infections in clinical and field settings.

REFERENCES

[1] M. E. J. Woolhouse, A. Rambaut, and P. Kellam, “Lessons from Ebola: Improving infectious disease surveillance to inform outbreak management,” *Sci. Transl. Med.*, vol. 7, no. 307, pp. 307rv5–307rv5, Sep. 2015.

[2] A. Zumla, D. S. Hui, and S. Perlman, “Middle East respiratory syndrome,” *Lancet*, vol. 386, no. 9997, pp. 995–1007, Sep. 2015.

[3] C. A. Daep, J. L. Muñoz-Jordán, and E. A. Eugenin, “Flaviviruses, an expanding threat in public health: focus on dengue, West Nile, and Japanese encephalitis virus,” *J. Neurovirol.*, vol. 20, no. 6, pp. 539–560, Dec. 2014.

[4] L. R. Petersen, D. J. Jamieson, A. M. Powers, and M. A. Honein, “Zika Virus,” *N. Engl. J. Med.*, vol. 374, no. 16, pp. 1552–1563, 2016.

[5] R. W. Peeling and R. McNerney, “Emerging technologies in point-of-care molecular diagnostics for resource-limited settings,” *Expert Rev. Mol. Diagn.*, vol. 14, no. 5, pp. 525–534, Jun. 2014.

[6] M. L. Sin, K. E. Mach, P. K. Wong, and J. C. Liao, “Advances and challenges in biosensor-based diagnosis of infectious diseases,” *Expert Rev. Mol. Diagn.*, vol. 14, no. 2, pp. 225–244, Mar. 2014.

[7] S. Yang and R. E. Rothman, “PCR-based diagnostics for infectious diseases: uses, limitations, and future applications in acute-care settings,” *Lancet Infect. Dis.*, vol. 4, no. 6, pp. 337–348, Jun. 2004.

[8] M. J. Espy, J. R. Uhl, L. M. Sloan, S. P. Buckwalter, M. F. Jones, E. A. Vetter, J. D. C. Yao, N. L. Wengenack, J. E. Rosenblatt, F. R. Cockerill, and T. F. Smith, “Real-time PCR in clinical microbiology: applications for routine laboratory testing.,” *Clin. Microbiol. Rev.*, vol. 19, no. 1, pp. 165–256, Jan. 2006.

[9] W. C. Timmer and J. M. Villalobos, “The polymerase chain reaction,” *J. Chem. Educ.*, vol. 70, no. 4, p. 273, Apr. 1993.

[10] P. Craw and W. Balachandran, “Isothermal nucleic acid amplification technologies for point-of-care diagnostics: a critical review,” *Lab Chip*, vol. 12, no. 14, p. 2469, Jun. 2012.

[11] S. D. Boyd, “Diagnostic Applications of High-Throughput DNA Sequencing,” *Annu. Rev. Pathol. Mech. Dis.*, vol. 8, no. 1, pp. 381–410, Jan. 2013.

[12] G. Ventimiglia and S. Petralia, “Recent Advances in DNA Microarray Technology: an Overview on Production Strategies and Detection Methods,” *Bionanoscience*, vol. 3, no. 4, pp. 428–450, Dec. 2013.

[13] T. G. Drummond, M. G. Hill, and J. K. Barton, “Electrochemical DNA sensors,” *Nat. Biotechnol.*, vol. 21, no. 10, pp. 1192–1199, Oct. 2003.

[14] S. A. Byron, K. R. Van Keuren-Jensen, D. M. Engelthaler, J. D. Carpten, and D. W. Craig, “Translating RNA sequencing into clinical diagnostics: opportunities and challenges,” *Nat. Rev. Genet.*, vol. 17, no. 5, pp. 257–271, May 2016.

[15] W. Pettine, M. Jibson, T. Chen, S. Tobet, P. Nikkel, and C. S. Henry, “Characterization of Novel Microelectrode Geometries for Detection of Neurotransmitters,” *IEEE Sens. J.*, vol. 12, no. 5, pp. 1187–1192, May 2012.

[16] M. I. Montenegro, M. A. Queirós, and J. L. Daschbach, *Microelectrodes: Theory and Applications*. Springer Netherlands, 1991.

[17] S. Gawad, “Substrate arrays of Iridium Oxide microelectrodes for in vitro neuronal interfacing,” *Front. Neuroeng.*, vol. 3, no. January, pp. 1–7, 2009.

[18] G. Li and P. Miao, “Electrochemical Analysis of Proteins and Cells,” 2013.

[19] D. S. Dandy, P. Wu, and D. W. Grainger, “Array feature size influences nucleic acid surface capture in DNA microarrays.,” *Proc. Natl. Acad. Sci. U. S. A.*, vol. 104, no. 20, pp. 8223–8, May 2007.

[20] L. Yang and R. Bashir, “Electrical/electrochemical impedance for rapid detection of foodborne pathogenic bacteria,” *Biotechnol. Adv.*, vol. 26, no. 2, pp. 135–150, Mar. 2008.

[21] J. B. Wydallis, R. M. Feeny, W. Wilson, T. Kern, T. Chen, S. Tobet, M. M. Reynolds, and C. S. Henry, “Spatiotemporal norepinephrine mapping using a high-density CMOS microelectrode array,” *Lab Chip*, vol. 15, no. 20, pp. 4075–4082, Sep. 2015.

[22] C. Stagni, C. Guiducci, L. Benini, B. Ricco, S. Carrara, B. Samori, C. Paulus, M. Schienle, M. Augustyniak, and R. Thewes, “CMOS DNA Sensor Array With Integrated A/D Conversion Based on Label-Free Capacitance Measurement,” *IEEE J. Solid-State Circuits*, vol. 41, no. 12, pp. 2956–2964, Dec. 2006.

[23] S. Bhansali, G. Chornokur, S. K. Arya, C. Phelan, and R. Tanner, “Impedance-based miniaturized biosensor for ultrasensitive and fast prostate-specific antigen detection,” *J. Sensors*, vol. 2011, 2011.

[24] J. S. Daniels and N. Pourmand, “Label-Free Impedance Biosensors: Opportunities and Challenges,” *Electroanalysis*, vol. 19, no. 12, pp. 1239–1257, Jun. 2007.

[25] F. Lisdat and D. Schäfer, “The use of electrochemical impedance spectroscopy for biosensing,” *Anal. Bioanal. Chem.*, vol. 391, no. 5, pp. 1555–1567, Jul. 2008.

[26] W. Bracke, P. Merken, R. Puers, and C. Van Hoof, “Ultra-Low-Power Interface Chip for Autonomous Capacitive Sensor Systems,” *IEEE Trans. Circuits Syst. I Regul. Pap.*, vol. 54, no. 1, pp. 130–140, Jan. 2007.

[27] C. Berggren, P. Stålhandske, J. Brundell, and G. Johansson, “A feasibility study of a capacitive biosensor for direct detection of DNA hybridization,” *Electroanalysis*, vol. 11, no. 3, pp. 156–160, 1999.

[28] L. Moreno-Hagelsieb, “Sensitive DNA electrical detection based on interdigitated Al/Al2O3 microelectrodes,” *Sensors Actuators B Chem.*, vol. 98, no. 2–3, pp. 269–274, Mar. 2004.

[29] C. Guiducci, C. Stagni, A. Fischetti, U. Mastromatteo, L. Benini, and B. Riccoricco, “Microelectrodes on a Silicon Chip for Label-Free Capacitive DNA Sensing,” *IEEE Sens. J.*, vol. 6, no. 5, pp. 1084–1093, Oct. 2006.

[30] K.-H. Lee, J.-O. Lee, M.-J. Sohn, B. Lee, S.-H. Choi, S. K. Kim, J.-B. Yoon, and G.-H. Cho, “One-chip electronic detection of DNA hybridization using precision impedance-based CMOS array sensor,” *Biosens. Bioelectron.*, vol. 26, no. 4, pp. 1373–1379, Dec. 2010.

[31] A. Qureshi, J. H. Niazi, S. Kallempudi, and Y. Gurbuz, “Label-free capacitive biosensor for sensitive detection of multiple biomarkers using gold interdigitated capacitor arrays,” *Biosens. Bioelectron.*, vol. 25, no. 10, pp. 2318–2323, Jun. 2010.

[32] W. C. Eberhardt, Y. A. Shakhsheer, B. H. Calhoun, J. R. Paulus, and M. Appleby, “A bio-inspired artificial whisker for fluid motion sensing with increased sensitivity and reliability,” in *2011 IEEE SENSORS Proceedings*, 2011, pp. 982–985.

[33] S. S. Kallempudi and Y. Gurbuz, “A nanostructured-nickel based interdigitated capacitive transducer for biosensor applications,” *Sensors Actuators B Chem.*, vol. 160, no. 1, pp. 891–898, Dec. 2011.

[34] S. Wright and T. Chen, “A PVT-compensated capacitive sensor with sub-1fF sensitivity,” *Midwest Symp. Circuits Syst.*, vol. 2015-Septe, 2015.

[35] C. Berggren, P. Stålhandske, J. Brundell, and G. Johansson, “A Feasibility Study of a Capacitive Biosensor for Direct Detection of DNA Hybridization,” *Electroanalysis*, vol. 11, no. 3, pp. 156–160, Mar. 1999.

[36] J. C. Love, L. A. Estroff, J. K. Kriebel, R. G. Nuzzo, and G. M. Whitesides, “Self-Assembled Monolayers of Thiolates on Metals as a Form of Nanotechnology,” *Chem. Rev.*, vol. 105, no. 4, pp. 1103–1170, Apr. 2005.

[37] C. Guiducci, “DNA detection by integrable electronics,” *Biosens. Bioelectron.*, vol. 19, no. 8, pp. 781–787, Mar. 2004.

[38] A. B. Steel, R. L. Levicky, T. M. Herne, and M. J. Tarlov, “Immobilization of Nucleic Acids at Solid Surfaces: Effect of Oligonucleotide Length on Layer Assembly,” *Biophys. J.*, vol. 79, no. 2, pp. 975–981, Aug. 2000.

[39] N. Oliveira, E. Souza, D. Ferreira, D. Zanforlin, W. Bezerra, M. Borba, M. Arruda, K.

Lopes, G. Nascimento, D. Martins, M. Cordeiro, and J. Lima-Filho, “A Sensitive and Selective Label-Free Electrochemical DNA Biosensor for the Detection of Specific Dengue Virus Serotype 3 Sequences,” *Sensors*, vol. 15, no. 7, pp. 15562–15577, Jul. 2015.

[40] B. Mattiasson and M. Hedström, “Capacitive biosensors for ultra-sensitive assays,” *TrAC - Trends Anal. Chem.*, vol. 79, pp. 233–238, 2016.

[41] *,†,‡ Dmitri Y. Petrovykh, §. Hiromi Kimura-Suda, ‡ and Lloyd J. Whitman, and M. J. Tarlov§, “Quantitative Analysis and Characterization of DNA Immobilized on Gold,” 2003.

[42] Y. Su, V. G. Kravets, S. L. Wong, J. Waters, A. K. Geim, and R. R. Nair, “Impermeable barrier films and protective coatings based on reduced graphene oxide,” *Nat. Commun.*, vol. 5, no. 1, p. 4843, Dec. 2014.

[43] T. M. H. and and M. J. Tarlov, “Characterization of DNA Probes Immobilized on Gold Surfaces,” 1997.

[44] D. Noble, “DNA Sequencing on a Chip,” *Anal. Chem.*, vol. 67, no. 5, p. 201A–204A, Mar. 1995.

[45] C. Berggren, B. Bjarnason, and G. Johansson, “Capacitive biosensors,” *Electroanalysis*, vol. 13, no. 3, pp. 173–180, 2001.

[46] H. Li, Z. Sun, W. Zhong, N. Hao, D. Xu, and H.-Y. Chen, “Ultrasensitive Electrochemical Detection For DNA Arrays Based on Silver Nanoparticle Aggregates,” *Anal. Chem.*, vol. 82, no. 13, pp. 5477–5483, Jul. 2010.

[47] W. Shen and Z. Gao, “Quantum dots and duplex-specific nuclease enabled ultrasensitive detection and serotyping of Dengue viruses in one step in a single tube,” *Biosens. Bioelectron.*, vol. 65, pp. 327–332, Mar. 2015.

[48] M. Nuzaihan M.N., U. Hashim, M. K. Md Arshad, S. R. Kasjoo, S. F. A. Rahman, A. . Ruslinda, M. F. M. Fathil, R. Adzhri, and M. M. Shahimin, “Electrical detection of dengue virus (DENV) DNA oligomer using silicon nanowire biosensor with novel molecular gate control,” *Biosens. Bioelectron.*, vol. 83, pp. 106–114, Sep. 2016.

[49] G. Nie, Z. Bai, J. Chen, and W. Yu, “Simple Label-Free Femtomolar DNA Detection Based on a Nanostructure Composite Material: MWNT-Doped Poly(indole-6-carboxylic acid),” *ACS Macro Lett.*, vol. 1, no. 11, pp. 1304–1307, Nov. 2012.

[50] S. Wang, L. Li, H. Jin, T. Yang, W. Bao, S. Huang, and J. Wang, “Electrochemical detection of hepatitis B and papilloma virus DNAs using SWCNT array coated with gold nanoparticles,” *Biosens. Bioelectron.*, vol. 41, pp. 205–210, Mar. 2013.

CHAPTER 5: AN ULTRA-SENSITIVE CAPACITIVE MICROWIRE SENSOR FOR PATHOGEN-SPECIFIC SERUM ANTIBODY RESPONSES[4]

5.1 Introduction

Detecting and analyzing the humoral antibody response in clinical samples is critical for diagnosis of infectious disease, understanding pathogenesis and immune response kinetics, and vaccine development [1]. Current methods for antibody detection include immunoprecipitation (e.g., hemagglutination), immunoblotting, plaque reduction neutralization tests, and immunosorbent assays [2]. Among these methods, the enzyme-linked immunosorbent assay (ELISA) is used as the gold standard clinical diagnostic tool for antibody detection [3]. However, established detection techniques, including ELISAs, require large instrumentation in centralized laboratories and specialized training to execute and interpret the results [4,5]. These disadvantages limit the use of ELISAs in low-resource settings [4,6]. When standard laboratory tools are not locally accessible, samples must be collected, stored under specific conditions, and sent to reference laboratories, which leads to additional turnaround time. As a result, many cases go undiagnosed and this indicates an urgent need for sensitive and robust assays that can be used at the point of care (POC) to quickly diagnose infection and provide health-care providers with actionable information.

As one branch of electrochemical immunosensors, capacitive biosensors employ direct sample application for label-free detection. Other electrochemical antibody sensors have been developed for serological analysis, but these designs incorporate enzymatic labels [7,8] or toxic

---

[4] Lei Wang, Brian Geiss and David Dandy conceived and designed the study. Lei Wang, Jessica Filer and Meghan Lorenz designed and performed experiments and analyzed data. Lei Wang. and Jessica Filer wrote the manuscript, on which Brian Geiss. and David Dandy also assisted.

redox couples [9] that increase the complexity and cost of the sensor. Compared to other immunosensors, capacitive biosensors are ideal candidates for sensitive and label-free bioanalysis platforms. Capacitive sensing is based on the underlying theory of the electrical double layer [10,11], where the working electrode is conjugated with probe that binds its respective target to increase the thickness of the double layer. This increase in double layer width produces a corresponding change in capacitance [12,13]. Such capacitive signals provide a direct measure of target binding and can be rapidly detected. Based on our previous work using capacitive change to detect DNA [12], the sensitivity of capacitive biosensors is far superior to traditional diagnostic assays [12–15] and is ideal for the detection of low antibody titers found during early stages of infection. Capacitive biosensors are thus an attractive sensing modality that has not yet been fully explored for specific antibody detection.

The goal of this work is to develop a novel POC platform that can specifically detect low levels of antigen-specific antibodies in serum. Due to its clinical relevance, Zika virus (ZIKV) was chosen as a model system to validate the sensing platform. ZIKV is an emerging Flavivirus that is closely related to other mosquito-borne viruses of clinical importance, such as Yellow Fever, West Nile, and dengue viruses. It has become a major public health concern due to neurological complications in infected adults [16–19] or severe developmental complications for fetuses of infected women [20–24]. Therefore, accurate and early diagnosis of ZIKV infection is essential for proper monitoring and medical intervention in these cases.

In this study, we developed a capacitive immunosensor that specifically detects ZIKV and Chikungunya (CHIKV) antibodies by the recognition of their respective envelope (E) protein. The sensor presented here directly measures ZIKV-specific monoclonal antibody, with a lower detection limit of approximately 10 antibody molecules in a 30 µL sample. The antibody detection system discriminates between virus specific antibodies with little cross-reactivity, indicating a high degree of selectivity, and can even differentiate antibody isotypes. We also demonstrate that our system can specifically and sensitively detect polyclonal anti-ZIKV antibodies present in mouse serum. This method is distinguished from previous antibody detection methods not only in the platform, but also by its superior sensitivity and specificity.

5.2 Experimental section

5.2.1 Study design

The purpose of this study was to build a sensitive capacitive biosensor for the specific detection of ZIKV antibody. The working microwire surface was functionalized with E protein from either ZIKV (ZIKV E) or Chikungunya virus (CHIKV E). Detection limits for the device were first determined with monoclonal antibody samples. Anti-ZIKV E antibody was employed as a specific target while anti-CHIKV E, anti-Dengue, and anti-M13 were used as nonspecific targets. The microwire biosensor was also used to isotype the monoclonal antibodies with anti-mouse IgG1, IgG2a, IgG2b, IgG3, IgA and IgM antibodies. The microwire sensor was then validated using pre-immune and immune mouse serum collected 4, 7, 14 and 21 days post ZIKV immunization. Next, the sensor was used to isotype Day 4 and 21 mouse sera for IgM and IgG antibody.

Information for development of DNA vaccine vectors, immunization protocol, serum collection, Western blots and ELISAs confirming antibodies in serum are described in Supplemental Information. Representative serum samples positive for ZIKV IgG antibody by Western blot were included in the serum testing. Three experimental replicates were performed for each monoclonal antibody and serum sample. Control samples and experimental sample replicates are indicated in the text and figure legends.

5.2.2 Materials and equipment

Potassium hydroxide (KOH), iron (III) chloride hexahydrate ($FeCl_3{\cdot}6H_2O$), 30% hydrogen peroxide (H_2O_2), and absolute ethanol were purchased from Fisher Scientific (Fairlawn, NJ). High-purity silver ink was purchased from SPI Supplies (West Chester, PA). 11-Mercaptoundecanoic acid (MUA) was purchased from Santa Cruz Biotechnology (Dallas, TX). 3-Mercapto-1-propanol (MPOH) was purchased from Tokyo Chemical Industry Co., Ltd. (Portland, OR). N-Hydroxysuccinimide (NHS) and 1-Ethyl-3-(3-dimethylaminopropyl)-carbodiimide (EDC) were purchased from Acros Organics (Geel, Belgium). Ethanolamine, Tween-20, and 2-(N-morpholino) ethanesulfonic acid (MES) was purchased from Sigma-Aldrich (St. Louis, MO). Phosphate buffered saline (1× PBS: 137 mM NaCl, 2.7 mM KCl, 10 mM Na_2HPO_4 and 1.8 mM KH_2PO_4, pH 7.4) was purchased from Hyclone (Logan, UT). All reagents were used as received without further purification. All stock solutions were prepared using ultrapure water (18 MΩ cm) purified with the Nanopure System (Kirkland, WA). 99.99% pure gold (25 µm) and silver (25 µm) wires were purchased from California Fine Wire Company (Grover Beach, CA) and used as the working and reference electrode materials, respectively.

Recombinant ZIKV E, recombinant CHIKV E, and mouse monoclonal anti-CHIKV E antibodies were purchased from MyBioSource, Inc. (San Diego, CA) and stored at –20°C until use. M13 antibody (Abcam ab24229), anti-dengue 2 envelope antibodies (Abcam ab80914), and ZV-2 Anti-Zika envelope antibody [25] were generously provided by Dr. Michael Diamond. ZIKV immune mouse serum was generated after DNA immunization of mice with ZIKV virus-like particle expression plasmids modeled from previous work [26]. Details for the construction of the immunization plasmids, immunization, serum collection, and initial antibody testing of serum can be found in Supplemental information. Anti-Mouse IgG1, IgG2a, IgG2b, IgG3, IgG, IgA and IgM antibodies were purchased from BD Biosciences (San Jose, CA), and stored at 4°C until use.

5.2.3 Working electrode surface functionalization

The 25 µm diameter Au microwire was used as the working electrode. To prepare the surface of the electrodes, the Au microwire was immersed in a 20 mL solution of 50 mM KOH and 25% H_2O_2 for 10 min [27], and thoroughly rinsed in Milli-Q water to remove residual reagent. The Au microwire was then plasma cleaned for 2 min in an O_2 Plasma Etch PE-25 (Plasma Etch, Carson City, NV, USA) at a pressure of 200 mTorr and with 150 W applied to the RF coil. An alkanethiol self-assembling monolayer (SAM) layer formation reaction was performed immediately after plasma cleaning. A 10 mM mixed solution consisting of a 1:1 ratio of 3-MPOH (3-Mercapto-1-propanol) to 11-MUA (11-Mercaptoundecanoic acid) was prepared in the absolute ethanol. The gold microwires were immersed in the mixed solution for 48 hours without light at room temperature and then rinsed three times with deionized water to remove residual reagent.

The MUA carboxyl groups on the SAM were immediately activated for antigen coupling by a two-step NHS/EDC bioconjugation protocol. The SAM modified gold microwires were incubated in 20 mL of 20 mM EDC and NHS in 0.1 M MES (2-(N-morpholino) ethanesulfonic acid) (pH 6.0) buffer for 30 minutes and then rinsed with 20 mL 0.1 M MES buffer. A solution of 8 µg/mL antigen (ZIKV E or CHIKV E) was incubated on the activated MUA surface for 2 hours. After antigen incubation, the surface was incubated in 0.1 M ethanolamine in 1× PBS solution for 30 min to passivate unbound, activated MUA. The wire was rinsed with 1× PBS, incubated for 10 minutes, then rinsed three times with 30 µL of 0.1× PBS buffer before baseline measurements.

5.2.4 Microwire chip fabrication

The capacitive sensor was constructed using a glass substrate with a polydimethylsiloxane (PDMS) layer 1 mm in height, and two metal microwires. Liquid sample confinement was achieved by making a 6 mm diameter hole in the hydrophobic PDMS that was bonded on a hydrophilic glass slide. To make the PDMS layer, PDMS prepolymer [RTV 615 A and B (10:1, w/w)] was mixed, degassed, then poured onto a flat silicon wafer to yield a 1 mm-thick fluidic layer [28]. The PDMS layer was baked for 30 min at 80°C, then peeled from the silicon wafer. A biopsy punch (Technical Innovations, FL, Inc. USA) was used to create 6 mm diameter wells for sample containment. Both the PDMS and glass were exposed to oxygen plasma (Plasma Etch, NV, USA) for 1 min, then contacted to form a permanent bond. On the PDMS with a 6-mm diameter well, Ag/AgCl and Au microwires were spaced 1 mm apart across the well. A two-electrode system was employed using Au and Ag/AgCl microwires as the working and reference electrodes, respectively, each with a surface area of 4.7×10^{-3} cm^2. Ag/AgCl reference electrodes were made by dipping silver Ag wire in 50 mM iron (III) chloride for 50 s, forming a silver chloride layer on the surface. Silver paint was applied to wire ends to create touchpads that could be connected to the capacitance reader.

5.2.5 Capacitance measurement device and setup

Capacitance measurement data were collected using an Instek LCR-821 benchtop LCR meter (New Taipei City, Taiwan) with a PC interface for data acquisition. Because double layer capacitance is a non-faradaic signal, a 0 V DC bias voltage was applied. A 20 mV root mean square (RMS) AC voltage was applied to the sensors at frequencies of 20 Hz. All capacitance readouts were recorded in parallel mode in 30 µL of 0.1× PBST and 60 data points were collected per reading. A faradic cage was used to remove electrical interference during readout.

Capacitance data was analyzed using Matlab (Mathworks) and statistical tests were performed using *R* (www.r-project.org). Only *p* values less than 0.05 were considered statistically significant.

5.2.6 Monoclonal antibody detection and antibody isotype detection

For antibody detection, 30 µL dilution of monoclonal antibody was added to the micro-well and incubated for 5 min at room temperature in 1× PBST buffer containing 1 to 10^3 molecules of each monoclonal antibody. Following incubation, electrodes were rinsed three times with 1× PBST buffer and three times with 0.1× PBST buffer.

For antibody isotype determination, a 30 µL monoclonal CHIKV E antibody was added to the micro-well and incubated for 5 min at room temperature in 1× PBST buffer. Electrodes were rinsed with 1× and 0.1× PBST, and then antibodies specific for each isotype were added to the well with dilutions of 1 to 10^3 anti-isotype antibody molecules in 1× PBST buffer. Following incubation, electrodes were rinsed again three times with 30 µL 1× PBST buffer and three times with 30 µL 0.1× PBST buffer. Capacitance measurements were then performed as described in the Capacitance Measurement and Device Setup section.

5.2.7 Mouse serum sample antibody detection and antibody isotype detection

Clarified mouse sera were diluted $1:10^6$ and $1:10^{12}$ in 30 µL 1× PBST buffer, and incubated on microwire chips for 5 min at room temperature. Following incubation, electrodes were rinsed three times with 30 µL 1× PBST buffer and three times with 30 µL 0.1× PBST buffer. To determine the isotype of anti-ZIKV antibodies in the mouse sera the microwire sensor was first immersed in 30 µL of mouse serum diluted $1:10^6$ in 1× PBST for 5 min at room temperature. Antibodies specific for each isotype were then incubated for 5 min at dilutions of $1:10^6$ and $1:10^{12}$ in 30 µL 1× PBST buffer. Following incubation, electrodes were rinsed three times with 30 µL 1× PBST buffer and three times with 0.1× PBST buffer prior to capacitance reading.

5.3 Results and discussion

5.3.1 Sensor design and working principles

The label-free capacitive immunosensor introduced here uses microwire electrodes for sensitive and rapid detection of antibodies produced during the host immune response to infection, in this case antibodies against ZIKV. The device is made of low-cost, easily acquired materials. A glass slide is used as the base substrate with a biocompatible polydimethylsiloxane (PDMS) well for sample application. Au and Ag/AgCl microwires (working and reference electrodes respectively) are immobilized across the PDMS well (Figure 5.1a) and 30 µL of liquid sample is added to the well and incubated for 5 min. Measurements can then be taken in as quickly as one minute. Microelectrode wires, compared to other electrode fabrication methods like ink printing, paste, and sputter-coated electrodes, demonstrate increased mass transport rates due to radial diffusion [29]. This increases the current density and consequently improves sensitivity and enhances detection limits [30]. In addition, microelectrodes hold additional benefits of simple fabrication without expensive equipment, ease of surface chemical modification, and availability in different pure and alloyed compositions [31].

The capacitance at the electrode/solution interface in our system can be modeled as several capacitors in series, as visualized in Figure. 5.1b. The first component constitutes the insulating SAM layer on the electrode surface, C_{SAM}. The second, C_{Ag}, includes the anchoring groups and the recognition element (antigen), which is followed by the concentration-dependent antibody layer, C_{Ab}. Based on this model, the specific binding of antibody to antigen results in a change in the total capacitance, C_{tot}. C_{SAM} is generally large and constant and its contribution to the C_{tot} may therefore be ignored. The sensitivity of the sensor is predominately determined by the relative capacitance between antigen and antibody. In this case, use of a large analyte like antibody increases the sensitivity of our sensor by creating a proportionally larger increase in double layer width compared to smaller analytes like antigens [32] . This ultra-sensitivity is necessary to adapt the immunosensor for pre-symptomatic pathogen detection, which is currently only achieved by nucleic acid testing (NAT) [33].

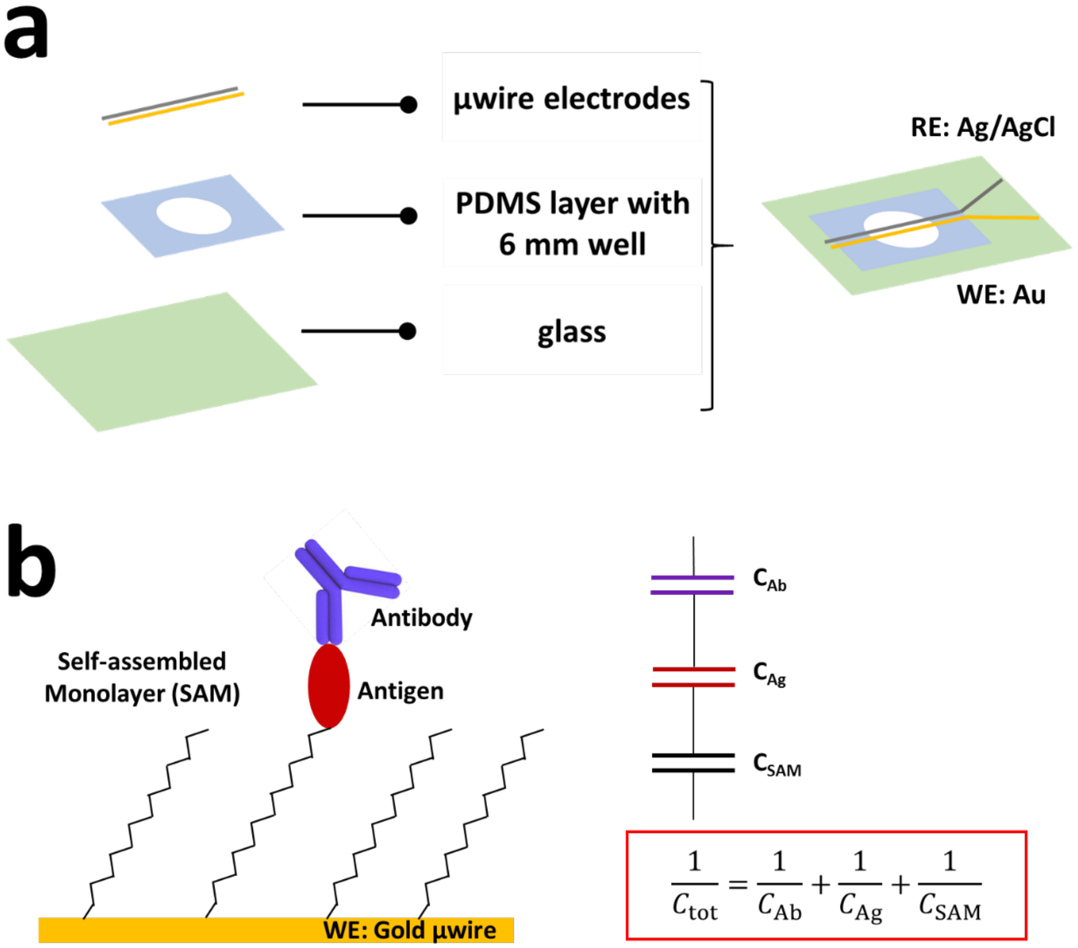

Figure 5.1 Schematic of capacitive immunosensor design and working principles. (**a**) The device layers and resulting immunosensor shown from the top. RE: reference electrode, WE: working electrode; (**b**) Working electrode (Au microwire) surface chemistry and functionalized layers, with the corresponding equivalent series circuit and total capacitance equation.

5.3.2 Specificity tests and detection limit with monoclonal antibodies

To characterize the performance of the capacitive immunosensor, the microwire sensor immobilized with ZIKV E (probe) was first tested with monoclonal antibodies diluted in 1× PBST buffer (pH 7.4, 0.05% Tween 20). Anti-ZIKV E (experimental sample), anti-M13 antibody (control sample), anti-CHIKV E (control sample), and anti-DENV antibody (control sample) were tested (Figure 5.2a). Each antibody was applied to the sensor at concentrations ranging from 1 to 10^3 molecules per 30 µL. The mean negative capacitance changes, $-\Delta C = -(C_{Ab} - C_{BL})$, (where BL = baseline) for each antibody sample with standard deviations ($n = 3$) are presented in Figure 5.2b. The $-\Delta C$ obtained from anti-ZIKV E is proportional to the concentration/number of antibodies in the experimental sample and can be fit with linear regression as shown in the Figure 5.2b ($R^2 = 0.9813$). These results demonstrate that the magnitude of the capacitance change for the sensor is proportional to the concentration of the specific target bound. In comparison, the $-\Delta C$ from control samples have no significant change at any concentration tested, suggesting that there was no significant binding between ZIKV E and control antibodies. In addition, it is notable that the $-\Delta C$ obtained from anti-ZIKV E antibody sample containing 10 molecules is statistically significantly different from the control antibody samples, indicating that the present detection platform has a detection limit as low as 10 antibody molecules/30 µL, far superior to that of other immunosensors or ELISA assays [14]. To demonstrate that the device can be adapted to other antigen/antibody pairs, the sensor was functionalized with CHIKV E2 antigen and tested with the same four monoclonal antibodies at the same concentration ranges (Figure 5.2c). As expected, the $-\Delta C$ obtained from anti-CHIKV E antibody is proportional to the concentration/number of corresponding anti-CHIKV E antibody and is fitted via linear regression shown in the Figure 5.2d ($R^2 = 0.9466$). The other three nonspecific antibodies did not induce significant responses. Again, the $-\Delta C$ obtained from anti-CHIKV E antibody sample containing 10 molecules is statistically significantly different from the three non-specific antibodies, which confirms a detection limit of 10 antibody molecules/30 μL.

Collectively, these results show that the immunosensor functionalized with specific antigen can selectively capture antigen-specific antibodies at extremely low concentrations without nonspecific binding from other tested antibodies. This suggests an excellent combination of specificity and sensitivity for this platform.

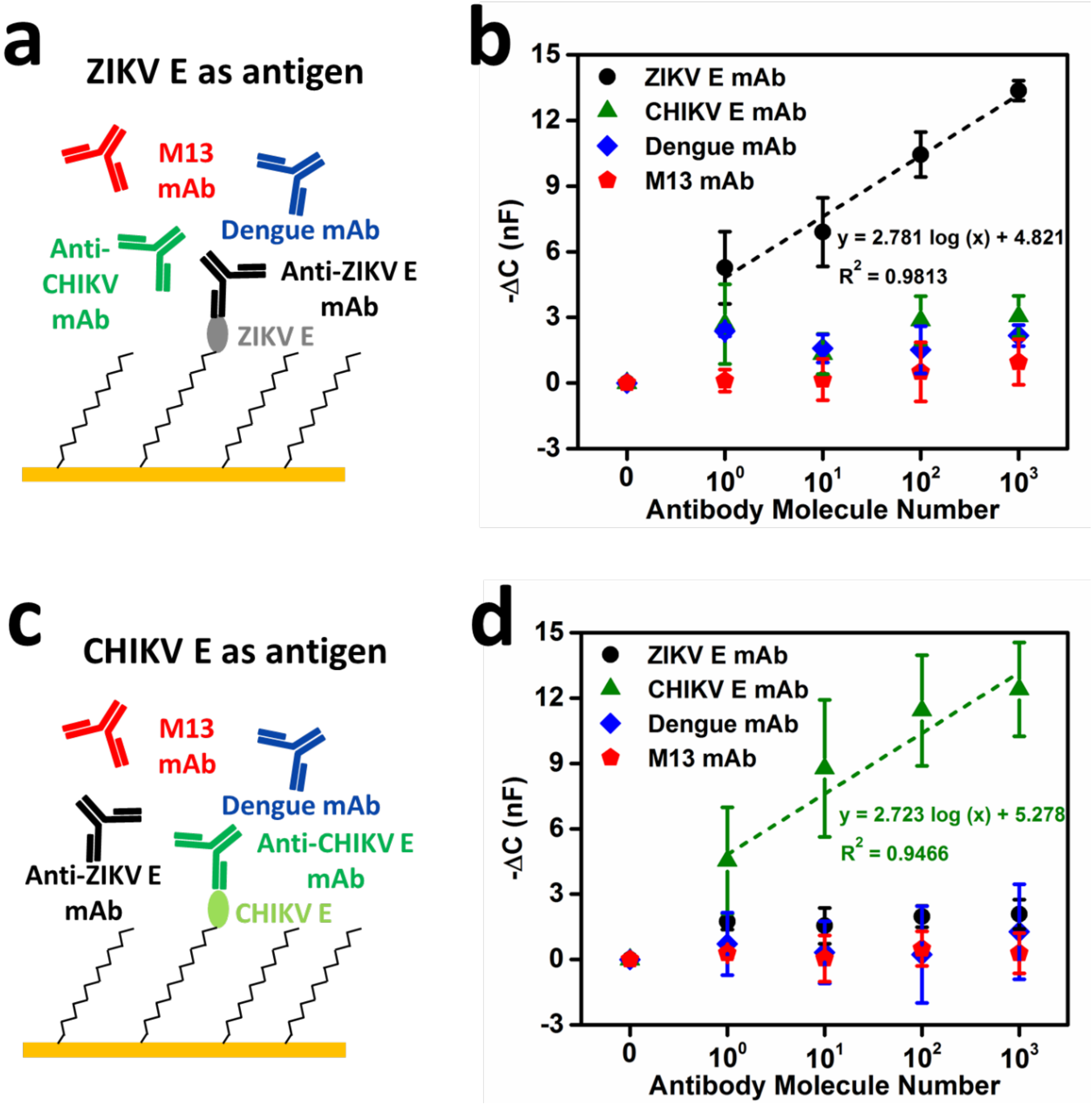

Figure 5.2 Specificity tests with monoclonal antibodies. a) Illustration of ZIKV E antigen as the recognition element to test one specific and three nonspecific antibodies; (**b**) Capacitance responses for the four antibodies at concentrations from 0 to 10^3 molecules per 30 µL in 1× PBST buffer (*n* = 3 at each concentration, mean ± STD). The linear fit for specific anti-ZIKV E is shown in the plot as a dashed line; (**c**) Illustration of CHIKV E antigen as the recognition element to test one specific and three nonspecific antibodies; (**d**) Capacitance responses for four antibodies at concentrations from 0 to 10^3 molecules per 30 µL in 1× PBST buffer (*n* = 3 at each concentration, mean ± STD). The linear fit for specific anti-CHIKV E is shown in the plot as a dashed line.

5.3.3 Isotyping tests with monoclonal antibodies

The isotype of antigen-specific antibodies is commonly determined to elucidate the stage of an infection, with IgM antibodies being present early in infection and IgG antibodies present later in infection. To explore if our platform can be used to determine antibody isotypes, the microwires were functionalized with CHIKV E antigen probe and subsequently saturated with corresponding IgG 2b antibody against CHIKV E (10^3 molecule/ 30 µL). The capacitance value for anti-CHIKV antibody was set as a new baseline ($\mathrm{C_{BL}}$). The devices were then incubated with six secondary antibodies with different anti-mouse antibody specificities (IgG1, IgG2a, IgG2b, IgG3, IgA and IgM) at concentrations ranging from 1 to 10^3 molecules per 30 µL (Figure 5.3a). Figure 5.3b presents the mean negative capacitance changes, $-\Delta \mathrm{C} = -(\mathrm{C_{anti-iso\,Ab}} - \mathrm{C_{BL}})$ for each antibody sample with standard deviations (*n* = 3). As predicted by the circuit model, an additional capacitance change was observed from specific anti-IgG2b antibody samples in all the concentrations applied. In addition, the $-\Delta \mathrm{C}$ of anti-IgG2b antibody increases proportionally with increasing concentrations of anti-IgG2b antibodies. In contrast, the five nonspecific anti-isotype antibodies did not increase capacitance responses (Figure 5.3b). Supporting previous results of the detection limit, the capacitance of 10 anti-IgG 2b antibody molecules/30 µL is statistically significantly different from the nonspecific antibodies. These results indicate that our system can accurately determine the isotype of ultralow concentrations of antigen-specific antibodies.

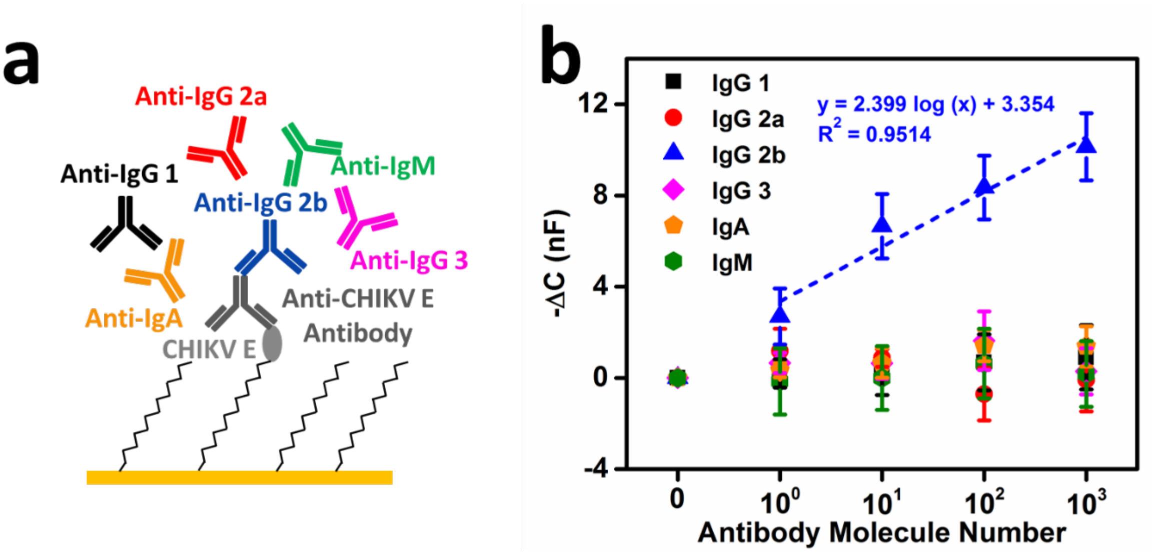

Figure 5.3 Isotyping tests with monoclonal antibodies. (**a**) Illustration of CHIKV E antigen-antibody complex to determine the isotype of anti-CHIKV E (IgG 2b). Six secondary antibodies are used here to perform the test: anti-IgG1, anti-IgG2a, anti-IgG2b, anti-IgG3, anti-IgA and anti-IgM; (**b**) Capacitance responses of the isotype tests with six secondary antibodies at concentrations from 0 to 10^3 molecules per 30 µL in 1× PBST buffer ($n = 3$ at each concentration, mean ± STD). A linear fit is shown in the plot for secondary IgG2b antibody.

5.3.4 Detection of anti-ZIKV antibodies during an immunization time-course

To explore the performance of the capacitive immunosensor in a complex matrix with various interfering species, we tested if ZIKV-specific polyclonal antibodies could be detected in mouse serum. Ten CD1 mice were administered with a DNA vaccine for ZIKV and serum samples were collected before vaccination (pre-immune samples), and 4, 7, 14 and 21 days after vaccination. To confirm a Day 21 anti-ZIKV immune response, the samples were first tested for IgG antibody using strip Western blots and ZIKV-infected Vero cell lysates as the antigen (Fig. S5.1). Of the 10 vaccinated mice, two with strong anti-Zika IgG antibody responses (mice 3 and 4) and one with a weak anti-Zika IgG antibody response (mouse 6) were chosen for further analysis. Mouse 3, 4, and 6 samples were tested with the ZIKV E functionalized sensor. To determine suitable dilutions of the mouse serum samples for the platform, the pre-immune and

Day 4 mouse sera were tested with a wide range of concentrations (1:10^{18} to 1:10^{3} dilutions in 1× PBST). As shown in Fig S5.2, the average $-\Delta C$ obtained from the Day 4 serum increases along with increased concentration and the pre-immune sera conversely shows no significant change in the average $-\Delta C$ across the dilution range. There is no significant difference between pre-immune and Day 4 serum at dilutions lower than 1:10^{12}. All dilutions at and above 1:10^{12} show statistically significant differences with p-values less than 0.05 (Fig S5.2). These results indicate that this platform can differentiate vaccinated from non-vaccinated mouse serum at ultra-dilute concentrations as low as 1:10^{12} and as few as four days after vaccination, which is comparable to the early acute phase of infection before or concurrent with disease symptomology [34]. Subsequently, this assay can extend the window of antibody detection into the early acute phase of infection.

Based on the results in Fig S5.2, two dilutions of the mouse serum, 1:10^{6} and 1:10^{12} were chosen for detection for Day 4, 7, 14 and 21 mouse serum samples. Each of the three biological replicates was tested and averaged. Every biological replicate is the average of three technical replicates. The $-\Delta C$ for each post-vaccination sample was compared to the pre-immune sample as shown in Figure 5.4a and Figure 5.4b. At a 1:10^{12} dilution, the $-\Delta C$ increases with each time point after vaccination, and saturates around Day 14. The lower $-\Delta C$ for Day 14 can be attributed to its smaller sample size as there was no serum collected for mouse 6 on this day. Although results are similar for the 1:10^{6} dilution compared to the 1:10^{12} dilution, it is notable that the $-\Delta C$ for this dilution saturates as early as Day 4 after immunization. Because the 1:10^{6} dilution is significantly more concentrated, this is not unexpected. More importantly, this capacitive immunosensor can detect target antibodies at extremely low concentrations as early as four days and through 21 days post-vaccination.

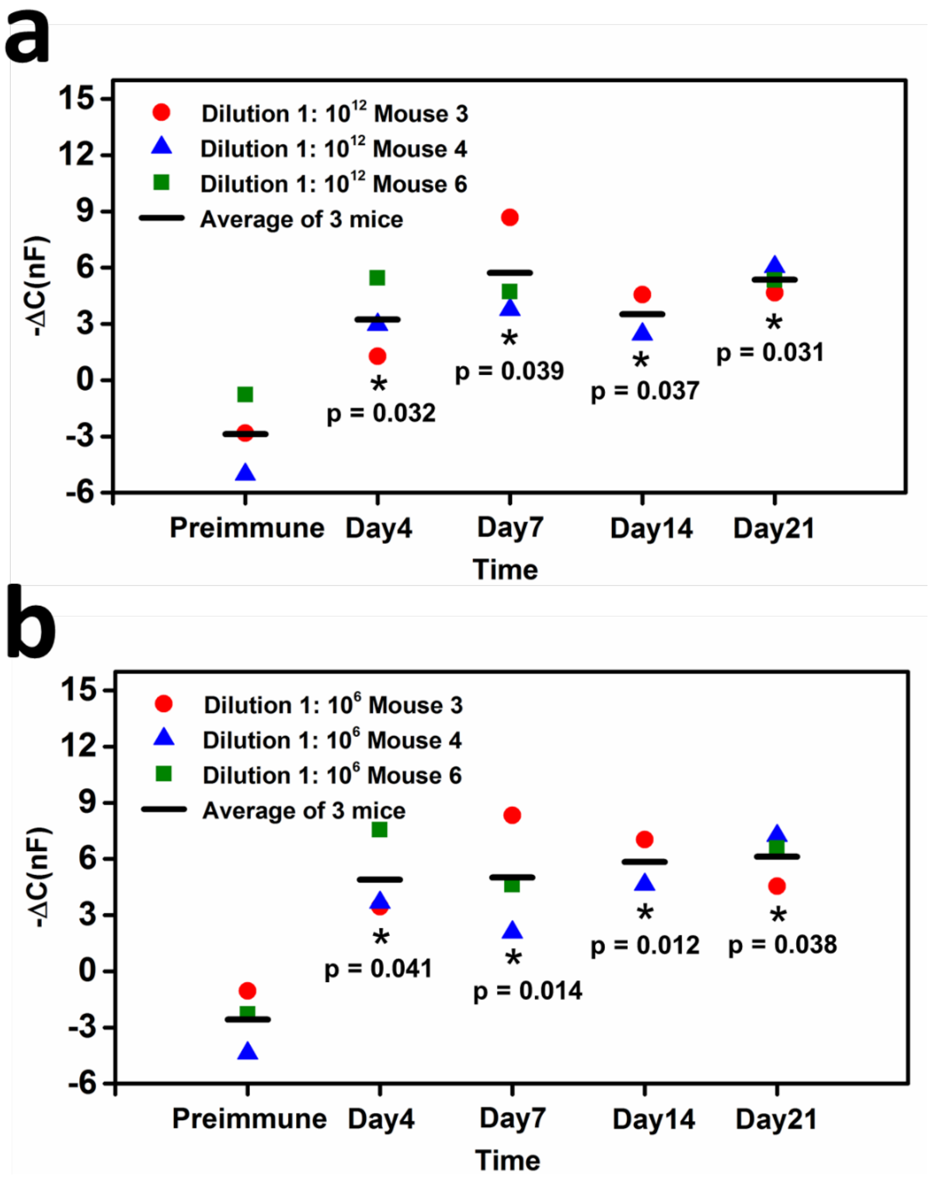

Figure 5.4 Immune response kinetics for mouse serum samples. Capacitive response to mouse serum at different time points pre- and-post vaccination with ZIKV. (**a**) The mouse serum was tested at a 1:10^{12} dilution in 1⨉ PBST buffer; (**b**) The mouse serum was tested at a 1:10^6 dilution in 1⨉ PBST buffer. Three biological samples (n = 3, mean ± STD) for each time point were tested except for Day 14 (n = 2, mean ± STD). Each biological sample shown is the average of three technique replicates. The paired t-test was carried out between pre- and post- vaccination with ZIKV samples. * paired *t*-test: $p < 0.05$.

Reliably detecting as few as ten molecules and accurately analyzing serum at dilutions of 1:10^{12}, these results suggest that our sensor has a sensitivity that is far superior to other platforms

[9,35]. This increased sensitivity enables us to detect an antibody response four days earlier compared to established serological methods [36]. Our sensor also requires less sample volume than comparable ELISAs (30 µL of $1:10^{12}$ vs 50-100 µL of 1:400 diluted sample [37]), which preserves precious serum sample and reduces reagent waste. Furthermore, whereas the CDC ZIKV MAC-ELISA needs 12+ hours to obtain results from sample application, our sensor can produce results in under ten minutes. This could result in faster diagnostics needed to determine a timely and effective therapeutic intervention.

5.3.5 Specificity tests with mouse sera

To further characterize the specificity of our sensors, we examined whether anti-ZIKV serum had any cross-reactivity with CHIKV sensors. CHIKV E antigen was conjugated to the microwire as a control probe to test two dilutions ($1:10^{12}$ and $1:10^{6}$) of the pre-immune and ZIKV-vaccinated Day 21 mouse serum. Figure 5.5 compares the $-\Delta C$ results obtained with specific ZIKV E probe and control CHIKV E probe. The *y*-axis marks the difference in $-\Delta C$ between Day 21 and pre-immune samples, and the *x*-axis denotes the two probes used. As shown in Figure 5.5a, the $-\Delta C$ between Day 21 and pre-immune mouse serum using ZIKV E probe is approximately 9 nF at the $1:10^{12}$ dilution, suggesting that ZIKV antibody concentrations increase significantly after 21 days post vaccination. In comparison, the CHIKV E sensor shows almost no change (~0 nF), 21 days post ZIKV vaccination, indicating that only specific binding occurred. A small increase in capacitance may be attributed to small amounts of nonspecific adsorption. There is a statistically significant difference between the ZIKV E and CHIKV E functionalized sensors. Similar results are observed for a $1:10^{6}$ dilution (Figure 5.5b.)

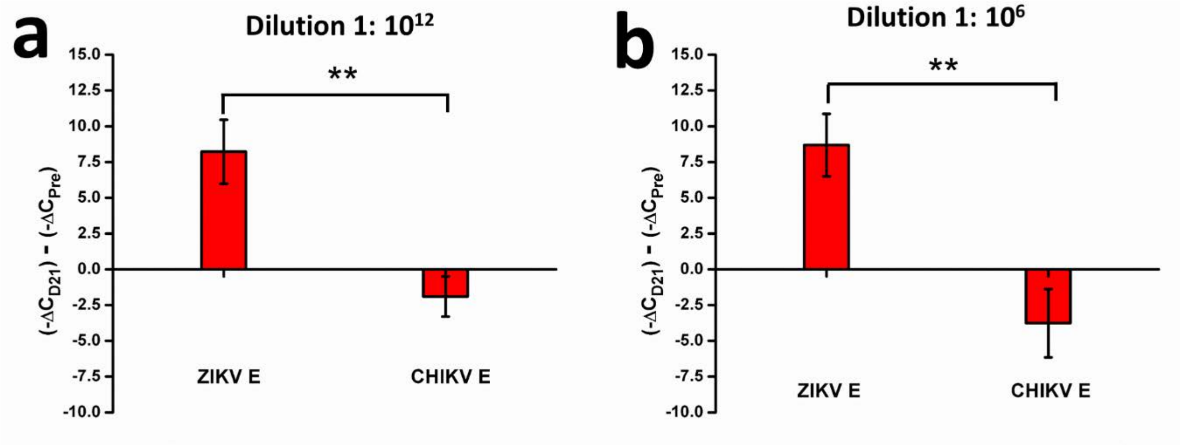

Figure 5.5 Specificity tests with mouse serum samples. (**a**) The difference between the negative capacitance change for Day 21 and pre-immune mouse serum samples at a $1:10^{12}$ dilution in 1× PBST buffer are compared for ZIKV E and CHIKV E recognition antigens ($n = 3$ at each concentration, mean ± STD). (**b**) The difference between the negative capacitance for Day 21 and pre-immune mouse serum samples at a $1:10^6$ dilution in 1× PBST buffer are compared for ZIKV E and CHIKV E recognition antigens ($n = 3$ at each concentration, mean ± STD). ** paired *t*-test: $p < 0.01$.

These results demonstrate satisfactory reproducibility and further validate the excellent specificity and sensitivity of this platform in a complex physiological matrix. Therefore, our sensor may be useful for direct detection of antigen-specific antibodies in serum and other potential types of biological sample.

5.3.6 Isotyping of antibodies in mouse serum samples

Isotyping is a diagnostic component required to separate acute from past infections. To characterize whether our wire sensor platform can be used to for isotype determination of a serum sample, wire sensors were functionalized with ZIKV E protein and saturated with antibody using a $1:10^6$ dilution of serum from Day 4 or Day 21. Anti-mouse IgM or IgG was applied to the sensor and the results are compared in Figure 6. As expected from published flavivirus antibody kinetics [38] and the corresponding ELISA data (Fig S5.3), Day 4 IgM levels were higher than IgG. It was somewhat surprising that the sensor detected constant levels of IgM between Day 4 and Day 21 given that the ELISA showed an increase from Day 4 to Day 21.

This may be explained by saturation of the sensor. A recent report, however, indicates that anti-ZIKV IgM levels drop off 8-16 days after symptom onset [36]. The discrepancy between our ELISA data and theirs may be due to our use of the immunodominant E protein instead of NS1 as antigen or it could be related to differences in host species. Antibody kinetics for dengue virus indicate that IgM can be detected for over 90 days [38], suggesting that a higher titer for Day 21 is reasonable. The sensor results also show an increase in IgG levels from Day 4 to Day 21, which agrees with the ELISA data. However, higher IgG than IgM levels do conflict somewhat with the ELISA results, which show slightly higher IgM for both days. Because the IgM is significantly larger than IgG, it is possible that steric hindrance causes the IgM sensor to saturate faster than the IgG sensor. As a smaller molecule, more IgG may be able to bind to the wire surface and produce a larger signal.

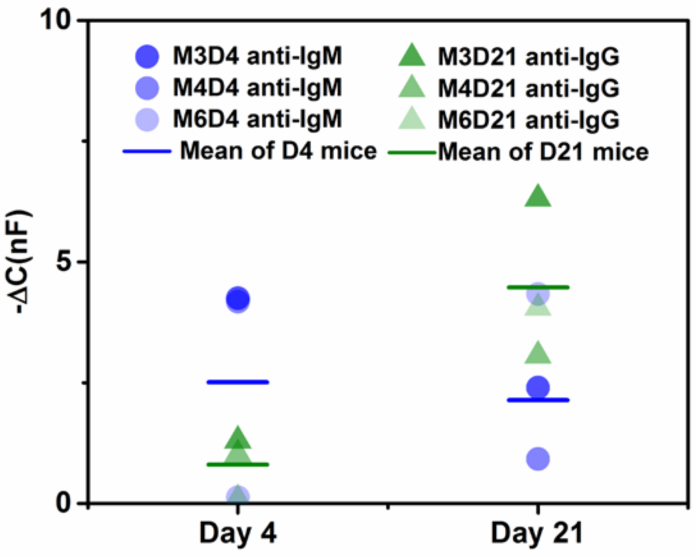

Figure 5.6 Isotyping of antibodies in mouse serum samples. Capacitive response of antibody isotypes in mouse serum at day 4 and 21 with ZIKV. The mouse serum was tested at a 1:10^6 dilution in 1× PBST buffer. Three biological samples (*n* = 3, mean ± STD) for each time point were tested. Each biological sample shown is the average of three technical replicates.

Cabral-Miranda *et al*. recently published an immunosensor for ZIKV antibody with isotyping capacity that was able to detect a 10^6 to 10^7 dilutions of serum [9]. However, the reported design incorporates a toxic redox couple that limits its point of care use in addition to decreased sensitivity compared to our system. Without using labels or redox couples, our sensor can distinguish antibody isotypes from a complex serum matrix containing a mixture of isotypes. These results enhance the applicability of the sensor for point of care diagnostic purposes and even for research purposes.

5.4 Conclusion

Although diagnosis of infectious diseases like ZIKV require laboratory confirmation, current methodologies are limited to use by specialized diagnostic laboratories. Recent outbreaks like that of Ebola virus and ZIKV indicate a growing need for simple, sensitive, and selective diagnostics amenable to a point of care setting. The ultra-sensitive capacitance sensor introduced in this study represents a simple and robust platform for pathogen-specific antibody detection in serum. Within minutes, it can detect as few as 10 antibody molecules in a 30 µL volume, as well as determine the antibody isotype. Without using labels or redox couples, our sensor can detect anti-ZIKV antibodies during an immunization time course and distinguish antibody isotypes from a complex serum matrix containing a mixture of isotypes. Furthermore, this sensor design can be easily integrated with microfluidics and handheld measuring devices to make it suitable for field work and point of care testing. Our research team is currently working to integrate this immunosensor platform into our previously developed paper-based analytical device [39]. Continued development of this novel platform technology can greatly increase the capacity of public health agencies worldwide to assess drug or vaccine efficacy and to monitor emerging infectious diseases of global importance in future.

REFERENCES

[1] P. D. Burbelo, K. H. Ching, E. R. Bush, B. L. Han, and M. J. Iadarola, “Antibody-profiling technologies for studying humoral responses to infectious agents.,” *Expert Rev. Vaccines*, vol. 9, no. 6, pp. 567–578, Jun. 2010.

[2] M. J. Parnham and F. P. Nijkamp, *Principles of Immnunopharmacology*. 2005.

[3] J. R. Crowther, *The ELISA Guidebook Series Editor*. 2008.

[4] L. Petersen, D. Jamieson, A. Powers, and M. Honein, “Zika Virus,” *N. Engl. J. Med.*, vol. 374, no. 16, pp. 1552–1563, 2016.

[5] I. B. Rabe, J. E. Staples, J. Villanueva, K. B. Hummel, J. A. Johnson, L. Rose, MTS, S. Hills, A. Wasley, M. Fischer, and A. M. Powers, “Interim Guidance for Interpretation of Zika Virus Antibody Test Results.,” *MMWR. Morb. Mortal. Wkly. Rep.*, vol. 65, no. 21, pp. 543–6, 2016.

[6] P. Yager, G. J. Domingo, and J. Gerdes, “Point-of-Care Diagnostics for Global Health,” *Annu. Rev. Biomed. Eng.*, vol. 10, no. 1, pp. 107–144, 2008.

[7] I. C. Prado, M. E. T. A. Chino, A. L. dos Santos, A. L. A. Souza, L. G. Pinho, E. R. S. Lemos, and S. G. De-Simone, “Development of an electrochemical immunosensor for the diagnostic testing of spotted fever using synthetic peptides,” *Biosens. Bioelectron.*, vol. 100, no. July 2017, pp. 115–121, 2018.

[8] G. Adornetto, L. Fabiani, G. Volpe, A. De Stefano, S. Martini, R. Nenna, F. Lucantoni, M. Bonamico, C. Tiberti, and D. Moscone, “An electrochemical immunoassay for the screening of celiac disease in saliva samples,” *Anal. Bioanal. Chem.*, vol. 407, no. 23, pp. 7189–7196, 2015.

[9] G. Cabral-Miranda, A. R. Cardoso, L. C. S. Ferreira, M. G. F. Sales, and M. F. Bachmann, “Biosensor-based selective detection of Zika virus specific antibodies in infected individuals.,” *Biosens. Bioelectron.*, vol. 113, no. April, pp. 101–107, Aug. 2018.

[10] C. Berggren, B. Bjarnason, and G. Johansson, “Capacitive biosensors,” *Electroanalysis*, vol. 13, no. 3, pp. 173–180, 2001.

[11] G. Ertürk and B. Mattiasson, “Capacitive biosensors and molecularly imprinted electrodes,” *Sensors (Switzerland)*, vol. 17, no. 2, pp. 1–21, 2017.

[12] L. Wang, M. Veselinovic, L. Yang, B. J. Geiss, D. S. Dandy, and T. Chen, “A sensitive DNA capacitive biosensor using interdigitated electrodes,” *Biosens. Bioelectron.*, vol. 87, pp. 646–653, 2017.

[13] K. Teeparuksapun, M. Hedstrom, E. Y. Wong, S. Tang, I. K. Hewlett, and B. Mattiasson,

“Ultrasensitive Detection of HIV-1 p24 Antigen Using Nanofunctionalized Surfaces in a Capacitive\rImmunosensor,” *Anal. Chem.*, vol. 82, no. 20, pp. 8406–8411, 2010.

[14] B. Mattiasson and M. Hedström, “Capacitive biosensors for ultra-sensitive assays,” *TrAC - Trends Anal. Chem.*, vol. 79, pp. 233–238, 2016.

[15] S. Loyprasert, M. Hedström, P. Thavarungkul, P. Kanatharana, and B. Mattiasson, “Sub-attomolar detection of cholera toxin using a label-free capacitive immunosensor,” *Biosens. Bioelectron.*, vol. 25, no. 8, pp. 1977–1983, 2010.

[16] C. N. Soares, P. Brasil, R. Medialdea, C. Msc, P. Sequeira, A. Bispo De Filippis, V. A. Borges, F. Theophilo, M. A. Ellul, M. Tom, and S. Frcp, “Fatal encephalitis associated with Zika Virus infection in an adult,” *J. Clin. Virol.*, vol. 83, no. January, pp. 63–65, 2016.

[17] S. Mécharles, C. Herrmann, P. Poullain, T. Tran, N. Deschamps, G. Mathon, A. Landais, and S. Breurec, “Case Report Acute myelitis due to Zika virus infection,” *Lancet*, vol. 8, no. 16, p. 6736, 2016.

[18] G. Carteaux, M. Maquart, A. Bedet, D. Contou, P. Brugières, S. Fourati, L. Cleret de Langavant, T. de Broucker, C. Brun-Buisson, I. Leparc-Goffart, and A. Mekontso Dessap, “Zika Virus Associated with Meningoencephalitis.,” *N. Engl. J. Med.*, pp. 1386–1388, Mar. 2016.

[19] E. Oehler, L. Watrin, P. Larre, I. Leparc-Goffart, S. Lastere, F. Valour, L. Baudouin, H. Mallet, D. Musso, and F. Ghawche, “Zika virus infection complicated by Guillain-Barre syndrome--case report, French Polynesia, December 2013.,” *Euro Surveill.*, vol. 19, no. 9, pp. 7–9, 2014.

[20] L. O. Ventura, C. V Ventura, L. Lawrence, V. van der Linden, A. van der Linden, A. L. Gois, M. M. Cavalcanti, E. A. Barros, N. C. Dias, A. M. Berrocal, and M. T. Miller, “Visual impairment in children with congenital Zika syndrome,” *J. Am. Assoc. Pediatr. Ophthalmol. Strabismus*, p. -, 2017.

[21] M. C. Leal, L. F. Muniz, T. S. A. Ferreira, C. M. Santos, L. C. Almeida, V. Van Der Linden, R. C. F. Ramos, L. C. Rodrigues, and S. S. Caldas Neto, “Hearing Loss in Infants with Microcephaly and Evidence of Congenital Zika Virus Infection — Brazil , November 2015 – May 2016,” *MMWR Morb Mortal Wkly Rep*, vol. 65, no. November 2015, pp. 2015–2017, 2016.

[22] A. A. van der Eijk, P. J. van Genderen, R. M. Verdijk, C. B. Reusken, R. Mögling, J. J. A. van Kampen, W. Widagdo, G. I. Aron, C. H. GeurtsvanKessel, S. D. Pas, V. S. Raj, B. L. Haagmans, and M. P. G. Koopmans, “Miscarriage Associated with Zika Virus Infection.,” *N. Engl. J. Med.*, pp. 1386–1388, Jul. 2016.

[23] J. Mlakar, M. Korva, N. Tul, M. Popović, M. Poljšak-Prijatelj, J. Mraz, M. Kolenc, K. Resman Rus, T. Vesnaver Vipotnik, V. Fabjan Vodušek, A. Vizjak, J. Pižem, M. Petrovec, and T. Avšič Županc, “Zika Virus Associated with Microcephaly,” *N. Engl. J.*

Med., p. 160210140106006, 2016.

[24] C. V Ventura, M. Maia, V. Bravo-Filho, A. L. Góis, and R. Belfort, “Zika virus in Brazil and macular atrophy in a child with microcephaly,” *Lancet*, vol. 387, no. 10015, p. 228, 2016.

[25] J. J. Miner, B. Cao, J. Govero, A. M. Smith, E. Fernandez, O. H. Cabrera, C. Garber, M. Noll, R. S. Klein, K. K. Noguchi, I. U. Mysorekar, and M. S. Diamond, “Zika Virus Infection during Pregnancy in Mice Causes Placental Damage and Fetal Demise,” *Cell*, vol. 165, no. 5, pp. 1081–1091, 2016.

[26] T. C. Pierson, M. D. Sánchez, B. A. Puffer, A. A. Ahmed, B. J. Geiss, L. E. Valentine, L. A. Altamura, M. S. Diamond, and R. W. Doms, “A rapid and quantitative assay for measuring antibody-mediated neutralization of West Nile virus infection,” *Virology*, vol. 346, no. 1, pp. 53–65, 2006.

[27] L. M. Fischer, M. Tenje, A. R. Heiskanen, N. Masuda, J. Castillo, A. Bentien, J. Émneus, M. H. Jakobsen, and A. Boisen, “Gold cleaning methods for electrochemical detection applications,” *Microelectron. Eng.*, vol. 86, no. 4–6, pp. 1282–1285, 2009.

[28] L. Wang, W. Liu, Y. Wang, J. Wang, Q. Tu, R. Liu, and J. Wang, “Construction of oxygen and chemical concentration gradients in a single microfluidic device for studying tumor cell-drug interactions in a dynamic hypoxia microenvironment.,” *Lab Chip*, vol. 13, no. 4, pp. 695–705, 2013.

[29] K. Aoki, “Theory of ultramicroelectrodes,” *Electroanalysis*, vol. 5, no. 8, pp. 627–639, 1993.

[30] P. Salaün and C. M. G. Van Den Berg, “Voltammetric detection of mercury and copper in seawater using a gold microwire electrode,” *Anal. Chem.*, vol. 78, no. 14, pp. 5052–5060, 2006.

[31] J. A. Adkins and C. S. Henry, “Electrochemical detection in paper-based analytical devices using microwire electrodes,” *Anal. Chim. Acta*, vol. 891, pp. 247–254, 2015.

[32] I. I. Suni, “Impedance methods for electrochemical sensors using nanomaterials,” *TrAC - Trends Anal. Chem.*, vol. 27, no. 7, pp. 604–611, 2008.

[33] A. M. Nicolini, K. E. McCracken, and J. Y. Yoon, “Future developments in biosensors for field-ready Zika virus diagnostics,” *J. Biol. Eng.*, vol. 11, no. 1, pp. 1–9, 2017.

[34] K. M. Bullard-Feibelman, J. Govero, Z. Zhu, V. Salazar, M. Veselinovic, M. S. Diamond, and B. J. Geiss, “The FDA-approved drug sofosbuvir inhibits Zika virus infection,” *Antiviral Res.*, vol. 137, pp. 134–140, 2017.

[35] J. Cecchetto, F. C. B. Fernandes, R. Lopes, and P. R. Bueno, “The capacitive sensing of NS1 Flavivirus biomarker,” *Biosens. Bioelectron.*, vol. 87, no. August 2016, pp. 949–956, 2017.

[36] Y. E. Jeong, G. W. Cha, J. E. Cho, E. J. Lee, Y. Jee, and W. J. Lee, “Viral and serological kinetics in Zika virus-infected patients in South Korea,” *Virol. J.*, vol. 14, no. 1, pp. 4–9, 2017.

[37] CDC, “Zika MAC-ELISA For Use Under an Emergency Use,” 2016.

[38] The Centers for Disease Control and Prevention, “Laboratory Guidance and Diagnostic Testing,” *Centers Dis. Control Prev.*, p. 1, 2016.

[39] R. B. Channon, Y. Yang, K. M. Feibelman, B. J. Geiss, D. S. Dandy, and C. S. Henry, “Development of an Electrochemical Paper-Based Analytical Device for Trace Detection of Virus Particles.,” *Anal. Chem.*, May 2018.

CHAPTER 6: CONCLUSION

Over the past several decades, different aspects of pathogen-detecting platforms have been extensively studied in a massive effort to achieve true point-of-care diagnostic capability. The World Health Organization established the ASSURED criteria for truly point-of-care platforms. This acronym stands for Affordable, Sensitive, Specific, User-friendly, Rapid and robust, Equipment-free and Delivered to these in need [1]. Despite recent technological advances, the development of such platforms meeting the ASSURED criteria remains elusive. In this dissertation, the platforms for microorganism detection, including whole microorganism separation, nucleic acid and antibody sensing, have been constructed, validated and applied to clinical related samples under the guidance of the ASSURED criteria.

6.1 Conclusions from Chapters 2 and 3

A passive approach for inertial focusing of micron and submicron-sized particles and bioparticles with high throughput has been systemically studied to sort microorganisms. Besides microorganism enrichment and separation, there are a broad set of potential applications for this platform, such as isolating subcellular organelles, monitoring heterogeneous responses of bacteria in drug susceptibility testing, and observing signals of bacteria and subcellular organelles in miniaturized cytometry and digital microfluidics.

In addition, efficient inertial focusing of nano-scale particles/bioparticle, e.g., virus and DNA, is still waiting for exploration and exploitation. However, reducing channel size, as what we did in chapters 2 &3, may not be enough to achieve this goal alone. Introductions of additional active manipulation techniques and viscoelastic forces into the current platform could be explored.

The current theory of inertial focusing is feasible to guide experimental explorations on the effects of altering channels dimensions and operation conditions for specific sizes or shapes of particles, but the lack of the ability to accurately predict the outcomes of a proposed experiment still eludes researchers. Therefore, the optimization of microchannels designs for broader biomedical applications using numerical simulations is one of the intriguing areas for future research. More efforts are still needed to uncover the detailed underlying mechanism of inertial focusing and provide explicit guidelines for point-of-use applications to the end users without backgrounds on inertial microfluidics.

The works presented in chapters 2&3 in this dissertation are fundamentally two dimensional (2D) focusing. Only two focal positions on a 2D plane were achieved, due to the limitations on channel geometries imposed by the fabrication technique used. Three-dimensional (3D) printing technology has demonstrated capacities toward design and fabrication 3D structure in an inexpensive and rapid manner. Integration of 3D printing technique with inertial microfluidics could be promising for rapid production of three dimensional microchannel, for example, vertical tightly curving loops and the alternation of horizontal and vertical straight sections [2]. Such structures are able to provide an additional focusing dimension to realize 3D particle inertial focusing.

In conclusion, significant progress has been made for inertial microfluidics in the past decade towards high-throughput, low-cost, and wide applications, but a wide range of raw territories are still waiting to be explored to further uncover mechanisms and expand applications.

6.2 Conclusions from Chapters 4 and 5

To directly test nucleic acid and anti-pathogen antibody in an ultra-sensitive way, capacitive based affinity sensors have been built and tested with clinically relevant samples. Both the DNA sensor and immunosensor designs can be easily integrated with microfluidics and handheld measurement devices to make them suitable for field work and point of care testing. Furthermore, the widely-used smartphones are presenting unprecedent opportunities toward point of care detection of pathogen in a low-resource setting. Adaptable connectors for smartphone are therefore worthwhile to be further explored for the DNA and antibody detection platforms developed in chapters 4&5.

The ability to perform multiplexed tests can be explored through integrating parallel testing units, which is especially important for the detection of pathogens that have similar infection symptoms. Parallel multiplexing is also able to reduce detection costs by providing multiple information from a single-shot analysis.

Furthermore, these sensors can be constructed as paper-based analytical devices, which would further cut the cost of detection largely but still retain good sensitivity and specificity. Further studies should also explore the stability of the devices under a wide range of conditions, such as storage, transport, and clinical administration.

In order to bring microsystems developed in laboratory conditions to commercial market, strong collaborations between academia and industry are needed to address the key issues, such as the reproducibility. As reported, it is common to have the device-to-device variabilities due to the techniques of fabrication and electrode modification used in the laboratory [3]. The commercialized screen printing of electrodes can provide improved biosensor reproducibility in large scale productions. Companies producing commercially available screen-printed electrodes, including Metrohm USA Inc., DropSens S.L., and Bio-Logic SAS [4], are able to bridge this gap.

Possible future applications of the developed DNA and antibody detection platforms include, but are not limited to, pathogen detections. For instance, these devices could be expanded to non-invasive diagnostics of Down syndrome and other aneuploidies through the blood sample of pregnant women containing DNA from their fetus; it is also promising to adapt the developed antibody sensor to monitor the status of the immune system by sensing the repertoire of expressed antibodies, which could provide a detailed picture of the various processes of immune defense.

Continued developments of these novel platforms can greatly increase the capacity of public health agencies worldwide to assess drug or vaccine efficacy and to monitor emerging infectious diseases and personal health condition in the future.

REFERENCES

[1] M. Urdea, L. a Penny, S.S. Olmsted, M.Y. Giovanni, P. Kaspar, A. Shepherd, P. Wilson, C. a Dahl, S. Buchsbaum, G. Moeller, D.C. Hay Burgess, Requirements for high impact diagnostics in the developing world., Nature. 444 Suppl (2006) 73–79. doi:10.1038/nature05448.

[2] P. Paiè, F. Bragheri, D. Di Carlo, R. Osellame, Particle focusing by 3D inertial microfluidics, Microsystems Nanoeng. 3 (2017) 17027. doi:10.1038/micronano.2017.27.

[3] R.B. Channon, Y. Yang, K.M. Feibelman, B.J. Geiss, D.S. Dandy, C.S. Henry, Development of an Electrochemical Paper-Based Analytical Device for Trace Detection of Virus Particles., Anal. Chem. (2018). doi:10.1021/acs.analchem.8b02042.

[4] A. Ahmed, J. V. Rushworth, N.A. Hirst, P.A. Millner, Biosensors for whole-cell bacterial detection, Clin. Microbiol. Rev. 27 (2014) 631–646. doi:10.1128/CMR.00120-13.

APPENDIX I: SUPPLEMENTARY INFORMATION FOR CHAPTER 5

7.1 Preparation of plasmids for Zika DNA immunization.

Genes for the Zika virus PRVABC59 strain (NCBI Accession: KX087101) capsid and prM-Env proteins were codon-optimized for mammalian expression and synthesized by Genescript Inc. The V5 epitope tagged capsid gene was cloned into the EcoRV site of pcDNA3.1 (plasmid pBG610), and a Japanese encephalitis virus prM signal sequence was added to the prM-Env gene and the construct was cloned into the EcoRV site of pcDNA3.1 (pBG611) as previous described [1]. Plasmid sequences will be provided upon request. Expression of capsid and prME proteins after transfection into Vero cells was verified by Western blot analysis using anti-V5 (Life Tech) and anti-Envelope (4G2 [2](ATCC HB-112 (D1-4G2-4-15))) antibodies, respectively (data not shown).

DNA was prepared for immunization using the TempliPhi Rolling Circle Amplification Kit (GE HealthCare) according to the manufacturer's instructions. DNA was purified by phenol:chloroform extraction and ethanol precipitation, quantified by UV spectrometry, and stored at -20^{o}C until DNA immunization. Equal molar amounts of each amplified DNA were prepared in saline at 2μg total DNA/50μl or 10μg total /50μl prior to immunization.

7.2 Ethics Statement.

This study was carried out in strict accordance with the recommendations in the Guide for Care and Use of Laboratory Animals of the National Institutes of Health. The protocols were approved by the Institutional Animal Care and Use Committee at the Colorado State University (Assurance Number: D16-00345) under IACUC protocol number 16-6565A. Every effort was taken to minimize pain and suffering in the animals.

7.3 DNA Immunization.

Ten 6-week old female CD1 outbred mice were purchased from Jackson Laboratories for use in DNA vaccination studies. Pre-immune sera were collected from each mouse via submandibular vein punctures, and five mice (Mice 1-5) were immunized intramuscularly with 4µg total DNA (50 µl of 2µg/50µl in each flank (Mice 1-3)) or 20 µg total DNA (50µl of 10µg/50µl in each flank (Mice 6-10)). 100 µl of whole blood was collected via retro-orbital bleed at Days 4, 7, 14, and 21 post-immunization. At Day 28 post-immunization, mice were anesthetized with isoflurane and terminal bleeds were collected via cardiac puncture. Sera was separated from whole blood via centrifugation at 13K RPM, and clarified sera were stored at -20^{o}C in single-use aliquots until use.

7.4 Initial Assessment of IgG Antibody in Immunized Sera via Western Blot and ELISA.

Aliquots of Day 21 sera from Mice 1-10 were used as the source of primary antibodies in strip Westerns. Vero cells infected with the PRVABC59 strain of Zika virus [3] were lysed in Laemelli buffer and resolved on 12% PAGE gels. Proteins were transferred to nitrocellulose membranes that were subsequently cut into strips. Strips were blocked in phosphate-buffered saline 0.05% Tween + 2% non-fat dried milk (PBST-NFDM), then incubated in PBST-NFDM with each sera (1:100 dilution) overnight. 10 µg/mL of 4G2 antibody was used as a control. Strips were washed with PBST, incubated with anti-mouse IgG HRP (abcam# ab6728) in PBST-NFDM for 1 hr, washed with PBST, and developed with Pierce 1-step Ultra TMB-blotting solution. Results of the Western blots are shown in Supplementary Figure 5.1.

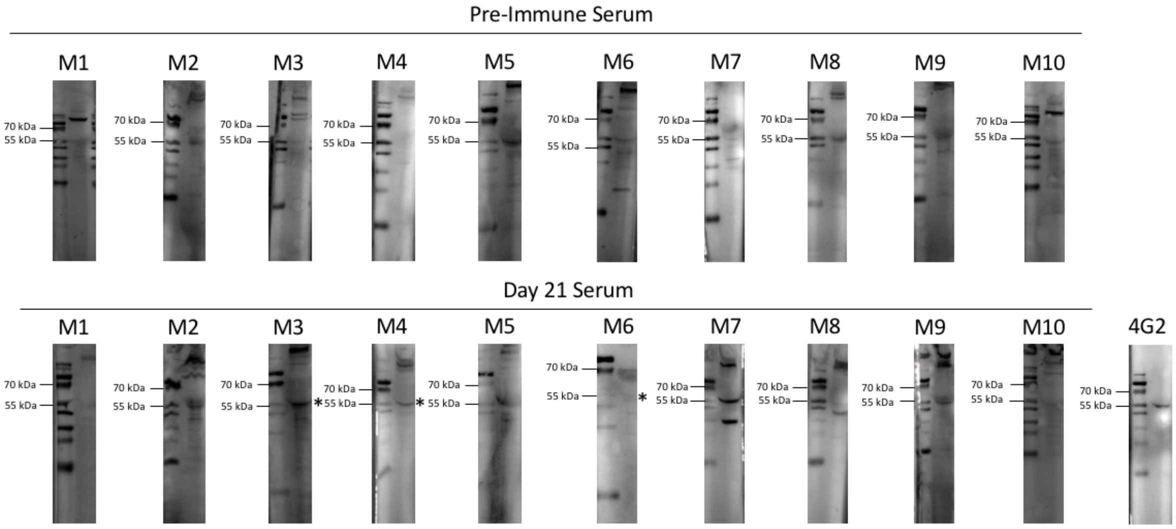

Fig. S5.1. Western blot analysis of IgG antibody responses in mice immunized with Zika DNA vaccine. * denotes the presence of anti-Zika envelope reactivity in Day 21 samples.

An ELISA assay was used to determine the relative amounts of IgM and IgG in the Mouse 3, 4, and 6 Day 4 and Day 21 serum samples. Briefly, 100 µL of 10 µg/mL ZIKV E protein (My Biosource Cat# MBS319787) diluted in PBS (pH 7.4) was added to each well of a Nunc Maxisorp 96 well plate (Cat# 44-2404-21) and incubated at 4˚C overnight. Excess antigen was discarded and the wells were washed three times with 0.05% PBST (pH 7.4). 300µL of fresh blocking buffer (4% milk powder in PBS) was then incubated in each well for 1 hour at room temperature. Afterwards, the wells were washed six times with 0.05% PBST. 100 µL of mouse serum was then incubated for 1 hour at room temperature at dilutions of 1:100, 1:500, and 1:2500. 10 µg/mL of 4G2 antibody was used as a positive control. The wells were washed again six times with 300µL of 0.05% PBST and 100 µL of 1:3000 HRP-conjugated anti-mouse IgG (AbCam ab97023) or IgM (AbCam ab97230) was incubated for 1 hour at room temperature. The plate was washed six times with 300 µL 0.05% PBST then again twice with 300 µL of PBS to eliminate residual detergent. 100 µL of TMB-ELISA substrate (ThermoScientific) was incubated for 30 minutes at room temperature and quenched with 100 µL of H_2SO_4. Absorbance was measured at 450 nm. Results of the ELISA assay are shown in Supplementary Figure 5.3.

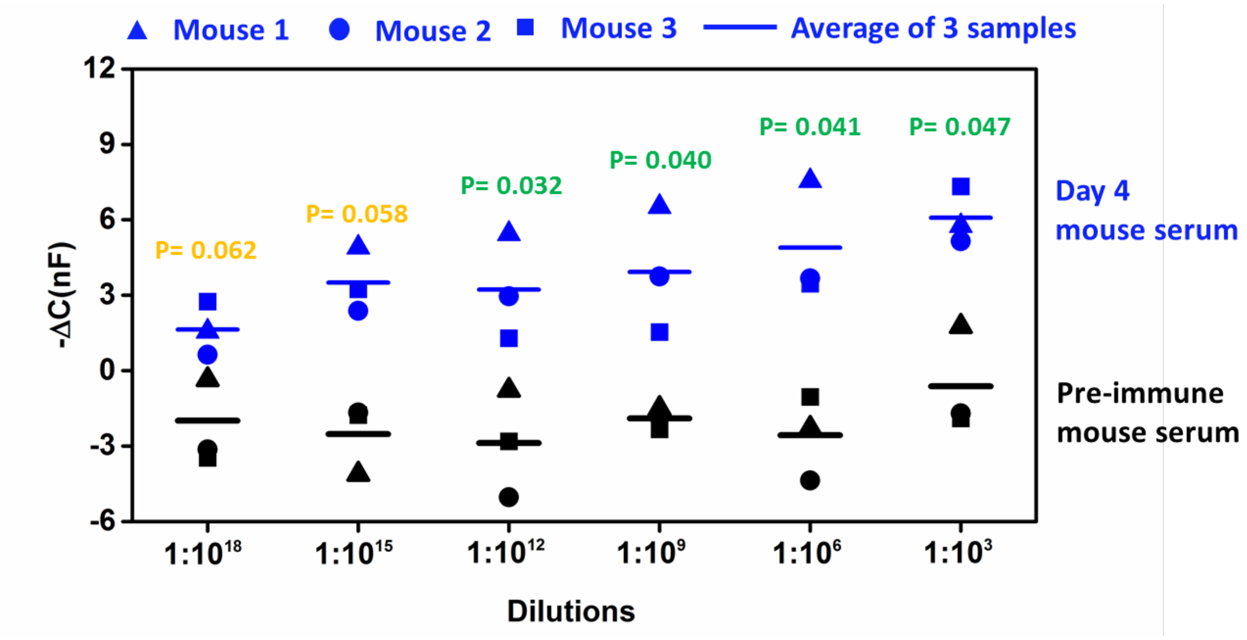

Fig. S5.2. Capacitive responses of pre-immune and Day 4 after ZIKV infected mouse serums at a wide range of dilutions from 1:10^{18} to 1:10^{3} dilutions in 1x PBST buffer (*n* = 3 at each dilution).

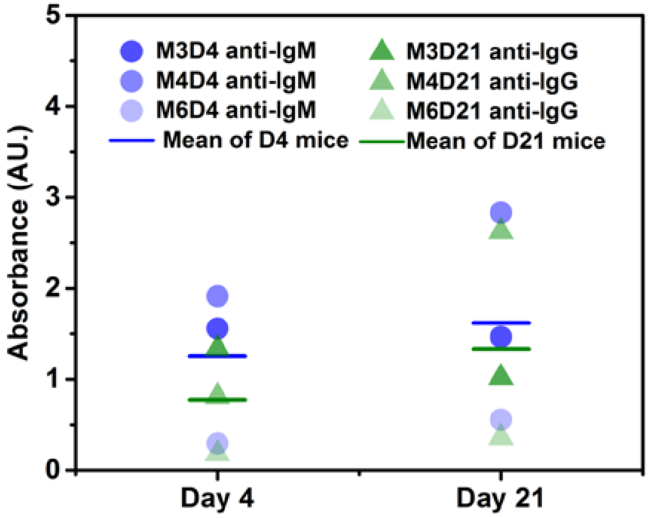

Fig. S5.3. ELISA analysis of anti-Zika IgM and IgG levels in Mice 3, 4, and 6.

REFERENCES

[1] T.C. Pierson, M.D. Sánchez, B.A. Puffer, A.A. Ahmed, B.J. Geiss, L.E. Valentine, L.A. Altamura, M.S. Diamond, R.W. Doms, A rapid and quantitative assay for measuring antibody-mediated neutralization of West Nile virus infection, Virology. 346 (2006) 53–65. doi:10.1016/j.virol.2005.10.030.

[2] E.A. Henchal, M.K. Gentry, J.M. McCown, W.E. Brandt, Dengue virus-specific and flavivirus group determinants identified with monoclonal antibodies by indirect immunofluorescence, Am. J. Trop. Med. Hyg. 31 (1982) 830–836. doi:10.4269/ajtmh.1982.31.830.

[3] J. Weger-Lucarelli, N.K. Duggal, K. Bullard-Feibelman, M. Veselinovic, H. Romo, C. Nguyen, C. Rückert, A.C. Brault, R.A. Bowen, M. Stenglein, B.J. Geiss, G.D. Ebel, Development and Characterization of Recombinant Virus Generated from a New World Zika Virus Infectious Clone, J. Virol. 91 (2017) e01765–16. doi:10.1128/JVI.01765-16.